國立台灣大學 電信工程學研究所

博士論文

指導教授：李學智、李百祺 教授

運用 *K*-space 方法於超音波掃掠式系統之流速向量估測

Ultrasonic Vector Velocity Estimation in Swept-scan Using a *K*-space Approach

研究生：鄭耿璽　撰

中華民國九十四年七月

中文摘要

頻率大於 20MHz 的高頻超音波影像系統能夠觀察細微的組織以及量測微弱血流速度，然而由於高頻陣列探頭製作技術的困難，目前高頻系統大都採用單一探頭、機械掃瞄的方式來取得影像資訊，掃瞄的方法主要採用離散步進的方式(step scan)，這種方法相當耗時，無法提供即時的血流資訊。另一種稱作掃掠式掃瞄的技術(swept scan)則是讓探頭連續不間斷地移動，因此能大幅縮短成像的時間。雖然掃掠式掃瞄已應用於目前的高頻系統，然而探頭的連續移動對於流速的估計有著不可忽略的影響。為此，本論文主要目的則是從理論面以及實驗探討掃掠式掃瞄對於流速估計的效應，並針對掃掠式高頻系統提出一個新的定量流速估計方法。

本文首先利用二維空間頻譜的概念(稱為 *k*-space)來量化掃掠式掃瞄對於二維流速估測的影響。我們證明移動物體的空間頻譜等效於其時間頻譜 (亦即，由都卜勒頻率以及 RF 頻率所構成的二維頻譜)。另外，相較於離散式掃瞄，掃掠式掃瞄造成都卜勒頻寬的變動，此頻寬變動導致流速估計的偏差及變異。為了校正此一速度偏差並提高估計的精確度，我們提出一個基於 *k*-space 的流速向量估計方法。我們利用模擬以及體外流體實驗來驗證所提出的新方法，此外，我們亦利用 45MHz 的高頻系統來測量老鼠尾巴內的靜脈流速，實驗結果顯示所提出的流速向量估計方法適用於掃掠式高頻系統，並能有效地降低流速以及血管角度估計的誤差。

本研究之主要貢獻，在於以 *k*-space 之方式建構超音波血流分析之理論架構，並完整分析掃掠式掃描對於流速計算之影響，提升超音波小動物影像中定量血流分析之能力。

Abstract

The rapid developments in high-frequency ultrasound systems (operating at higher than 20 MHz) have allowed visualization of fine tissue structures and assessment of small vessels with slow flows. Due to the lack of high-frequency arrays, however, most current high-frequency systems use mechanically scanned, single-element transducers that are moved through a series of discrete positions. This scan technique, called the step scan, is relatively time consuming and cannot provide flow information in real-time. An alternative technique, called the swept scan, involves continuous scanning a transducer and is capable of improving the data acquisition time. Although the swept-scan technique is currently employed in high-frequency ultrasound systems, the continuous transducer movement may have non-negligible effects on accuracy of velocity estimation. It is therefore the purpose of this thesis to thoroughly investigate such effects, and to further develop a new quantitative flow estimation method.

In this thesis, a spatial frequency domain (i.e., *k*-space) approach is employed to quantify the effects of swept scanning on the spectral-broadening-based vector velocity estimation method. It is shown that the *k*-space representation of a 2-D moving object is equivalent to a Doppler-RF frequency domain representation, and that transducer movement in the swept-scan technique results in a change in Doppler bandwidth. The spectral broadening caused by swept scanning introduces velocity estimation bias and variance that are not present in the step-scan technique. In order to correct such effects and improve velocity estimation accuracy, a robust vector velocity estimation method is developed based on the proposed *k*-space approach. Both simulations and *in vitro* experiments were performed to evaluate performance of the proposed vector velocity estimator. Furthermore, *in vivo* measurements of mouse tail vessels were also conducted using a 45-MHz transducer. The results demonstrate that the proposed vector velocity estimator is feasible in a swept scan and can effectively reduce the velocity and angle estimation errors.

The main contributions of the thesis include development of a theoretical framework for ultrasonic flow analysis using a *k*-space approach. Based on this framework, effects of the swept scan on flow estimation were thoroughly investigated, thus making quantitative flow analysis in ultrasonic small animal imaging more feasible.

List of Symbols

$A_{\mathrm{R}}(x)$	receive aperture function
$A_{\mathrm{T}}(x)$	transmit aperture function
a	transducer aperture size
$B_{\mathrm{PE}}(f_t)$	pulse-echo temporal frequency response
bw_D	Doppler spectral bandwidth
bw_k	lateral spatial spectral bandwidth
d	transducer displacement during the pulse-echo round trip time
$\overline{f}$	mean Doppler frequency at f_c
$\overline{f_x}$	mean frequency of the lateral spatial spectrum
f_c	center frequency of the excitation
f_D	Doppler frequency
f_d	Doppler shift frequency
f_{num}	f-number
f_t	RF (temporal) frequency
f_x	lateral spatial frequency
f_z	axial spatial frequency
G	scaling factor in the *k*-space representation
M	number of axial spatial frequencies used for averaging
m	$f_z/2f_{\mathrm{num}}$
N_{A}	number of axial sampling points in the kernel
N_{L}	number of scan lines in the kernel
N_{R}	number of firings in a step scan
n	$f_z/2z_{\mathrm{f}}$
PRI	pulse repetition interval
$P_{\mathrm{ST}}(f_x, f_z)$	*k*-space representation of a stationary object in a step scan
$P_{\mathrm{SW}}(f_x, f_z)$	*k*-space representation of a stationary object in a swept scan
$P_{\mathrm{SW}}(f_D, f_t)$	temporal frequency representation of a stationary object in a swept scan
$P_{\mathrm{SW\_motion}}(f_x, f_z)$	*k*-space representation of a 2-D moving object in a swept scan
$P_{\mathrm{SW\_motion}}(f_D, f_t)$	temporal frequency representation of a 2-D moving object in a swept scan
$p_{\mathrm{SW}}(x, z)$	PSF of a stationary object in a swept scan
$p_{\mathrm{SW\_motion}}(x, z)$	PSF of a 2-D moving object in a swept scan
R	vessel radius
$R(\tau)$	autocorrelation function of flow samples in the slow-time axis
r	radial distance relative to the vessel center
t	time of flight (fast time)

$u(r)$	parabolic profile in a laminar flow
$u_{\max}$	maximum flow velocity
u_{obj}	object velocity vector
$u_{\text{obj(axial)\_max}}$	maximum detectable axial velocity in a step scan
$u_{\text{obj(max)}}$	maximum detectable velocity vector in a swept scan
u_{rel}	relative lateral velocity between the transducer and moving object
u_{scan}	scan speed
W_x	lateral kernel width
w_{eff}	–6-dB effective beamwidth
x	lateral direction
z	axial direction
z_{f}	focal depth
α	$\sin\alpha \cong d/z_{\text{f}}$
γ	scaling factor in determining bw_k
γ'	scaling factor in determining bw_D
Δs	scan line interval in a step scan
$\Delta u_{\text{obj(axial)}}$	axial velocity resolution in a swept scan
$\Delta u_{\text{obj(lat)}}$	lateral velocity resolution in a swept scan
Δx	scan line interval in a swept scan
Δz	axially sampling interval
θ	Doppler angle
$\hat{\theta}$	estimate of Doppler angle
θ_{cr}	Doppler critical angle
λ	wavelength
v	ratio of u_{obj} to u_{scan}
τ	slow time
ϕ	upper bound of the Doppler critical angle
ψ	tilt angle of the transducer
$\varphi(\tau)$	phase of $R(\tau)$
$\Pi(\bullet)$	rectangular function

Table of Contents

List of Figures

List of Tables

Chapter 1 Introduction

1.1 Doppler Ultrasound

Medical ultrasound systems have been well developed in assessing blood flow velocities. They can provide non-invasive detection of blood flow and display the velocity information in real-time. Typically, velocity estimation using ultrasound is mainly based on the Doppler principle, i.e., the received frequency from moving objects is shifted with respect to the transmitted frequency. The transducer generates an ultrasound beam that interacts with the moving objects (mainly red blood cells) in a vessel, and the backscattered echoes experience a frequency shift that can be used to detect the flow velocity. Generally, flow velocities in the human body are typically below 10 m/s and much less than the sound velocity (~1500 m/s) [1]. In this case, the frequency shift f_d of the received signals relative to the center frequency f_c of the excitation is approximately (see Fig. 1.1) [1]

$$f_d = f_c \frac{2u_{\text{obj}} \cos\theta}{c}, \tag{1.1}$$

where u_{obj} denotes the object velocity, c is the sound velocity, and θ is the angle between the beam and the flow direction (known as the Doppler angle). By transmitting a continuous wave (called CW Doppler), flow velocities parallel to the beam direction can be obtained by estimating the frequency shift of the received signals indicated in (1.1).

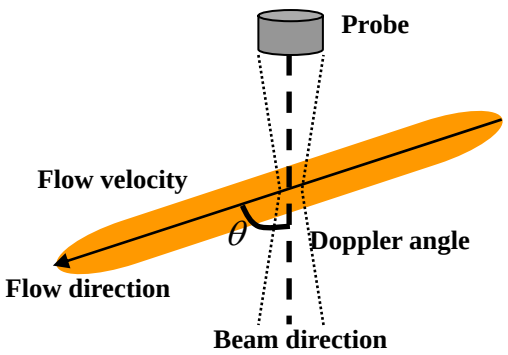

Fig. 1.1. Representation of a vessel intersected with the transmit beam.

The main limitation of CW Doppler is that it provides no range information. Alternatively, PW (pulsed wave) Doppler with which a group of short sinusoidal bursts is transmitted along a specific scan direction allows velocity estimation at a specific sample volume. Fig. 1.2 illustrates flow estimation in the PW Doppler mode. The received signals can be represented as a 2-D data set, with one axis representing the pulse firing index (called the slow-time axis) and the other axis being the time of flight (called the fast-time axis). The sampling interval in the slow-time axis is determined by the pulse repetition interval (PRI). The received data within a particular range gate are extracted and analyzed to measure the velocity parameters. Instead of estimating the frequency shift along the fast-time axis, the time difference due to the target motion between two consecutive received signals, given by $2u_{\text{obj}}\text{PRI}\cos\theta/c$ [2], is detected. Such a time difference leads to a frequency shift equal to (1.1) in the corresponding frequency domain of the slow-time axis (i.e., the Doppler frequency domain). The resulting spectrum (referred to as the Doppler spectrum) at a specific range gate can be estimated by using the Fourier transform and then displayed as a function of time (called Spectral Doppler). To provide real-time visualization of velocity information on the image plane, the related velocity parameters, such as the mean Doppler frequency and Doppler spectral energy, are spatially encoded in colors and superimposed on the B-mode imaging (called Color and Power Doppler, respectively). Fig. 1.2(b) provides the typical signal processing required for flow velocity estimation in PW Doppler, where the wall filter is operated in the slow-time axis and used to remove the signals from stationary tissues or slowly moving vessel walls.

In order to allow real-time display, the flow velocity in Color Doppler is typically estimated using 4–16 firings, which is much less than 64–128 pulses used in Spectral Doppler [2]. In this case, alternative efficient techniques rather than Fourier-transform-based methods are often adopted to provide reliable mean velocity estimation with a limited number of firings [3]–[6]. Note that these techniques mainly measure the axial velocity component (i.e., parallel to the beam direction). They can basically be classified as the phase- and time-shift estimation methods, and are described as follows.

1.1.1 Phase-shift Estimation Techniques

The phase shift caused by the target motion between two received signals can be detected by performing the autocorrelation between the flow samples along the slow-time axis [3]. Mathematically, the mean Doppler frequency (and thus the mean

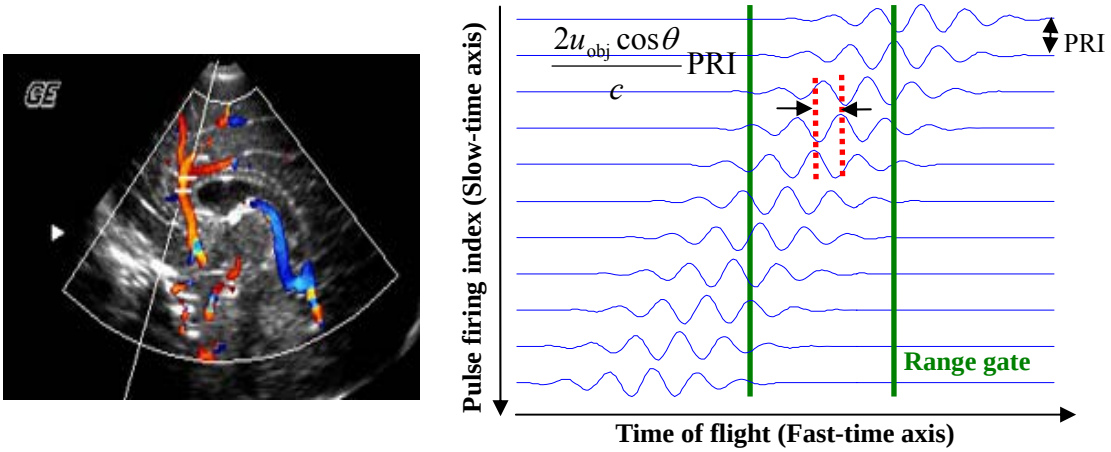

(a)

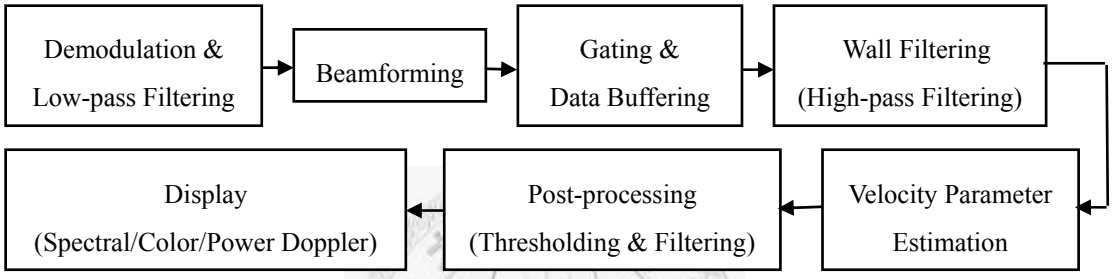

(b)

Fig. 1.2. Description of velocity estimation in the pulsed-wave Doppler mode. (a) The received echoes from repeated firings are represented as a 2-D data set. The time or phase shift between consecutive waveforms due to the flow motion is detected to obtain the flow velocity. (b) Block diagram for the primary signal processing at the receiver. (The image is from the website: http://www.gehealthcare.com/usen/ultrasound/).

axial velocity) is related to the autocorrelation function $R(\tau)$ of the flow signals by

$$\overline{f} = -\frac{j}{2\pi}\frac{\dot{R}(0)}{R(0)} = \frac{\dot{\varphi}(0)}{2\pi} \approx \frac{\varphi(\mathrm{PRI})}{2\pi\mathrm{PRI}}, \tag{1.2}$$

where $\varphi(\tau)$ is the phase of $R(\tau)$ and ‘ ˙ ’ represents the first-order temporal derivative [3]. The above equation indicates the mean Doppler frequency can be estimated directly by evaluating the phase of $R(\tau)$ at the first lag. The autocorrelation technique indicated in (1.2) is known as the 1-D autocorrelator because the received signals within the range gate along the fast-time axis are summed and reduced to one sample per firing. A 2-D autocorrelation technique

proposed by Loupas *et al.* [4], on the other hand, performs the two-dimensional autocorrelation on the slow- and fast-time plane. The primary difference between them is in the estimation of the RF frequency (i.e., the corresponding frequency domain of the fast-time). Different from the 1-D autocorrelator that is evaluated at the center RF frequency, the 2-D autocorrelator estimates the mean RF frequency. Compared to the 1-D autocorrelator, the 2-D autocorrelator is capable of accounting for the spectral variation resulting from attenuation or multiple scattering [4].

The common problem for the phase-shift techniques is that the spectral aliasing limits the maximum detectable axial velocity. The maximum detectable axial velocity is given by [1]

$$u_{\text{obj(axial)\_max}} = \frac{\lambda}{4PRI}, \tag{1.3}$$

which can be increased by decreasing the PRI, where λ is the wavelength. On the other hand, a decrease in the PRI degrades the velocity resolution and limits the maximum penetration depth. Despite such limitations, phase-shift estimation techniques are computationally efficient and commonly employed in current commercial ultrasound systems.

1.1.2 Time-shift Estimation Techniques

Time-shift techniques directly measure the time difference between successive received signals at a range gate. This can be accomplished by employing cross-correlation methods [1], the matched filter method (known as the wideband maximum likelihood estimation) [5], or the efficient trajectory search techniques across the whole received data set (known as the butterfly search) [6]. The main benefit of time-shift techniques is aliasing immunity. In addition, these techniques, as well as the 2-D autocorrelator, can be regarded as a wideband approach compared to the 1-D autocorrelator in which the phase shift is estimated with respect to the center frequency. The bandwidth of the transmit pulse is therefore allowed to be as wide as that used in the B-mode imaging.

1.2 High-frequency Flow Estimation

Current commercial ultrasound systems mainly operate at a frequency ranging from 2 to 10 MHz. The corresponding spatial resolution is about 0.3–1.5 mm and the

detectable velocity is on the order of cm/s. At such frequencies, quantitative velocity estimation is only achievable for large arteries and veins in the human body. For small vessels (< 0.1 mm in diameter) with slow flows (< 10 mm/s) or closely spaced vessels, the performance of velocity estimation is limited. In this case, only qualitative visualization of flow patterns can be provided by using Power Doppler.

Increasing the operating frequency to above 20 MHz (referred to as high-frequency ultrasound) provides an opportunity to quantitatively evaluate slow flows within a small vessel [7]–[22]. This is because both spatial and velocity resolutions can be simultaneously improved at higher frequencies [1]. Furthermore, another advantage of high-frequency ultrasound is that, as the frequency increases, the intensity of backscattered signals from red blood cells increases more than that from tissues [7], which leads to an improvement in the signal-to-clutter ratio. With these properties, high-frequency ultrasound allows flow measurements at the arteriolar and capillary level [12]–[16], and enables the study of vascular hemodynamics and morphology in the microcirculation [7].

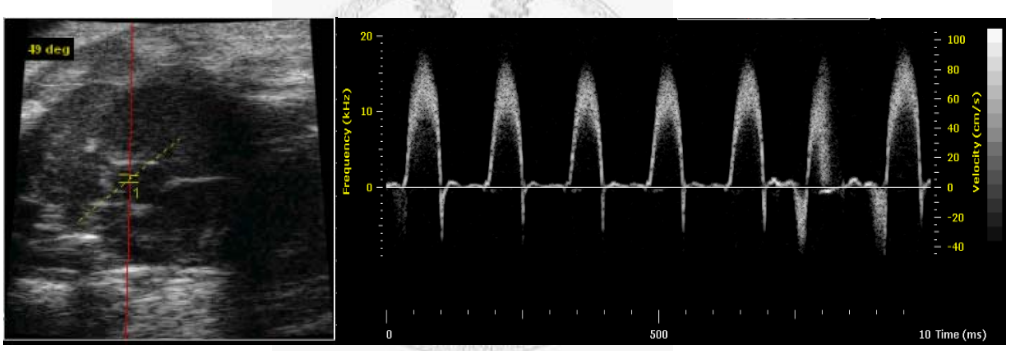

(a)

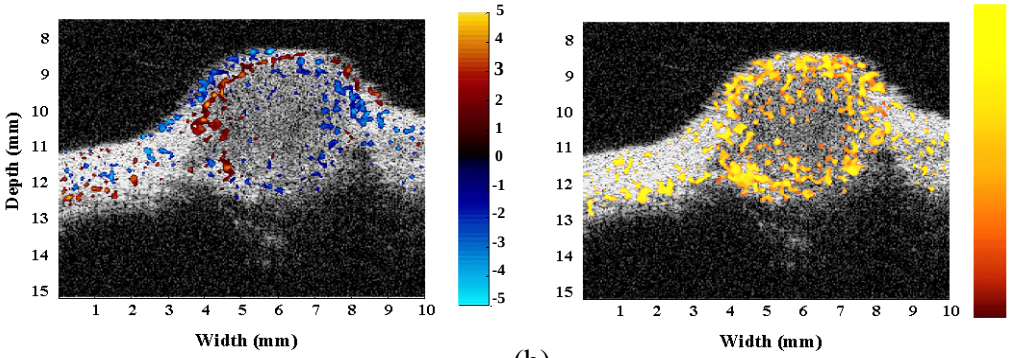

(b)

Fig. 1.3. High-frequency ultrasonic mouse imaging. (a) Spectral Doppler of aorta in an adult mouse (From the website: http://www.visualsonics.com/). (b) 40-MHz color Doppler (left) and power Doppler (right) images of a mouse tumor (From Li. *et al.* [20]).

Clinical applications of high-frequency ultrasound include imaging and flow assessment of the eye [10]–[14] and skin [7]. *In vivo* measurements of the ciliary body circulation in the human iris has been demonstrated using 40-MHz CW Doppler [12]. The vasculature of the rabbit eye using Color Doppler was also investigated by Kruse *et al.* [14]. The ability of measuring small vessels allows the evaluation of eye diseases such as glaucoma and anterior segment tumors, and skin cancers such as malignant melanoma [7]. High-frequency ultrasound is potentially capable of investigating tumor angiogenesis [7], quantifying blood flow over tumor areas [15]–[20], and producing 3-D microcirculation flow maps [16].

In addition, high-frequency ultrasound is well suited for small animal imaging [19]–[22]. Small animals, such as mice, have similar physiological structures and gene composition to humans, and hence have been used to develop various disease models [20][21][23]. High-frequency ultrasonic mouse imaging systems have recently become commercially available (VisualSonics^{TM} Vevo Series, Toronto, Ontario, Canada). High-frequency ultrasound has shown its capabilities in flow measurements of mouse embryos [19], which can provide valuable information for developmental biology. The investigations of adult mouse vascular and cardiac systems [21] and tumor microcirculation [20] allow longitudinal studies of disease evolution and development of new drug and treatment strategies (see Fig. 1.3) [7]. Furthermore, high-frequency ultrasound has been used for the guided injection of genetic material to specific sites in mouse organs as well as developing mouse embryos [24]. With the aid of contrast agents, high-frequency ultrasound was also shown to be able to detect blood perfusion and quantify flow rate in the capillary body of the rabbit eye [25]. The incorporation of contrast agents with high-frequency ultrasound enables the development of novel flow estimation techniques [25] and offers opportunities for drug delivery [26].

1.2.1 Mechanical Scanning Techniques

Because high-frequency arrays are not commercially available, high-frequency ultrasound systems involve mechanically scanning a single-element transducer [10]. Therefore, unlike array systems with electronic scanning, the frame rate in high-frequency ultrasound is greatly dependent on the scan speed of the transducer. The initial mechanical scanning technique, called the step scan or discrete scan [10], translates the transducer to a series of discrete positions, as illustrated in Fig. 1.4. The spacing between adjacent positions is typically on the order of a fraction of the excitation wavelength [10]. In flow velocity estimation using pulsed waves, several transmissions repeatedly interrogate the same region of interest at each scan position.

Because the transducer needs to be stopped and re-started during data acquisition, the step-scan technique is time consuming and makes it difficult to implement real-time color flow imaging [14].

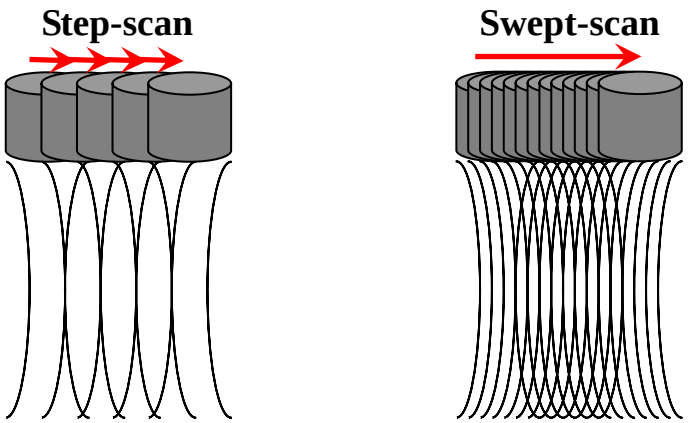

Fig. 1.4. Diagrams for two main mechanical scanning schemes: step scan (left) and swept scan (right). In the step-scan technique, the transducer is translated to a series of discrete positions. At each scan position, repeated firings are used to interrogate the same sample volume. In the swept-scan technique, the transducer is moved continuously while transmitting and receiving. The sample volume for each transmission event is not the same but overlapped closely.

To speed up data acquisition and improve the frame rate, an alternative technique, called the swept scan or continuous scan, was proposed [14]. In the swept-scan technique, the transducer is translated continuously while pulse-echo data are being acquired. The spacing between adjacent scan lines is determined by the transducer speed and the PRI. Unlike the step-scan method, flow velocities in a swept scan are directly evaluated by extracting data from overlapping but different sample volumes. In this case, to maintain sufficient correlation between successive scan data, the scan line interval is typically much less than that in a step scan [14].

Ideally, compared to the step scan, the frame rate improvement from the swept scan is approximately by a factor of $N_R \Delta x / \Delta s$, where N_R and Δs are the number of firings and the scan line interval in a step scan, respectively, and Δx denotes the scan line interval in a swept scan. Given $\Delta s = \lambda/2$, $\Delta x = \lambda/18 \sim \lambda/9$ and $N_R = 4 \sim 16$ (for Color Doppler), the frame rate for the swept scan is maximally nearly four times faster than that for the step scan. In practice, when considering the motor speed control in a step scan (i.e., acceleration and deceleration stages between neighboring scan lines), the frame rate improvement for the swept scan is larger than the aforementioned value [14].

Another potential advantage of the swept-scan method is in the use of a wall filter [14], [27]. The wall filter is used to remove clutter signals from stationary or slow-moving surrounding tissues and retain flow signals. Generally, the infinite-impulse-response (IIR) filter is of interest because only a few filter orders can achieve the narrow transition band [28], [29]. However, IIR filters exhibit the transient response such that the first few flow data are often discarded. This has a significant effect in a step scan because only 4–16 flow data are available. Applying initialization techniques to IIR filters can reduce the transient response but at the expense of yielding a wide transition band [29]. In contrast, because the flow data in a swept scan are continuously sampled in the transducer scanning direction, the IIR filter can be applied over the whole frame and thus the transient response is only present at the beginning of the image [14].

1.2.2 Difficulties in High-frequency Flow Estimation

Although high-frequency ultrasound is attractive for its better spatial and velocity resolutions, many difficulties and limitations in high-frequency flow velocity estimation exist. One of the primary disadvantages is the limited penetration depth resulting from frequency dependent attenuation. Moreover, a single-element transducer with a fixed focus is used. Both factors lead to an insufficient signal-to-noise ratio (SNR) at the ranges away from the focus. Consequently, high-frequency ultrasound is limited to investigate the vessels at superficial depths (less than 20 mm) [7]. Robust flow estimation techniques are therefore particularly needed for high-frequency flow estimation.

In addition, though the swept-scan technique allows near real-time flow estimation, effects of continuously scanning the transducer on accuracy of velocity estimation have not been studied comprehensively. Due to the translation of the transducer, the flow data between neighboring scans decorrelate as a function of the scanning position [14][16][30]. Such decorrelation degrades the performance of axial velocity estimation using correlation techniques.

Another difficulty in high frequency flow measurement is that slow flow velocity estimation is susceptible to the presence of clutters from surrounding tissues [16], especially when a large sample volume is used to improve the SNR. The spectral overlap between the flow and clutter signals might result in a large velocity estimate bias even if a wall filter is applied. A straightforward method to overcome this problem is to increase the PRI (see (1.3)). As a result, when the swept-scan technique is adopted, the performance of velocity estimation is greatly dependent on the scan

speed. Therefore, the choice of an adequate scan speed becomes critical. The system needs to be adjusted appropriately according to the velocity range of interest.

Finally, quantitative velocity estimation using Doppler principles in high-frequency ultrasound requires knowledge of the flow direction. Conventional Doppler-based techniques introduced in Section 1.1 can only measure the velocity component parallel to the beam. The velocity component perpendicular to the beam (i.e., the lateral direction) produces no frequency shift and thus cannot be detected. As a result, a large bias of velocity estimation occurs when the beam-vessel angle is large. To precisely estimate the velocity with Doppler-based methods, the angle needs to be known. Current commercial ultrasound scanners allow operators to perform angle correction manually. This is done by marking a line along the vessel to be investigated from the B-mode image [2]. This technique works well only if the vessel is clearly visible. For small vessels, however, the Doppler angle might be difficult to measure simply from the B-mode image. Hence, an efficient 2-D velocity or angle estimation method in high-frequency ultrasound is of particular demand.

1.3 Vector Velocity Estimation Methods

Quantitative flow velocity estimation is of clinical value. For example, the volumetric flow rate, defined as the product of the vessel cross sectional area and the flow velocity, is an important indicator for many circulatory diseases. For small animal models, measuring the volumetric flow rate over time helps to study arterial, venous, and microvascular thrombosis [21], [23]. Conventional Doppler-based velocity estimation techniques are angle dependent and fail to obtain the complete flow information. To overcome this problem, several techniques aiming at estimating either the Doppler angle or the velocity vector have been intensively investigated in low-frequency ultrasound [31]–[42]. These techniques mainly include multiple beam methods [31], [32], spatial quadrature methods [33], [34], speckle tracking methods [35]–[37], and spectral-broadening-based methods [38]–[42]. Details of these methods are described below, and possibilities of their applications to high-frequency ultrasound are examined.

1.3.1 Multiple Beam Methods

Multiple beam methods are still based on Doppler principles, but employ two or more beams to measure additional velocity components projected on these beam

directions [31]. Fig. 1.5 depicts a typical multiple beam approach using two transducers to estimate the Doppler angle. Two beams generated simultaneously by two different transducers are properly oriented so that they are overlapped with each other at the region of interest. The individual velocity component along the corresponding beam is then measured. Since the angle between the two beams is known, combining it with two velocity estimates by using the triangulation method can yield the Doppler angle and the velocity vector. Extending the two-beam to three-beam technique can obtain the three-dimensional velocity vector [32]. Note that this method can also be realized with a single array that is divided into several sub-apertures.

The main drawback of multiple beam methods is system complexity. Moreover, to obtain accurate velocity vector estimation, the angles between beams are required to be large enough, making this method difficult to implement in cardiac applications.

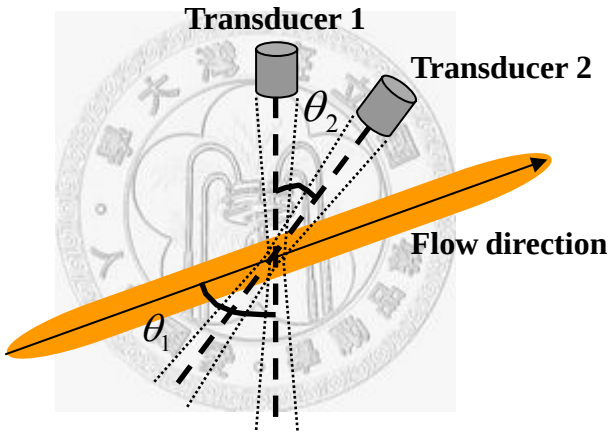

Fig. 1.5. Multiple beam methods using two transducers.

1.3.2 Spatial Quadrature Methods

The spatial quadrature method was proposed separately by Anderson [33] and Jensen [34]. The basic idea behind this method is to generate a modulation on the radiation field along the lateral direction. In doing so, the lateral velocity component can produce the frequency shift along this direction in a manner similar to the conventional Doppler effect. Such a lateral modulation can be generated by combining two appropriate apodization functions across the receive aperture. Hence, a parallel receive processing is necessary. A simple way to produce a lateral modulation is to let the spatial frequency response of the point spread function (PSF), or equivalently, the effective aperture of the pulse-echo response, become single-sided [33]. This leads to a decrease in the spatial resolution. Due to the apodization imposed

on the receive aperture, it is not clear whether the SNR is an issue for this method. Moreover, before performing the lateral velocity estimation, it is essential to align the received signals according to the estimated axial velocity component. Consequently, any misalignment may lead to the estimation error of the lateral velocity.

1.3.3 Speckle Tracking Methods

Speckle tracking methods are non-Doppler-based methods. They are capable of detecting motion and displacement between two different images, and have therefore been widely studied in many ultrasonic applications, such as strain estimation [43], motion compensation for freehand 3-D imaging [44], and flow estimation [35]–[37]. Basically, speckle tracking methods track the speckle pattern produced by the scatterers within a vessel over successive B-mode images using a pattern matching algorithm, such as cross-correlation [35] and sum-absolute-difference [36]. Fig. 1.6 shows an illustration of the search process in a typical 2-D speckle tracking approach. A kernel for velocity estimation is selected in a reference image (left panel), and then tracked within a predefined search region to find the best match in the next image (right panel). Clearly, the spatial resolution of velocity estimation is determined by the kernel size, whereas the search region size determines the maximum detectable velocity. Once the displacement between the kernel and the best match pattern is identified, the velocity vector for this kernel can be calculated according to the time interval between the reference and the search images.

Compared to other techniques, the primary disadvantage of speckle tracking methods is computational complexity. In addition, decorrelation between two speckle patterns degrades accuracy of velocity estimation, especially when the axial component is large or the Doppler angle is small [36]. Therefore, rapid image acquisition is required and the performance of this method applied in a mechanical-scan system is limited. Note that compared to transducer arrays capable of dynamic focusing, such decorrelation becomes more pronounced when a transducer with a fixed focus is used. To speed up data acquisition and decrease speckle decorrelation, Bohs *et al.* incorporated parallel receive beamforming into the original speckle tracking [37]. This method, named ensemble tracking, allows smaller translation between the speckle patterns at the expense of the velocity resolution. Even though ensemble tracking is more computationally efficient, the requirement of a transducer array capable of performing parallel beamforming limits its usage in high-frequency ultrasound.

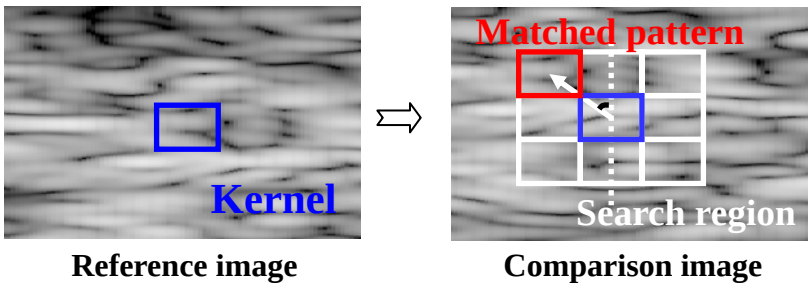

Fig. 1.6. Illustration of the speckle tracking method for vector velocity estimation. A kernel in which the velocity is estimated is selected from a reference image, and then compared with other regions within a predefined search region in successive images using a pattern matching algorithm.

1.3.4 Spectral-broadening-based Methods

The velocity component perpendicular to the beam axis can be estimated using the bandwidth of the Doppler spectrum. The relationship between them is described by the transit-time spectral-broadening effect [38]. The transit time is defined as the time it takes for a scatterer to travel across the sample volume [1]. As illustrated in Fig. 1.7, if the transit time of scatterers is determined by the sample volume width rather than its axial length, then the time duration of the Doppler signal at the slow-time axis is inversely proportional to the lateral velocity component of moving scatters. The resulting Doppler bandwidth is therefore proportional to the lateral velocity component [38].

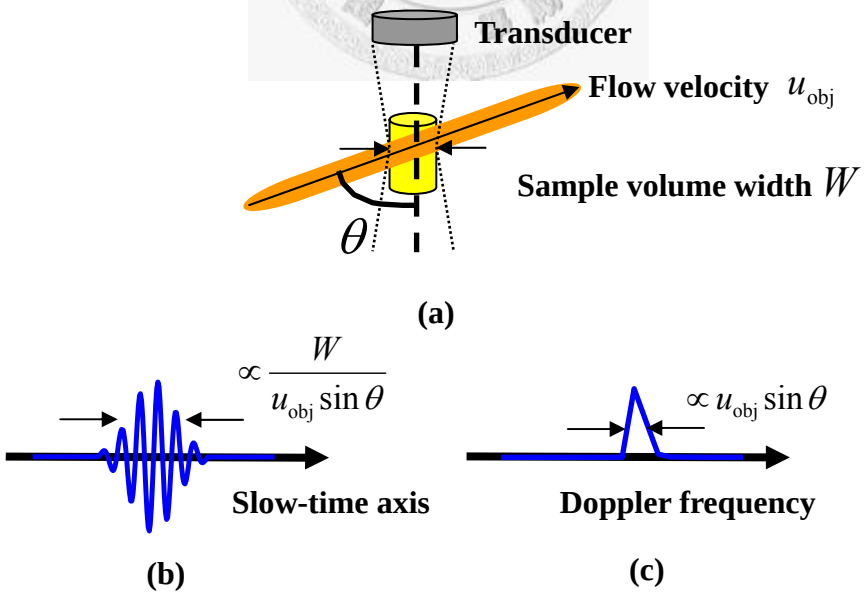

Fig. 1.7. The spectral-broadening-based vector velocity estimator. (a) Illustration of a vessel intersected with a beam by a angle of θ. (b) The received signal along the slow-time axis. (c) The corresponding Doppler spectrum with its bandwidth proportional to the lateral velocity component of moving targets.

Because only a single-element transducer is required, this method is attractive for high-frequency ultrasound. However, the success of this method relies on accuracy of the bandwidth estimation. Moreover, to assure the Doppler bandwidth is determined by the transit time, the observation time has to be longer than the transit time [40]. Therefore, a long data acquisition time is required, which makes this method originally only suitable for non-real-time Doppler modes such as Spectral Doppler [42]. The feasibility of this method in real-time applications was firstly investigated by Li *et al.* [40]. They employed a correlation-based method with spatial and/or temporal averaging schemes to reduce the data acquisition time. Without using any averaging scheme, Yeh and Li further suggested an extrapolation method to efficiently increase the observation time [41]. Besides, the performance of spectral-broadening-based methods is also affected by velocity gradients [41]. Velocity variations within the sample volume may broaden the spectrum and make the bandwidth estimation incorrect.

While spectral-broadening-based methods are suitable for high-frequency ultrasound in terms of system and computational complexity, applying them to a swept-scan system is still problematic. In this case, the transducer movement also affects the spectral bandwidth and, consequently, the accuracy of lateral velocity estimation. Therefore, the relationship between the lateral velocity component and the spectral bandwidth in swept scanning needs to be quantified.

1.4 A Brief Introduction to *K*-space

K-space is a spatial frequency domain description of an imaging system and the targets [38]. Typically, the *k*-space representation of the imaging system is the 2-D Fourier transform of the system's PSF. A complete formula regarding the *k*-space theory can be found in [45], which is originally derived based on the use of either a linear array with electronic scanning or a single-element transducer with mechanical step scanning. Here, we consider the case in a step scan. Let x-axis (the lateral direction) and z-axis (the axial direction) denote the transducer translation direction and the center scan line, respectively, as illustrated in Fig. 1.8(a). For a point target located at a focal range of z_f on the z-axis that is much larger than the aperture size, Walker and Trahey showed that the corresponding k-space representation $P_{ST}(f_x, f_z)$ is given by [45]

$$P_{\mathrm{ST}}(f_x, f_z) = \frac{G}{f_z^2} e^{-j2\pi f_z z_\mathrm{f}} B_{\mathrm{PE}}(-cf_z/2)\, A_{\mathrm{T}}(-2z_\mathrm{f} f_x / f_z) * A_{\mathrm{R}}(-2z_\mathrm{f} f_x / f_z), \qquad (1.4)$$

where f_x and f_z represent the lateral and axial spatial frequencies, respectively, c is the sound velocity, G is a scaling factor related to the target reflectivity, $A_{\mathrm{T}}(x)$ and $A_{\mathrm{R}}(x)$ denote the transmit and receive aperture functions, respectively, $B_{\mathrm{PE}}(f_t)$ denotes the pulse-echo frequency response (where f_t is the temporal frequency and equal to $cf_z/2$), and '$*$' denotes the convolution with respect to f_x. The exponential term results from the linear phase change with increasing range. The transmit and receive aperture functions are real for the target at the focus, but can be complex by additionally imposing a phase curvature to account for the distance difference between the target depth and the focus.

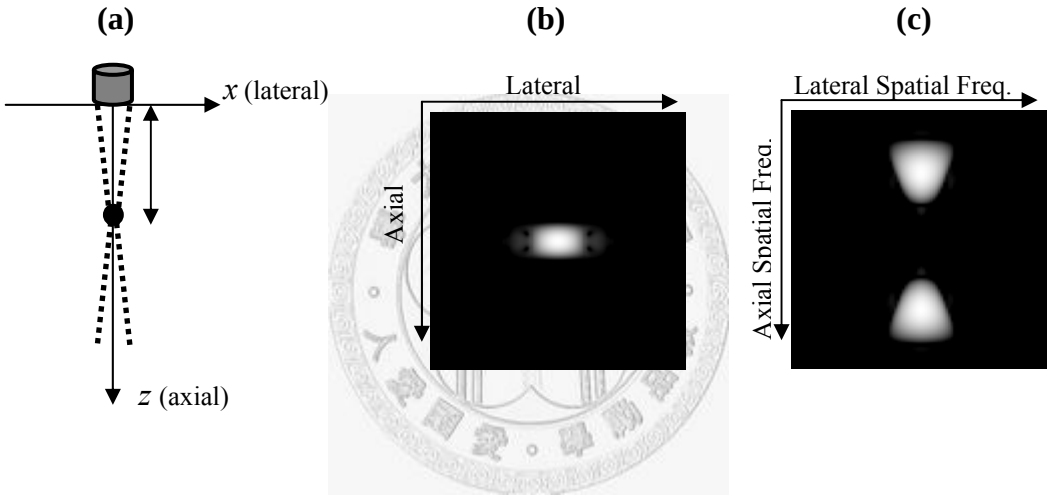

Fig. 1.8. The PSF (middle) and its k-space representation (right) for a stationary object located at the focus in a step scan (left). Both images are displayed over a 50-dB dynamic range.

(1.4) indicates that the k-space representation at a specific f_z (referred to as the lateral spatial spectrum) is simply the convolution of the transmit and receive aperture functions being spatially scaled and reversed. In other words, the lateral spatial spectrum is a scaled version of the effective aperture of the pulse-echo response. The scaling factor between them (i.e., the aperture index x and f_x) is related by $x = -2z_\mathrm{f} f_x / f_z$. Note that the k-space representation is non-separable in rectangular coordinates (f_x , f_z). The PSF and the associated k-space representation of a stationary object in a step scan are illustrated in Figs. 1.8(b) and (c), respectively. The spectrum along f_z is centered at $\pm 2/\lambda$. The lateral spatial spectrum, on the other hand, is centered at the origin. Meanwhile, the bandwidth of the lateral spatial spectrum increases with increasing f_z. This results from the fact that an increase in the temporal frequency causes a decrease in the wavelength and consequently, an improvement in the lateral spatial resolution.

The *k*-space technique provides a comprehensive tool to analyze many ultrasonic imaging applications, such as spatial/frequency compounding, synthetic aperture techniques, and correlation-based phase aberration correction [45]. In addition, *k*-space was also applied to the analysis of speckle decorrelation caused by velocity gradients in flow estimation [46]. As will be presented in this thesis, *k*-space can also be used to describe 2-D motion in a swept-scan system and offer a new perspective on flow estimation.

1.5 Description of the Experimental Setup

We have previously developed a high-frequency digital ultrasound system for experimental purposes [19]. The system operates at a frequency of 45 MHz and is capable of displaying the B-mode, M-mode, color Doppler and power Doppler imaging. Several advanced imaging techniques, including the synthetic aperture focusing technique [47], [48], the generalized-coherent-factor-based adaptive weighting technique [49], coded excitation schemes, and robust flow estimation methods [5], [6], are employed to enhance its performance. Previous studies for small animal models demonstrated its ability in imaging mouse embryos [19], [47] and detecting tumor microcirculation [20].

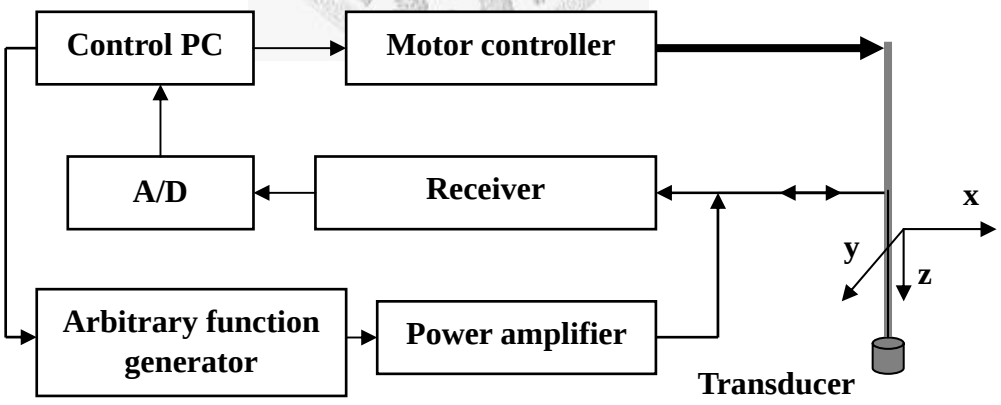

Fig. 1.9. Block diagram of the experimental high-frequency ultrasound system.

The block diagram for the experimental high frequency ultrasound system in this thesis is illustrated in Fig. 1.9. A single-crystal lithium niobate transducer (NIH Resource Center for Medical Ultrasonic Transducer Technology, Penn State University, University Park, PA) has a 45-MHz center frequency with a –6-dB fractional bandwidth of 55%. It is focused at 12 mm and has a diameter of 6 mm (thus

f-number = 2). By using a three-axis mechanical scanning system (CSIM, Taipei, Taiwan), the position of the transducer can be controlled to a precision of 1 μm. During data acquisition, proper acceleration and deceleration stages were employed to avoid the instability of the transducer movement. The transmitting signal was designed by using an 8-bit, 200-Msamples/s arbitrary-function generator (Signatec DAC200, Corona, CA), and then amplified by a power amplifier (Amplifier Research 25A250A, Souderton, PA) before transmission. The received RF signals were enhanced by a pulser/receiver (Panametrics 5900, Waltham, MA) and then sampled by an 8-bit, 200-MHz A/D converter (Signatec PDA500). The sampled data were stored in PC and demodulated to baseband off-line for further processing.

1.6 Scope and Dissertation Organization

The swept-scan technique enables rapid data acquisition in high-frequency ultrasound systems with a single-element transducer. Its effects on the accuracy of velocity estimation are, however, not thoroughly investigated yet. The primary purposes of this thesis are (i) to quantify the effects of both lateral and axial motions in a swept-scan system, and (ii) to develop an efficient and robust vector velocity technique in a swept-scan high-frequency ultrasound system. Specifically, a *k*-space approach is employed to describe the 2-D motion. Based on this modeling technique, an efficient vector velocity estimation algorithm is developed. We refer to this new velocity estimation method as the *k*-space vector velocity estimator.

This thesis is organized as follows. In Chapter 2, the proposed *k*-space modeling technique for 2-D motion in a swept scan is presented. The effects of swept scanning on both Doppler-based axial velocity estimation methods (autocorrelation-based methods) and spectral-broadening-based techniques are investigated theoretically and experimentally. The spectral difference of the flow data between swept and step scanning are also compared. Based on the *k*-space technique, limitations for velocity estimation in a swept-scan system are also analyzed.

In Chapter 3, the proposed *k*-space vector velocity estimator is presented. The required kernel size for the *k*-space vector velocity estimation is determined analytically and confirmed by numerical simulations. Simulations and constant-flow phantom experiments are used to demonstrate the efficacy of the *k*-space vector velocity estimator. In Chapter 4, performance of the *k*-space vector velocity estimator is evaluated experimentally using a flow phantom. In addition, *in vivo* measurements

of the mouse tail vessels are conducted to further investigate its performance. The experimental results are also discussed.

Chapter 5 discusses the applications of the proposed *k*-space estimator in coded excitation systems and electronic-scanning array systems. Moreover, performance of the *k*-space estimator is also compared to that of the conventional spectral-broadening-based techniques in a step scan. This thesis concludes in Chapter 6 with description of future works.

Chapter 2 Effects of Swept Scanning on Velocity Estimation

In order to understand the effects of the swept-scan technique on flow velocity estimation, this chapter employed a *k*-space approach based on the fact that in a swept scan the PSF of a moving target is deformed compared to that of a stationary target. Moreover, different motions result in different PSFs and their corresponding *k*-space representations. Furthermore, it is shown that the main difference between swept and step scanning is in the Doppler bandwidth, which increases linearly with the scanning speed in a swept scan.

Based on the proposed *k*-space modeling, the effects of swept scanning on conventional 1-D and 2-D autocorrelation-based axial velocity estimators [3], [4], as well as the spectral-broadening-based velocity estimation method [40], are examined and investigated experimentally using a 45-MHz transducer. The results indicate that such effects must be corrected in order to obtain accurate estimation of flow velocities.

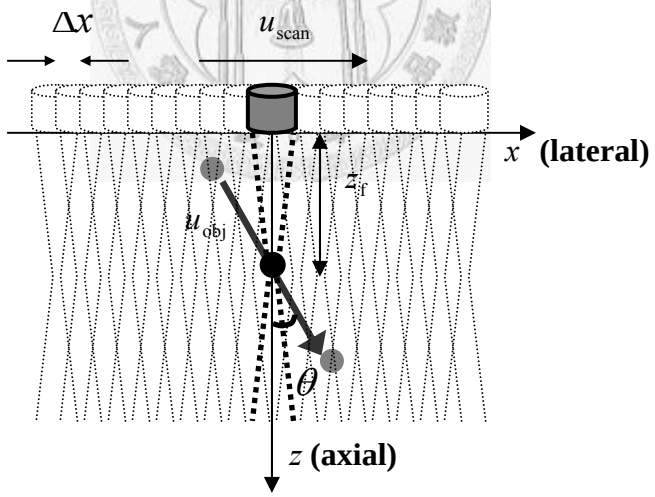

Fig. 2.1. Schematic diagram of the swept-scan technique.

2.1 Basic Principles

Fig. 2.1 provides a schematic diagram for the swept-scan technique and the coordinates used throughout this chapter. The transducer translation direction is

denoted as the x-axis and the z-axis is located at the center scan line. The transducer is scanned continuously at a speed of u_{scan}, and adjacent scan lines are separated by $\Delta x = u_{\text{scan}}$ PRI.

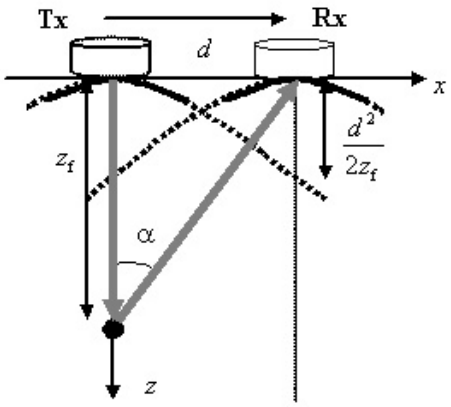

Fig. 2.2. The geometrical relationship of transmission and reception in a swept scan. Note that $d^2/2z_fc$ is the distance accounting for the constant phase difference between the transmit and the receive apertures.

2.1.1 *K*-space Representation in a Swept-scan: a Stationary Object

In (1.4), the k-space representation is derived based on the step scan and is not valid for the swept scan. Consider a stationary object located at a focal range of z_f on the z-axis in a swept scan. As indicated in Fig. 2.2, the transducer has moved a distance of $d = 2z_f u_{\text{scan}}/c$ after the echoes from the object are acquired. In this case, the receive aperture can be expressed as

$$\begin{aligned} A_R(x) &= A_T(x-d)e^{-j2\pi f_t \frac{d^2}{2z_f c}} e^{-j2\pi f_t \frac{(x-d)\sin\alpha}{c}} \\ &= A_T(x-d)e^{j\pi f_t \frac{d^2}{z_f c}} e^{-j2\pi f_t \frac{xd}{z_f c}}, \end{aligned} \tag{2.1}$$

where $\sin\alpha \cong d/z_f$. Compared to the transmit aperture $A_T(x)$, two phase terms are presented in the receive aperture: (i) $\exp(-j2\pi f_t d^2/2z_f c)$ is a constant phase shift that results from the transducer movement, and (ii) $\exp(-j2\pi f_t(x\text{-}d)\sin\alpha/c)$ is a linear phase term as a function of x specifying the steering-angle difference between the transmit and receive apertures. Incorporating (2.1) into (1.4) and recognizing that $f_t = cf_z/2$ and $x = -2z_f f_x/f_z$, the k-space representation in a swept scan $P_{SW}(f_x, f_z)$ is

$$P_{\mathrm{SW}}(f_x, f_z) = \frac{G}{f_z^2} e^{-j2\pi f_z (z_\mathrm{f} - \frac{d^2}{4z_\mathrm{f}})} B_{\mathrm{PE}}(-cf_z/2)\, A_{\mathrm{T}}(-2z_\mathrm{f} f_x / f_z) * A_{\mathrm{T}}(-2z_\mathrm{f} f_x / f_z - d) e^{j2\pi f_x d}. \tag{2.2}$$

Note that $d = 0$ is the result for the step scan. Considering the case where the transducer aperture function is uniformly weighted (i.e., unapodized) with a width of a, (2.2) becomes

$$\begin{aligned} P_{\mathrm{SW}}(f_x, f_z) &= G'(f_z)\Pi\left(\frac{f_x}{f_z/2f_{\mathrm{num}}}\right) * \Pi\left(\frac{f_x + df_z/2z_\mathrm{f}}{f_z/2f_{\mathrm{num}}}\right) e^{j2\pi f_x d} \\ G'(f_z) &= \frac{G}{f_z^2} e^{-j2\pi f_z (z_\mathrm{f} - \frac{d^2}{4z_\mathrm{f}})} B_{\mathrm{PE}}\left(\frac{-cf_z}{2}\right), \end{aligned} \tag{2.3}$$

where $f_{\mathrm{num}} = z_\mathrm{f}/a$ represents the f-number and $\Pi(\bullet)$ denotes the rectangular function. Let $m = f_z/2f_{\mathrm{num}}$ and $n = f_z/2z_\mathrm{f}$; (2.3) then yields

$$\begin{aligned} P_{\mathrm{SW}}(f_x, f_z) &= G'(f_z)\int \Pi\left(\frac{f_x - \xi}{m}\right)\Pi\left(\frac{\xi + nd}{m}\right) e^{j2\pi\xi d}\,\mathrm{d}\xi \\ &= G'(f_z)\begin{cases} 0, & f_x \le -m - nd \quad \text{or} \quad f_x \ge m - nd \\ \frac{1}{\pi d}\sin(\pi(f_x + m + nd)d)\, e^{j\pi d(f_x - nd)}, & -m - nd \le f_x \le -nd \\ \frac{1}{\pi d}\sin(\pi(-f_x + m - nd)d)\, e^{j\pi d(f_x - nd)}, & -nd \le f_x \le m - nd \end{cases}. \end{aligned} \tag{2.4}$$

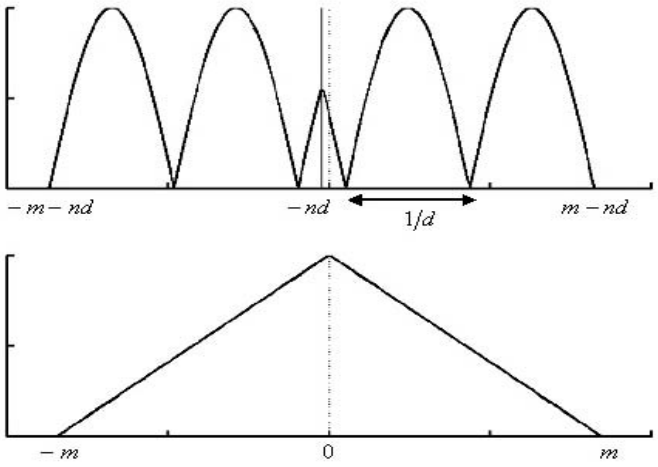

Fig. 2.3. Comparison of the lateral spatial spectrum between swept scanning (top panel) and step scanning (bottom panel) under the condition where a stationary target is at the focus and the transducer aperture function is rectangular. $m = f_z/2f_{\mathrm{num}}$, $n = f_z/2z_\mathrm{f}$, and f_{num} denotes the f-number.

According to (2.4), Fig. 2.3 compares the lateral spatial spectrum between swept and step scanning. It is shown that the lateral spatial spectrum in the swept scan is symmetric with respect to $f_x = -nd = -u_{\text{scan}} f_z / c$, with a zero-to-zero bandwidth of $2m$. On each side of the symmetry axis, the spectrum is sinusoidal with a period equal to $2/d$. In contrast, the lateral spatial spectrum in step scanning is an even, triangular function with the same bandwidth of $2m$. Accordingly, for a stationary object, swept scanning of a transducer produces both a shift and an oscillation in the lateral spatial spectrum.

In most applications the transducer scan speed is within the range 1–100 mm/s, depending on the flow velocity range of interest. In this case, $f_x d << \pi$ for f_x corresponding to the nonzero spectrum values, and hence (2.2) can be approximated as (see Appendix A)

$$P_{\text{SW}}(f_x, f_z) \cong \frac{G}{f_z^2} e^{-j2\pi f_z z_{\text{f}}} B_{\text{PE}}(-cf_z/2)\, e^{j\pi f_x d} \left[A_{\text{T}}(-2z_{\text{f}} f_x / f_z - d/2) * A_{\text{T}}(-2z_{\text{f}} f_x / f_z - d/2) \right] \tag{2.5}$$

Moreover, the lateral spectral shift (i.e., nd) caused by the swept scanning is at least four orders of magnitude smaller than the lateral spectral bandwidth (i.e., $2m$). Hence, (2.5) can be further simplified to

$$P_{\text{SW}}(f_x, f_z) \cong \frac{G}{f_z^2} e^{-j2\pi f_z z_{\text{f}}} B_{\text{PE}}(-cf_z/2)\, e^{j\pi f_x d} \left[A_{\text{T}}(-2z_{\text{f}} f_x / f_z) * A_{\text{T}}(-2z_{\text{f}} f_x / f_z) \right] \tag{2.6}$$

With such an approximation, the k-space representation for the swept scan is simply that for the step scan multiplied by a phase term $\exp(j\pi f_x d)$. The two scan methods exhibit identical spatial spectra (i.e., the magnitude of the k-space representation). Therefore, if the scan speed is much less than the sound velocity, both (2.6) and the bottom panel of Fig. 2.3 indicate two important properties regarding the lateral spatial spectrum when the target is at the focus and the transmit and receive apertures are identical and even functions: (i) the lateral spatial spectrum for a given f_z is an even function of f_x, and (ii) when each lateral spatial spectrum is normalized to its maximum, its bandwidth is proportional to f_z / f_{num}.

2.1.2 *K*-space Representation in a Swept-scan: 2-D Motion

Now consider an object moving at a velocity of u_{obj} and with a Doppler angle of θ, as indicated in Fig. 2.1. Assume that the object arrives at the focal point on the center scan line while the transducer is scanning this line. Fig. 2.4 shows the simulation results of the contour maps for the PSFs (left panels) and the associated

k-space representations (right panels) under different motion conditions. The velocity vector was fixed at 30 mm/s except for Fig 2.4(d), where 10 mm/s was used. The Field II ultrasound simulation program [50] was used with the simulation parameters listed in Table 2.1. Fig 2.4(a) shows the results for a stationary object. The left panel of Fig. 2.4(b) shows the PSF of the object moving axially away from the transducer (θ = 0°). It can be seen that its PSF deforms along the axial dimension relative to that of a stationary object. In general, if the axial displacement is less than the depth of field, the echoes of two successive scan lines are shifted axially, but weighted with different sound intensities. Such a shift is equal to the product of the axial velocity and the PRI.

Table 2.1. Simulation parameters used in the thesis

Simulation parameter	Value
Sound velocity (c)	1.48 mm/μs
Center frequency	40 MHz
Transducer fractional bandwidth	55%
Diameter of transducer (a)	6 mm
Focal length of transducer (z_f)	12 mm
Transducer scan speed (u_{scan})	20 mm/s
Pulse repetition interval (PRI)	100 μs
Transmission pulse	two-cycle sinusoid
Lateral sampling interval (Δx)	2 μm
Axial sampling interval (Δz)	3.7 μm

The left panels of Figs. 2.4(c) and (d) show the PSFs of an object moving laterally in the opposite ($\theta = -90°$) and the same ($\theta = 90°$) directions of the scanning, respectively. Compared to the PSF of a stationary object, the PSF in Fig. 2.4(c) is compressed in the lateral dimension while that in Fig. 2.4(d) is expanded, which is due to the relative lateral motion between the transducer and the object changing the lateral width of the PSF. In both cases, however, the PSFs in the axial dimension remain unchanged. For example, if the object and the transducer move with opposite velocities, the lateral width of the resulting PSF is half that of a stationary object. On the other hand, if the object moves synchronously with the transducer (i.e., the relative lateral velocity is zero), the resulting PSF is constant along the lateral dimension (i.e., its lateral width is infinite). Accordingly, the lateral width of the PSF varies with the relative lateral velocity over the transducer speed.

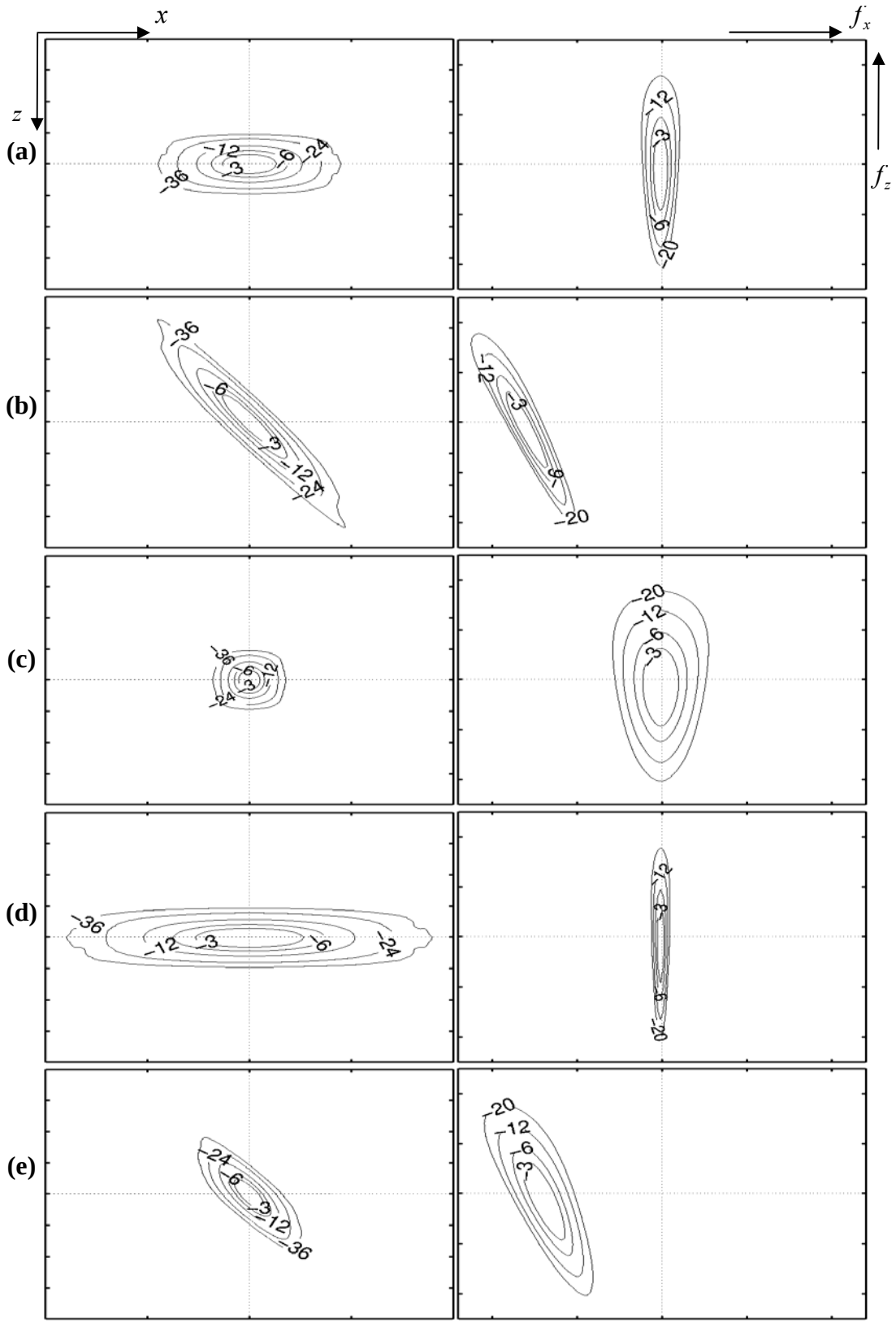

Fig. 2.4. Contour maps for PSFs (left panels) and the *k*-space representations (in baseband form, right panels) under different motion conditions with a vector velocity of 30 mm/s (except for (d), in which 10 mm/s was used). (a) Stationary object. (b) Axially moving object with $\theta = 0°$. (c) Laterally moving target with $\theta = -90°$. (d) Laterally moving target with $\theta = 90°$. (e) 2-D moving object with $\theta = -30°$.

Based on the above discussion, assuming the axial displacement is within the depth of field, the PSF $p_{\mathrm{SW\_motion}}(x, z)$ for a 2-D moving object in a swept scan can be expressed as

$$p_{\mathrm{SW\_motion}}(x,z) = p_{\mathrm{SW}}(|1 - v\sin\theta|x, z - xv\cos\theta), \tag{2.7}$$

where $v = u_{\mathrm{obj}}/u_{\mathrm{scan}}$, and $p_{\mathrm{SW}}(x, z)$ represents the PSF of a stationary object in a swept scan (i.e., the inverse Fourier transform of (2.6)). The use of the absolute value results from the lateral symmetry of the sound field generated by the transducer: the PSF scaled by $1-v\sin\theta$ is identical to that scaled by $v\sin\theta-1$. As shown in (2.7), the axial velocity component $u_{\mathrm{obj}}\cos\theta$ causes an axial shift in the PSF, whereas the lateral velocity component $u_{\mathrm{obj}}\sin\theta$ broadens or narrows the PSF in the lateral dimension. This is demonstrated in the left panel of Fig. 2.4(e) where the object moving with $\theta =$ –30°. By taking a 2-D Fourier transform of $p_{\mathrm{SW\_motion}}(x, z)$, the corresponding k-space representation $P_{\mathrm{SW\_motion}}(f_x, f_z)$ is given by

$$\begin{aligned} P_{\mathrm{SW\_motion}}(f_x, f_z) &= \iint p_{\mathrm{SW\_motion}}(x,z)e^{-j2\pi f_x x}e^{-j2\pi f_z z}\mathrm{d}x\mathrm{d}z \\ &= \iint p_{\mathrm{SW}}(|1 - v\sin\theta|x, z - xv\cos\theta)e^{-j2\pi f_x x}e^{-j2\pi f_z z}\mathrm{d}x\mathrm{d}z \\ &= \iint p_{\mathrm{SW}}(|1 - v\sin\theta|x, z')e^{-j2\pi(f_x + f_z v\cos\theta)x}e^{-j2\pi f_z z'}\mathrm{d}x\mathrm{d}z' \\ &= \frac{1}{|1 - v\sin\theta|}P_{\mathrm{SW}}\left(\frac{f_x + f_z v\cos\theta}{|1 - v\sin\theta|}, f_z\right), \end{aligned} \tag{2.8}$$

where $P_{\mathrm{SW}}(f_x, f_z)$ is as given in (2.6). The axial shift in the PSF leads to a shift in the lateral spatial spectrum proportional to the axial velocity component and f_z. For the lateral motion, each lateral spatial spectrum is broadened by $|1-v\sin\theta|$. The right panels of Fig. 2.4 demonstrate the k-space representations that (2.8) predicts. Based on (2.8), Fig. 2.5 further schematically illustrates the k-space representation of a 2-D moving object. Note that the center of each shifted lateral spatial spectrum is on the line passing through the origin of the entire frequency plane, with a slope of $-1/v\cos\theta$.

Based on (2.6) and (2.8), the bandwidth bw_k of the lateral spatial spectrum at a given f_z can be expressed as

$$bw_k(f_z) = \gamma\frac{f_z}{f_{\mathrm{num}}}\left|1 - \frac{u_{\mathrm{obj}}\sin\theta}{u_{\mathrm{scan}}}\right| = \gamma\frac{f_z|u_{\mathrm{rel}}|}{u_{\mathrm{scan}}f_{\mathrm{num}}}, \tag{2.9}$$

where γ is related to the aperture weighting function and the threshold used to determine the bandwidth, and $u_{rel} = u_{scan} - u_{obj}\sin\theta$ represents the relative lateral velocity between the transducer and the object. Based on (2.9), the lateral velocity component can be obtained by estimating the bandwidth of each lateral spatial spectrum.

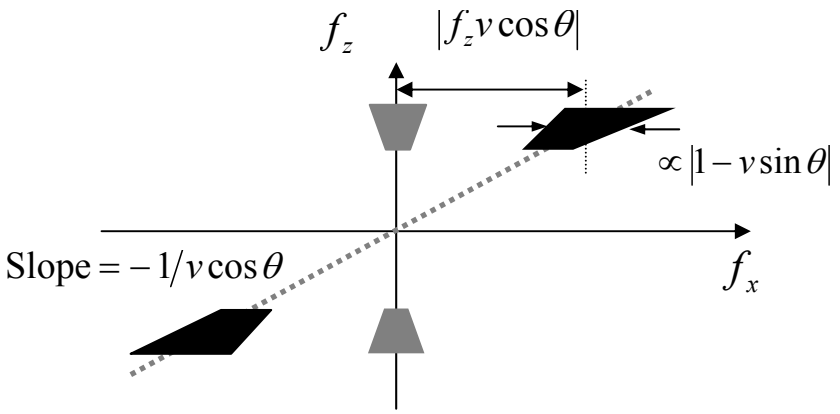

Fig. 2.5. *K*-space representations for a stationary object (light) and an object moving at a Doppler angle of θ (heavy). v is the ratio of the object velocity to the scan speed.

2.1.3 Comparison Between Swept and Step Scanning

Unlike conventional step-scan flow estimations performed in the temporal or temporal frequency domains [51], [52], the *k*-space motion modeling in swept scanning described in (2.8) is presented in the spatial frequency domain. To understand the impact of swept scanning on velocity estimation, it is necessary to examine the fundamental difference in the flow echoes between the step- and swept-scan methods. For this purpose, the spatial variables x and z are related to the temporal variables by

$$\begin{aligned} x &= u_{scan}\tau, \text{ and} \\ z &= \frac{ct}{2}, \end{aligned} \tag{2.10}$$

where τ is the data acquisition time (i.e., the slow time) and t is the fast time. Let f_D and f_t denote the Doppler and RF frequencies corresponding to the slow and fast times, respectively. Based on (2.10), the corresponding temporal frequency representation $P_{SW\_motion}(f_D, f_t)$ of (2.8) is

$$P_{\mathrm{SW\_motion}}(f_D, f_t) = CP_{\mathrm{SW}}\left(\frac{f_D + 2f_t u_{\mathrm{obj}} \cos\theta / c}{\left|u_{\mathrm{scan}} - u_{\mathrm{obj}} \sin\theta\right|}, \frac{2}{c} f_t\right), \tag{2.11}$$

where C is a scaling factor. Due to the linear relationship between the spatial and temporal (frequency) domains, $P_{\mathrm{SW\_motion}}(f_D, f_t)$ is a scaled version of the corresponding k-space representation $P_{\mathrm{SW\_motion}}(f_x, f_z)$. By applying (2.9) and (2.10), it is readily shown that in (2.11), the Doppler bandwidth bw_D (i.e., the bandwidth along the Doppler frequency dimension) at a given RF frequency f_t is given by

$$bw_D(f_t) = \gamma' \frac{f_t}{cf_{\mathrm{num}}} \left|u_{\mathrm{scan}} - u_{\mathrm{obj}} \sin\theta\right| = \gamma' \frac{f_t \left|u_{\mathrm{rel}}\right|}{cf_{\mathrm{num}}}, \tag{2.12}$$

where γ' is a scaling factor related to the aperture weighting function and the bandwidth threshold. In contrast to (2.9), here the Doppler bandwidth is directly proportional to u_{rel}.

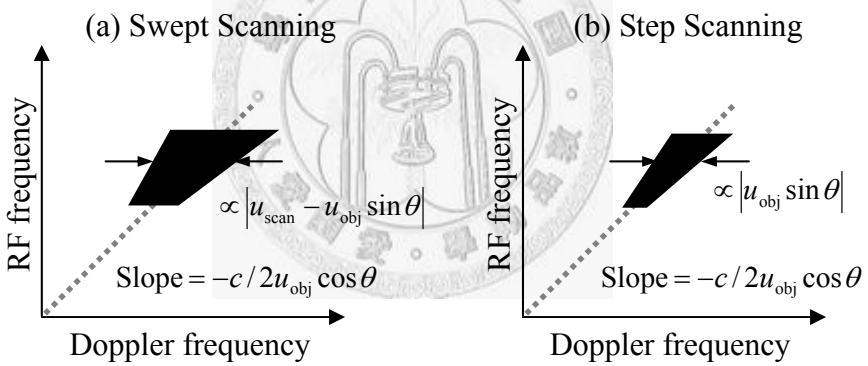

Fig. 2.6. Comparison of the temporal frequency representation for 2-D motion between (a) swept-scan and (b) step-scan methods.

For the step-scan method, the corresponding temporal frequency representation and the Doppler bandwidth can be regarded as a special case of the swept-scan method in which $u_{\mathrm{scan}} = 0$. Fig. 2.6 compares the temporal spectra of the swept- and step-scan methods, which reveals that the only difference is in the Doppler bandwidth. The Doppler bandwidth in a step scan is proportional to the lateral velocity component, which agrees with the results derived from the transit-time spectral broadening effect [38]. In contrast, the Doppler bandwidth in a swept scan is proportional to the relative lateral velocity between the transducer and the moving object. Hence, when the lateral velocity component of the flow velocity is absent, no Doppler spectral broadening occurs in step-scanned flow echoes (i.e., the temporal

spectrum shown in Fig. 2.6(b) becomes a line segment), but an inherent Doppler spectral broadening proportional to the scan speed exists in swept-scanned echoes. Note that in this case, the bandwidth of the lateral spatial spectrum for the swept-scan method is irrelevant to the scan speed (see (2.9)). Fig. 2.6 also indicates that the step-scan method cannot discriminate the direction of the lateral velocity. Nonetheless, two lateral motions with opposite directions in a swept scan result in distinct spectra and hence are distinguishable.

2.2 Effects of Swept-scanning on Vector Velocity Estimation

The 1-D and 2-D autocorrelation-based axial velocity estimation techniques are commonly used for color flow imaging because of their computational efficiency [3], [4]. Conceptually, both estimators obtain the mean axial velocity by using an estimation of the spectral mean frequency: the 1-D autocorrelator estimates the mean Doppler frequency at the center RF frequency [3], and the 2-D autocorrelator estimates the slope of the dotted line in Fig. 2.5 [4] (see Section 1.1.1). As a result, velocity estimation errors increase for both estimators as the spectrum broadens [53]. Since the Doppler spectrum broadens linearly with the scan speed, the axial velocity estimation using the autocorrelation technique is expected to be more erroneous in a swept scan than in a step scan. Moreover, the estimation error is proportional to the relative lateral velocity. The above observations are verified experimentally in Section 2.3.

In swept scanning, the transducer can also be moved back and forth during image data acquisition. According to (2.8), the k-space spectral shift along the f_x-axis in one scan direction is the opposite of the shift in the other direction. Moreover, the lateral spatial bandwidth also changes depending on the relative lateral velocity.

In the following, the mean frequency and the spectral bandwidth estimation in the conventional vector velocity estimation method are further examined in a swept scan in terms of the velocity resolution, aliasing, and the presence of clutter signals. The analyses are based on the k-space modeling in (2.8), and the Doppler angle θ is restricted to within ±90°. For the numerical examples presented below, we assume that both transmit and receive apertures are rectangular (thus, $\gamma = 0.5$ for half the zero-to-zero bandwidth), and a –12-dB threshold is used to determine the lateral spatial bandwidth (hence, $\gamma = 0.38$). The other parameters are listed in Table 2.1.

2.2.1 Velocity Resolution

According to (2.8) and (2.9), if the region of interest (or kernel) selected for the flow estimation spans N_L scan lines, the axial velocity resolution and the lateral velocity resolution will be

$$\begin{aligned}\Delta u_{\text{obj(axial)}} &= \frac{1}{f_z N_L PRI} = \frac{u_{\text{scan}}}{f_z W_x}, \text{ and} \\ \Delta u_{\text{obj(lat)}} &= \frac{f_{\text{num}}}{\gamma f_z N_L PRI} = \frac{f_{\text{num}}}{\gamma}\frac{u_{\text{scan}}}{f_z W_x},\end{aligned} \tag{2.13}$$

respectively, where $W_x = N_L \Delta x$ denotes the lateral kernel width. Note that γ is related to both the bandwidth threshold and the aperture weighting function. A scaling factor of f_{num}/γ exists between the axial and lateral velocity resolutions and, in general, $f_{\text{num}} > \gamma$, for example, $\gamma \leq 0.5$ if the transmit and receive apertures are rectangular. In contrast, the f-number is typically greater than unity. Therefore, the lateral velocity resolution is worse than the axial velocity resolution by a factor of f_{num}/γ. If the lateral kernel width is 8λ, the axial and lateral velocity resolutions at the central axial spatial frequency (i.e., $f_z = 2/\lambda$, where λ is the wavelength) are 1.25 and 6.58 mm/s, respectively.

As also indicated in (2.13), given a lateral kernel size, both the axial and lateral velocity resolutions can be improved simultaneously by decreasing the scan speed (either decreasing Δx or increasing the PRI). This indicates that the velocity resolution is improved at the expense of the frame rate. The lateral velocity resolution can also be improved by reducing the f-number. However, since the bandwidth of the lateral spatial spectrum is inversely proportional to the f-number (see (2.9)), decreasing the f-number increases the variance in the estimated lateral velocity. Therefore, a trade-off exists between the resolution and the variance in the estimated lateral velocity.

2.2.2 Spectral Aliasing

Spectral aliasing limits the maximum detectable velocity in Doppler-based estimations [1]. This aliasing occurs if the maximum lateral spatial frequency exceeds half the sampling rate along the lateral dimension; i.e.,

$$\frac{u_{\text{obj}} \cos\theta}{u_{\text{scan}}} f_z + \gamma \frac{f_z}{f_{\text{num}}}\left(1 - \frac{u_{\text{obj}} \sin\theta}{u_{\text{scan}}}\right) \geq \frac{1}{2\Delta x}. \tag{2.14}$$

We focus our discussion on the center axial spatial frequency. Note that the aliasing worsens at higher axial spatial frequencies. To avoid aliasing, the velocity has to satisfy

$$u_{\text{obj}} \le \frac{\lambda/4PRI - \gamma u_{\text{scan}}/f_{\text{num}}}{\cos\theta - \gamma \sin\theta/f_{\text{num}}}. \tag{2.15}$$

It can be readily seen that if $f_{\text{num}}^2 >> \gamma^2$ (which is valid in our case), to assure that aliasing is absent at all Doppler angles, the maximum detectable velocity $u_{\text{obj(max)}}$ is

$$u_{\text{obj(max)}} = \frac{\lambda}{4PRI} - \frac{\gamma}{f_{\text{num}}} u_{\text{scan}}, \tag{2.16}$$

which is $\gamma u_{\text{scan}}/f_{\text{num}}$ less than that for step scanning indicated in (1.3). The maximum detectable velocity increases as the PRI or Δx decreases. Thus, increasing the scan speed does not necessarily increase the maximum detectable velocity. The effects of the scan speed on the maximum detectable velocity are shown in Fig. 2.7, in which each solid line depicts the variation in the maximum detectable velocity as a function of the PRI, and each dashed line indicates the variation as a function of Δx. Note that the solid line marked as 'Δx = 0 μm' is the maximum detectable velocity in step scanning. The figure shows that for a constant scan speed, different combinations of Δx and the PRI give rise to different maximum detectable velocities. The maximum detectable velocity can be improved more by decreasing the PRI than by decreasing Δx. For a given PRI, if $\Delta x << \lambda$, the second term on the right-hand side of (2.16) is much less than the first term, and the maximum dectable velocity in a swept scan is close to that in a step scan. As indicated in Fig. 2.7, if Δx = 2 μm and PRI = 100 μs (i.e., a scan speed of 20 mm/s), the maximum detectable velocity is 88.7 mm/s in a swept scan compared to 92.5 mm/s in a step scan.

Even when spectral aliasing occurs, the velocity can still be estimated correctly by utilizing the 2-D characteristics of the spectrum. One technique to overcome the aliasing is based on the fact that for the aliasing spectrum, the line passing through the center of each lateral spatial spectrum does not pass through the origin of the spatial frequency plane [51]. The velocity estimate can be corrected by detecting such a condition.

In addition, with the swept-scan technique, an aliasing uniquely exists in spectral-broadening-based lateral velocity estimation. As indicated in (2.7) and (2.9), a lateral velocity of u_{scan} (1+s), where s > 0, cannot be discriminated from that of u_{scan} (1−s). The scan speed, therefore, affects the detectable range of lateral velocities in the scanning direction. Increasing the scan speed enlarges the detectable lateral velocity range in the scanning direction, but it also increases the variance in the estimated lateral velocity.

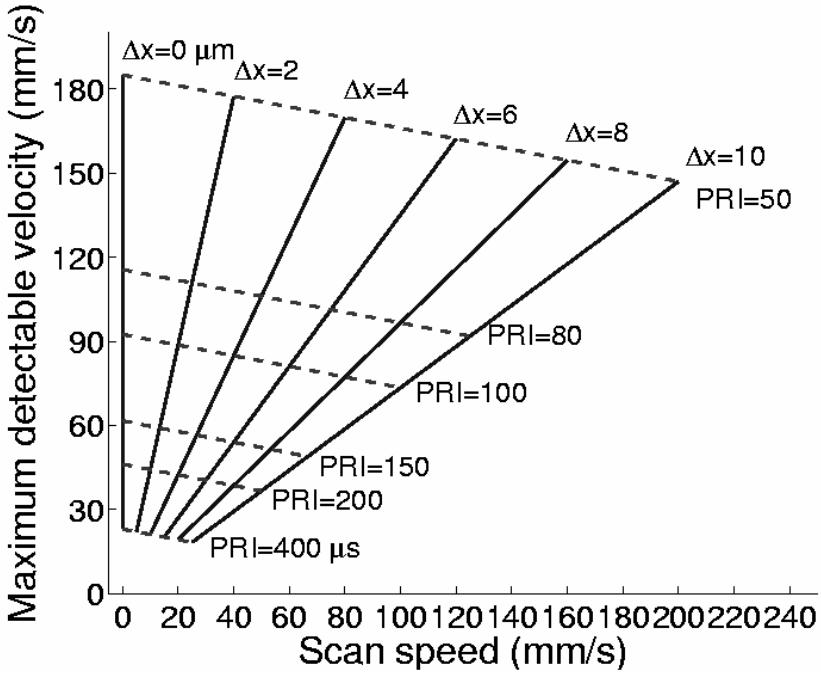

Fig. 2.7. Effects of the scan speed on the maximum detectable velocity. The solid and dashed lines indicate the maximum detectable velocity as functions of the PRI and Δx, respectively.

2.2.3 The Presence of Clutter Signals

In addition to flow signals, the selected kernel may contain clutter signals from surrounding tissues or the vessel walls. Such clutter signals appear in the vicinity of the zero lateral spatial frequency axis and their spectra may overlap those of the flow signals, which may degrade the accuracy of the velocity estimation. This spectral overlapping is more pronounced in swept scanning than in step scanning because the spectra of both the flow and the clutter signals are broadened in a swept scan [16]. The common method to remove clutter signals is to employ a high-pass filter. Nonetheless, if the spectrum overlapping is severe, the wall filter also removes the slow-velocity components of the flow; hence the presence of clutter signals limits the minimum detectable velocity.

In the following analyses, the intensity ratio of the clutter signals to the flow signals is set to unity to simplify the expressions. To avoid spectral overlapping, the spectral shift for the flow in the lateral spatial frequency dimension must be larger than the sum of the lateral spatial bandwidths of the clutter and flow signals; i.e.,

$$\frac{u_{\text{obj}}\cos\theta}{u_{\text{scan}}} f_z \geq \frac{\gamma f_z}{f_{\text{num}}} + \frac{\gamma f_z}{f_{\text{num}}}\left(1 + \frac{u_{\text{obj}}\sin\theta}{u_{\text{scan}}}\right). \tag{2.17}$$

For convenience, the sign in the bracket is changed to a plus. Hence, θ defined in figure 1 becomes $-\theta$. Rewriting (2.17) yields

$$u_{\text{obj}} \geq 2\gamma \frac{u_{\text{scan}}}{f_{\text{num}}} \frac{1}{\cos\theta - \gamma \sin\theta / f_{\text{num}}}. \tag{2.18}$$

Note that (2.18) is independent of the axial spatial frequency. Considering the special case in which only the axial velocity component is present (i.e., θ = 0°), (2.18) becomes

$$u_{\text{obj}} \geq 2\gamma \frac{u_{\text{scan}}}{f_{\text{num}}}. \tag{2.19}$$

Obviously, the minimum detectable velocity in this case is proportional to the transducer speed and inversely proportional to the f-number [16]. For example, for f_{num} = 2 and u_{scan} = 20 mm/s, the minimum detectable velocity is 7.6 mm/s.

Moreover, (2.18) can be rewritten as

$$\theta \leq \theta_{\text{cr}} = \phi - \sin^{-1}\left(\frac{2u_{\text{scan}}}{u_{\text{obj}}} \cos\phi \right), \tag{2.20}$$

where $\phi = \tan^{-1}(f_{\text{num}}/\gamma)$. The above equation states that given a scan speed and a velocity, the Doppler angle θ must be smaller than the critical angle θ_{cr} (i.e., $-90° \leq \theta < \theta_{\text{cr}}$) to avoid the spectra of the clutter and flow signals overlapping. In other words, the critical angle represents the maximum detectable angle in the presence of clutter signals. Based on (2.20), Fig. 2.8 shows the critical angles as a function of velocity for different scan speeds, from which the following observations can be made. First, the spectral overlapping is absent in the region below each curve, and the velocity corresponding to θ_{cr} = 0° is the minimum detectable velocity predicted by (2.19). Second, for each curve, the critical angle increases and saturates to its maximum as the velocity increases. Because the second term on the right-hand side of (2.20) is greater than zero, the critical angle has an upper bound equal to ϕ, which represents the maximum detectable angle in a step scan. In the case of Fig. 2.8, the upper bound of the critical angle is around 80°. The third observation is that both the critical angle and the minimum detectable velocity can be increased simultaneously by reducing the scan speed. Finally, Fig. 2.8 provides a guideline for the choice of scan speed according to the velocity range of interest. For example, for measuring flow velocities around 5 mm/s, the scan speed should be below 5 mm/s to allow assessment over a

wide spatial angle.

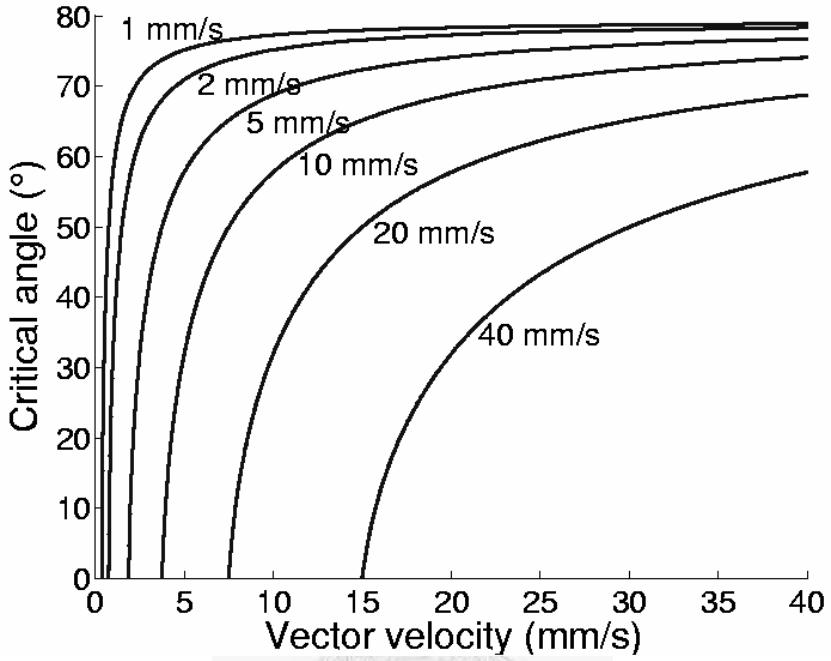

Fig. 2.8. Critical angles as a function of the vector velocity in the presence of clutter signals. Different curves represent different scan speeds.

2.3 Experimental Investigations

Experiments involving speckle phantoms were conducted to investigate Doppler spectral broadening caused by swept scanning and its effect on conventional autocorrelation-based axial velocity estimators. All experiments employed the transmission of three cycles of a 40-MHz sinusoid. The scan speed was varied by changing Δx with a fixed PRI of 100 μs.

2.3.1 Doppler Spectral Broadening for a Stationary Phantom

The proportionality between the Doppler bandwidth and the relative lateral velocity u_{rel}, as indicated in (2.12), was verified experimentally. A gelatin phantom containing graphite powder with uniform distribution was placed in a water tank. The transducer was scanned continuously and laterally to obtain the 2-D scan data set. A kernel around the focus was extracted from the 2-D scan data set, and was then multiplied by a 2-D Hanning window prior to 2-D Fourier transformation. The spatial

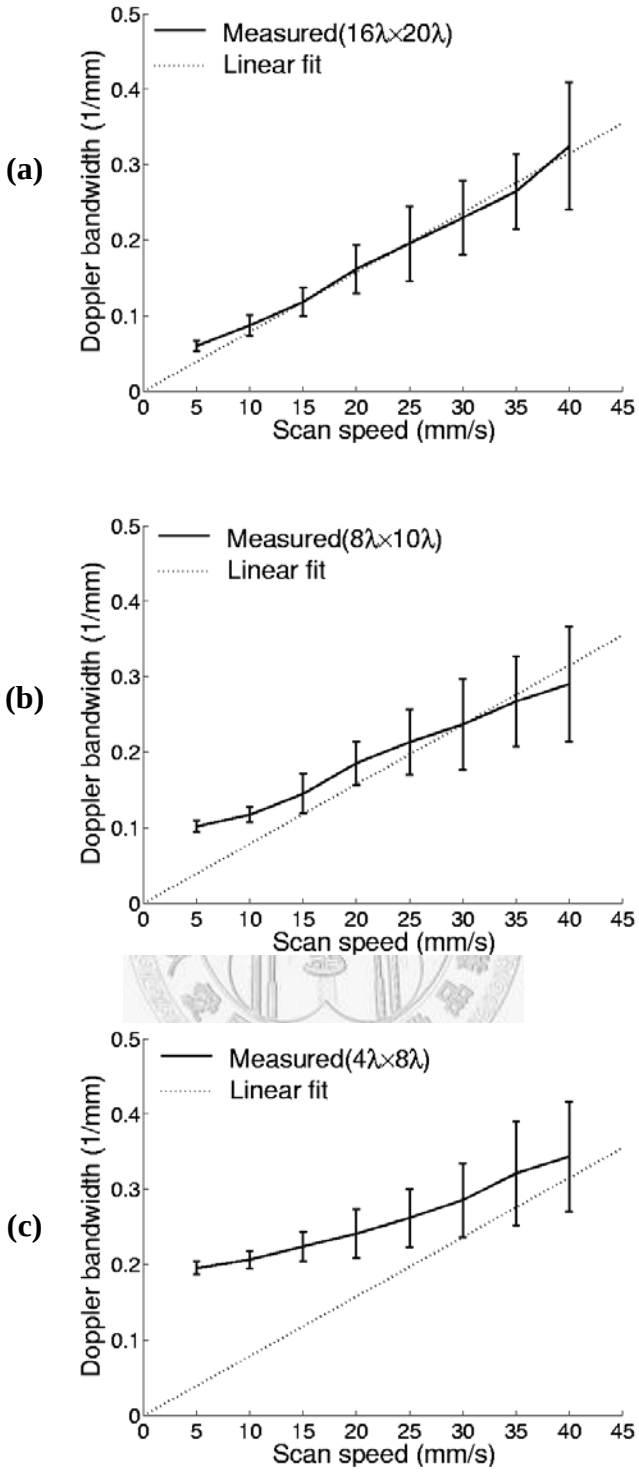

Fig. 2.9. Dependence of the –12-dB Doppler bandwidth on the scan speed (solid line) for a stationary phantom. Three kernels with the following sizes were investigated: (a) 16λ×20λ (lateral × axial), (b) 8λ×10λ, and (c) 4λ×8λ. The error bars represent ± one standard deviation. The dotted lines are identical and are the best linear fits of the estimates with a 16λ×20λ kernel.

spectrum obtained was represented as the corresponding temporal spectrum using (2.11). The dependence of the –12-dB Doppler bandwidth on the scan speed, using different kernel sizes, is shown by the solid lines in Fig. 2.9. Figs. 2.9(a)–(c) show the results with kernel sizes (lateral by axial) of $16\lambda \times 20\lambda$, $8\lambda \times 10\lambda$, and $4\lambda \times 8\lambda$, respectively. The dotted lines are identical and represent the best linear fit of the estimates using a kernel size of $16\lambda \times 20\lambda$. For all the panels, only the Doppler spectrum at the center RF frequency was used to estimate the bandwidth. Thirty independent experiments were performed under each condition to obtain the mean and standard deviation (indicated by error bars). With a $16\lambda \times 20\lambda$ kernel, the Doppler bandwidth is proportional to the scan speed (note that u_{rel} is equal to the scan speed in this study); for an $8\lambda \times 10\lambda$ kernel, such proportionality approximately holds when the scan speed is above 25 mm/s; however, when the scan speed is lower than 25 mm/s, the Doppler bandwidth is overestimated compared to the proportionality line, and this becomes significant for a $4\lambda \times 8\lambda$ kernel. This can be explained by (2.7): as the scan speed decreases, the PSF broadens until its lateral width is larger than the lateral kernel width. In this case, the Doppler bandwidth is dominated by the kernel size. Furthermore, Fig. 2.9 also indicates that the variance of the Doppler bandwidth estimation increases with the scan speed.

2.3.2 Performance of Autocorrelation-based Axial Velocity Estimators

The accuracy of the 1-D and 2-D autocorrelation-based axial velocity estimators under different scan speeds was investigated. The axial motion of the phantom was emulated by moving the transducer axially; hence, the transducer in this experiment was moved in two dimensions. A kernel around the focus with a size of $4\lambda \times 8\lambda$ was used to estimate the velocity. Effects of different scan speeds for axial velocity estimations of 0 and 10 mm/s are shown in Fig. 2.10(a), where the dashed and solid lines correspond to the 1-D and the 2-D autocorrelators, respectively. As a performance index, Fig. 2.10(b) shows the corresponding standard deviation estimate of the Doppler spectrum for the axial velocities of 0 mm/s (solid line) and 10 mm/s (dashed line). The dotted line in Fig. 2.10(b) represents the linear fit of the estimated standard deviation when a larger kernel ($16\lambda \times 20\lambda$) is used. In both figures, 30 realizations were used to obtain the statistical results. It can be seen that the velocity estimation errors for both 1-D and 2-D autocorrelators generally increase with the transducer scan speed. Due to the limited observation window, the proportionality between the estimate variance and the scan speed does not hold strictly, as explained earlier. In general, the 2-D autocorrelator outperforms the 1-D autocorrelator in terms

of the estimate variance. Besides, although the Doppler bandwidth is irrelevant to the axial velocity component, the estimate variance for 10 mm/s is evidently greater than that for 0 mm/s when the scan speed is below 15 mm/s. This is mainly attributable to the depth of field of the transducer used here not being large enough (the depth of field is $2f_{\text{num}}{}^2\lambda = 8\lambda$ in this case) and lacking uniformity, resulting in spectral fluctuation.

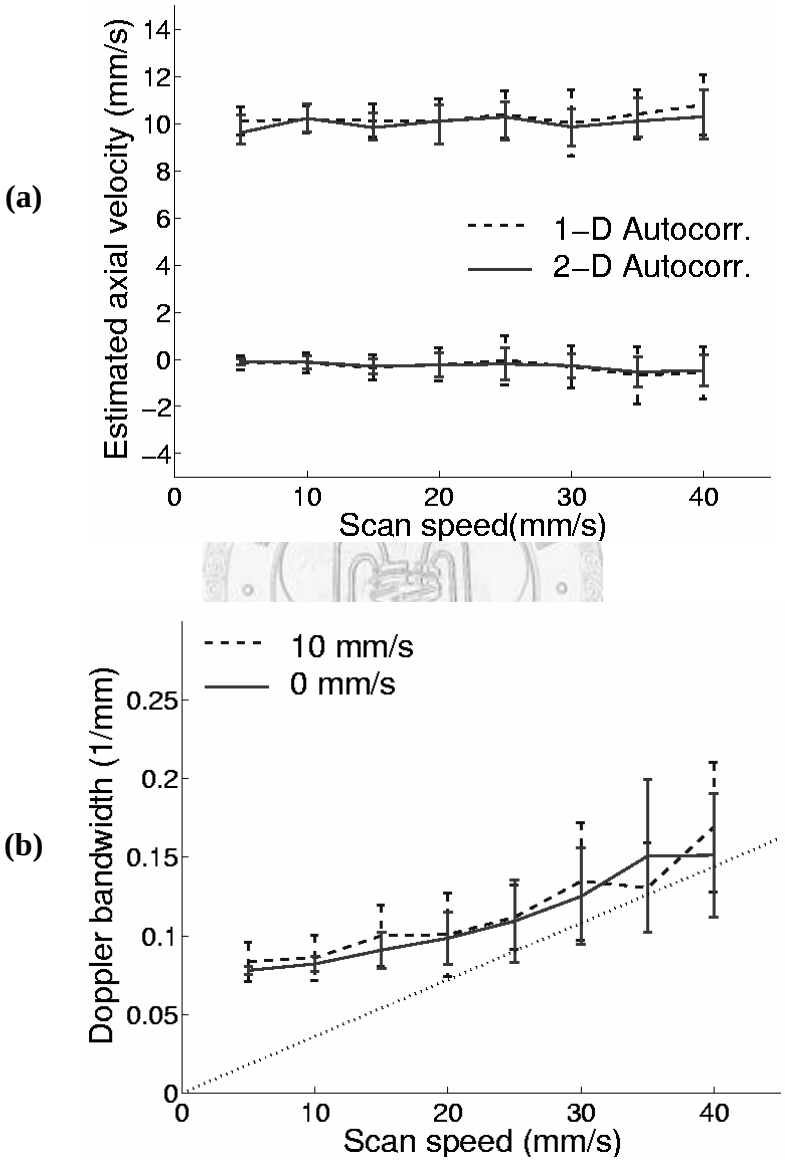

Fig. 2.10. (a) Effects of the scan speed on the 1-D (dashed lines) and 2-D (solid lines) autocorrelation-based axial velocity estimators. Axial velocities of 0 and 10 mm/s were investigated. (b) The corresponding standard deviation estimate of the Doppler spectrum as a function of the scan speed for axial velocities of 0 mm/s (dashed line) and 10 mm/s (solid line). The dotted line in (b) is the best linear fit of the esimates using a $16\lambda \times 20\lambda$ kernel. In each figure, error bars represent ± one standard deviation.

2.4 Concluding Remarks

This chapter investigated how continuously scanning the transducer affected the estimation of flow velocity in high-frequency ultrasound. Specifically, a *k*-space approach was employed to analyze 2-D motion with an arbitrary Doppler angle. Based on this *k*-space motion modeling, the temporal spectral contents of the swept- and step-scan methods were compared. The experimental results demonstrated that with the swept-scan technique, the Doppler bandwidth is approximately proportional to the relative lateral velocity between the transducer and the moving object when the kernel is large. Therefore, conventional lateral velocity estimation based on the proportionality between the Doppler bandwidth and the lateral velocity must be corrected. For instance, if the scan speed is 20 mm/s and a target moves laterally at 10 mm/s in the direction opposite to the scanning, the lateral velocity estimate for this target without considering the swept-scan effect is 30 mm/s.

We also examined the performance of the vector velocity estimation method (i.e., Doppler-based axial velocity estimator plus spectral-broadening-based lateral velocity estimator) in swept scanning. The results indicated that the performance indices related to flow velocity estimation, such as velocity resolution, estimate variance, and maximum/minimum detectable velocity, are compromised under different system settings. We summarize these results as follows. Increasing the scan speed improves the frame rate and the maximum detectable lateral velocity in the scanning direction; however, it limits the velocity resolution, the minimum detectable velocity, and the maximum detectable angle. Decreasing the f-number improves the lateral velocity resolution and the spatial resolution, but it increases the estimate variance and limits the minimum detectable velocity and the maximum detectable angle.

The experimental results also showed that the accuracy of spectral bandwidth estimation and the autocorrelation-based axial velocity estimators decreases as the scan speed increases. Due to the limited kernel size, the Doppler bandwidth estimation did not increase strictly proportionally with the relative lateral velocity. Thus, a large kernel size is required for accurate velocity estimation. Finally, the analyses performed did not consider flow velocity gradients, which may broaden the spectrum and degrade the performance of the spectral-broadening-based lateral velocity estimator [40], [41]. To address these problems, an efficient velocity estimator to reduce the estimation errors caused by the use of swept scanning and the presence of velocity gradients will be presented in Chapter 3.

Chapter 3 *K*-space Vector Velocity Estimator in Swept-scan

The conventional Doppler-based velocity estimation method limits its ability to detect the axial velocity component. Several techniques to quantify the non-axial velocity component are proposed, as mentioned in Section 1.4. Among them, the spectral-broadening-based velocity estimation method is particularly suited to a single-element transducer swept-scan system. However, as shown in Chapter 2, this technique includes a velocity bias proportional to the scan speed if the swept-scan effect is ignored. Furthermore, the spectral bandwidth increases with the scan speed, which makes the lateral velocity estimation with this technique in a swept scan more erroneous than in a step scan.

In order to correct the velocity estimation bias and reduce the estimation variance caused by the swept scan, an efficient vector velocity estimator is proposed based on the *k*-space approach described in Chapter 2. In the proposed method (referred to as the *k*-space vector velocity estimator), several vector velocity estimates corresponding to different axial spatial frequencies are averaged. Both simulations and constant flow phantom experiments were performed to demonstrate the validity of the proposed vector velocity estimator.

3.1 Theory

The *k*-space modeling technique described in (2.8) indicates that the lateral spatial spectral shift and bandwidth are related to the axial and lateral velocities, respectively. Therefore, the velocity vector can be obtained by combining the estimates from the mean frequency and the bandwidth of each lateral spatial spectrum. Accordingly, a procedure for estimating the velocity vector is proposed below. First, a kernel in an image is selected, which is then windowed (e.g., using a Hanning function) prior to 2-D Fourier transformation. Both the mean frequency and the bandwidth are estimated for each lateral spatial spectrum. To reduce the estimation error, the velocity estimate for each lateral spatial spectrum is further averaged across different axial spatial frequencies.

The mean frequency $\overline{f_x}$ of a lateral spatial spectrum at a specific f_z is calculated by

$$\overline{f_x(f_z)} = \frac{\int f_x \left|P'_{\mathrm{SW}}(f_x, f_z)\right|^2 \mathrm{d}f_x}{\int \left|P'_{\mathrm{SW}}(f_x, f_z)\right|^2 \mathrm{d}f_x}, \tag{3.1}$$

where $\left|P'_{\mathrm{SW}}(f_x, f_z)\right|^2$ is the 2-D power spectral density of the selected kernel. Note that the above equation is similar to the mean Doppler frequency estimation in conventional autocorrelation-based axial velocity estimation [40]. According to (2.8), the averaged axial velocity estimate ($\overline{u_{\mathrm{obj}} \cos\theta}$) is obtained by combining a total of M estimates corresponding to M different axial spatial frequencies (f_{zi}), i.e.,

$$\overline{u_{\mathrm{obj}} \cos\theta} = -\frac{1}{M} \sum_{i=1}^{M} \frac{\overline{f_x(f_{zi})}}{f_{zi}} u_{\mathrm{scan}}. \tag{3.2}$$

The bandwidth of the lateral spatial spectrum $bw_k(f_z)$ in (2.9) is defined as the difference between $\overline{f_x(f_z)}$ and the maximum lateral spatial frequency. The main advantage of this definition over other criteria, such as the standard deviation, is that estimating the maximum frequency is relatively insensitive to velocity gradients [54]. Another potential advantage is that the maximum frequency estimation is less affected by the wall filter used. Thus, the averaged lateral velocity estimate ($\overline{u_{\mathrm{obj}} \sin\theta}$) is given by

$$\overline{u_{\mathrm{obj}} \sin\theta} = \frac{1}{M} \sum_{i=1}^{M} \left(1 - \frac{f_{\mathrm{num}} bw_k(f_{zi})}{f_{zi}}\right) u_{\mathrm{scan}}. \tag{3.3}$$

Note that the above equation is derived based on $u_{\mathrm{rel}} \geq 0$ or $u_{\mathrm{scan}} \geq u_{\mathrm{obj}} \sin\theta$. Since $\pm u_{\mathrm{rel}}$ yield the same lateral spatial bandwidth, aliasing occurs when the lateral velocity component in the scanning direction is larger than the scan speed. That is, the lateral velocities $u_{\mathrm{scan}}(1 \pm s)$ in the scanning direction, where $s \geq 0$, cannot be distinguished.

The Doppler angle estimate $\hat{\theta}$ is readily found by combining (3.2) and (3.3), i.e.,

$$\hat{\theta} = \tan^{-1}\left(\frac{\overline{u_{\text{obj}} \sin\theta}}{\overline{u_{\text{obj}} \cos\theta}}\right). \tag{3.4}$$

Since the full 2-D spectrum is used, the *k*-space vector velocity estimator described here can be viewed as a wideband technique, in contrast to conventional narrowband methods such as the 1-D-autocorrelation-based [40] and the FFT-based vector velocity estimators [41], [42] which use only the center RF frequency (or equivalently, the center axial spatial frequency in our case). In the following sections, the conventional narrowband velocity estimator is referred to as the 1-D velocity estimator to distinguish it from the *k*-space velocity estimator.

3.2 Simulation Results

3.2.1 Kernel Size

Due to the finite observation window, the size of the kernel used to evaluate the flow velocity affects the accuracy of the *k*-space velocity estimator, in particular the bandwidth estimation more than the mean frequency estimation. In general, it is desirable to use a kernel that is large enough to incorporate the entire PSF. Since the PSF broadens with decreasing u_{rel}, the required lateral kernel size is thus determined by the maximum detectable lateral velocity component in the scanning direction. On the other hand, the required axial kernel size is determined by the maximum detectable axial velocity component. Based on the PSF described in (2.7), the required kernel size is derived theoretically below. To avoid improper truncation, the lateral kernel size should be greater than the –6-dB effective beamwidth w_{eff}. That is,

$$(N_{\text{L}} - 1)\Delta x \geq w_{\text{eff}} = \frac{\lambda f_{\text{num}}}{\left|1 - u_{\text{obj}} \sin\theta / u_{\text{scan}}\right|} = \frac{\lambda f_{\text{num}} u_{\text{scan}}}{\left|u_{\text{rel}}\right|}, \tag{3.5}$$

where N_{L} is the number of scan lines in the kernel. Note that w_{eff} is equal to λf_{num} for a stationary object [1]; moreover, w_{eff} increases as u_{rel} decreases. Once N_{L} is determined according to (3.5), the required axial kernel has to be larger than the axial shift caused by the axial velocity component. We therefore have

$$(N_{\mathrm{A}}-1)\Delta z \geq (N_{\mathrm{L}}-1)\frac{\left|u_{\mathrm{obj}}\cos\theta\right|}{u_{\mathrm{scan}}}\Delta x, \tag{3.6}$$

or equivalently,

$$\frac{(N_{\mathrm{A}}-1)\Delta z}{(N_{\mathrm{L}}-1)\Delta x} \geq \frac{\left|u_{\mathrm{obj}}\cos\theta\right|}{u_{\mathrm{scan}}}, \tag{3.7}$$

where Δz denotes the sampling interval along the axial direction and N_{A} is the required number of axial sampling points. (3.7) indicates that the ratio of the axial to lateral kernel sizes must be larger than the ratio of the axial velocity component to the scan speed. The lateral and axial kernel sizes can be determined from (3.5) and (3.6), respectively. For example, according to the parameters indicated in Table 2.1, in order to detect a target velocity of 30 mm/s with $\theta = 30°$, the required kernel size is at least 8λ (lateral)×10.4λ (axial). In practice, the kernel should be slightly larger than the predicted one due to the windowing function applied. Note that the above analysis of the kernel size is similar to that of the aspect ratio associated with conventional spectral-broadening-based vector velocity estimation methods [40].

The effects of kernel size on the lateral spatial bandwidth estimation were further studied by simulating a moving target. Doppler angles ranging from –90° to 40° with a step of 10° were investigated (see Fig. 2.1). A Hanning window was applied to the kernel prior to 2-D Fourier transformation. Fig. 3.1 shows the effects of kernel size on the –12-dB bandwidth for vector velocities of 30 mm/s (top panel) and 50 mm/s (bottom panel), where only the lateral spatial spectrum at the center axial spatial frequency was used for the bandwidth estimation. The horizontal axis is u_{rel}. In this case, no lateral velocity component is present when $u_{\mathrm{rel}} = 20\,\mathrm{mm/s}$. Ideally, the lateral spatial bandwidth is proportional to u_{rel} (see (2.9)), and Fig. 3.1 shows that the bandwidth is approximately proportional to u_{rel} as the kernel size increases. For smaller u_{rel}, however, such a relationship does not hold and the bandwidths become overestimated. As mentioned earlier, this is because the PSF expands laterally and hence becomes truncated. In this case, the bandwidth becomes dominated by the lateral kernel size. Fig. 3.1 suggests that an 8λ×10λ kernel is suitable for the vector velocity estimation, and is adopted in the sections below.

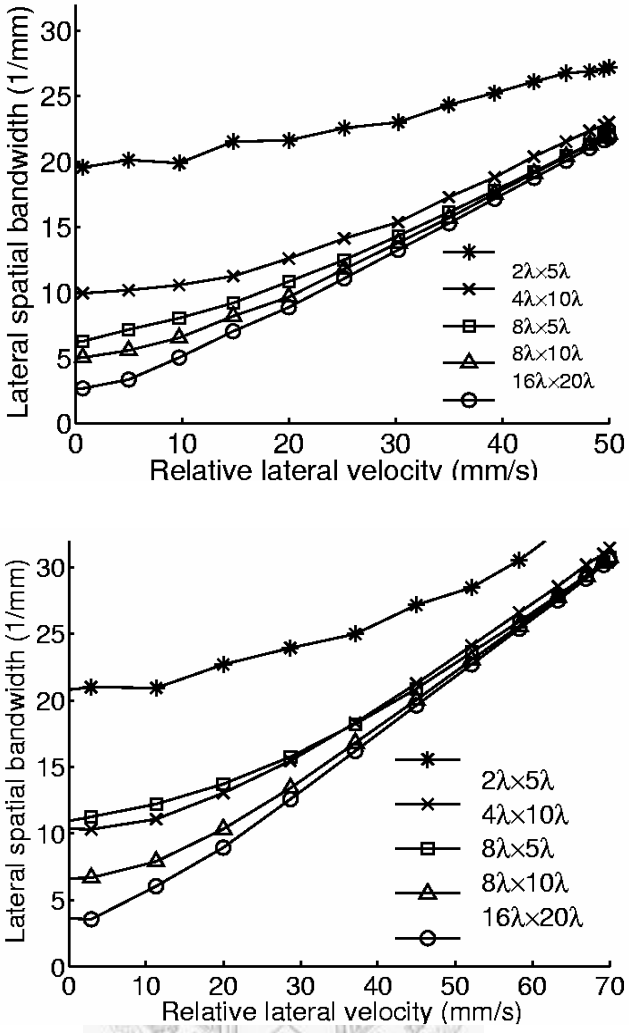

Fig. 3.1. Effects of kernel size on the –12-dB bandwidth for vector velocities of 30 mm/s (top panel) and 50 mm/s (bottom panel). The horizontal axis is u_{rel}.

3.2.2 Constant Flows

To verify the proposed *k*-space velocity estimator, a speckle-generating object moving at a constant velocity of 30 mm/s was simulated. Doppler angles from –90° to 40° with a step of 10° were investigated. The –12-dB threshold was used to determine the lateral spatial bandwidth, and the scaling factor γ in (3.3) was empirically set to 0.33. Eleven axial spatial frequencies (i.e., M =11) were used for averaging. Fig. 3.2 shows the estimated velocity components and Doppler angles using the *k*-space velocity estimator (solid lines). Fig. 3.2(a) shows the estimated u_{rel}, and Figs. 3.2(b) and (c) show the estimated axial velocity components and Doppler angles, respectively. As a comparison, the results for the 1-D velocity estimator are shown as dashed lines. The dotted lines represent the actual values. Note that a positive axial velocity represents movement away from the transducer. Also note that the axial

velocity estimates for the Doppler angles within 0~40° are similar to those within –40~0° and are not shown here for display convenience. In this figure, ten independent realizations were generated to produce the mean and standard deviation values.

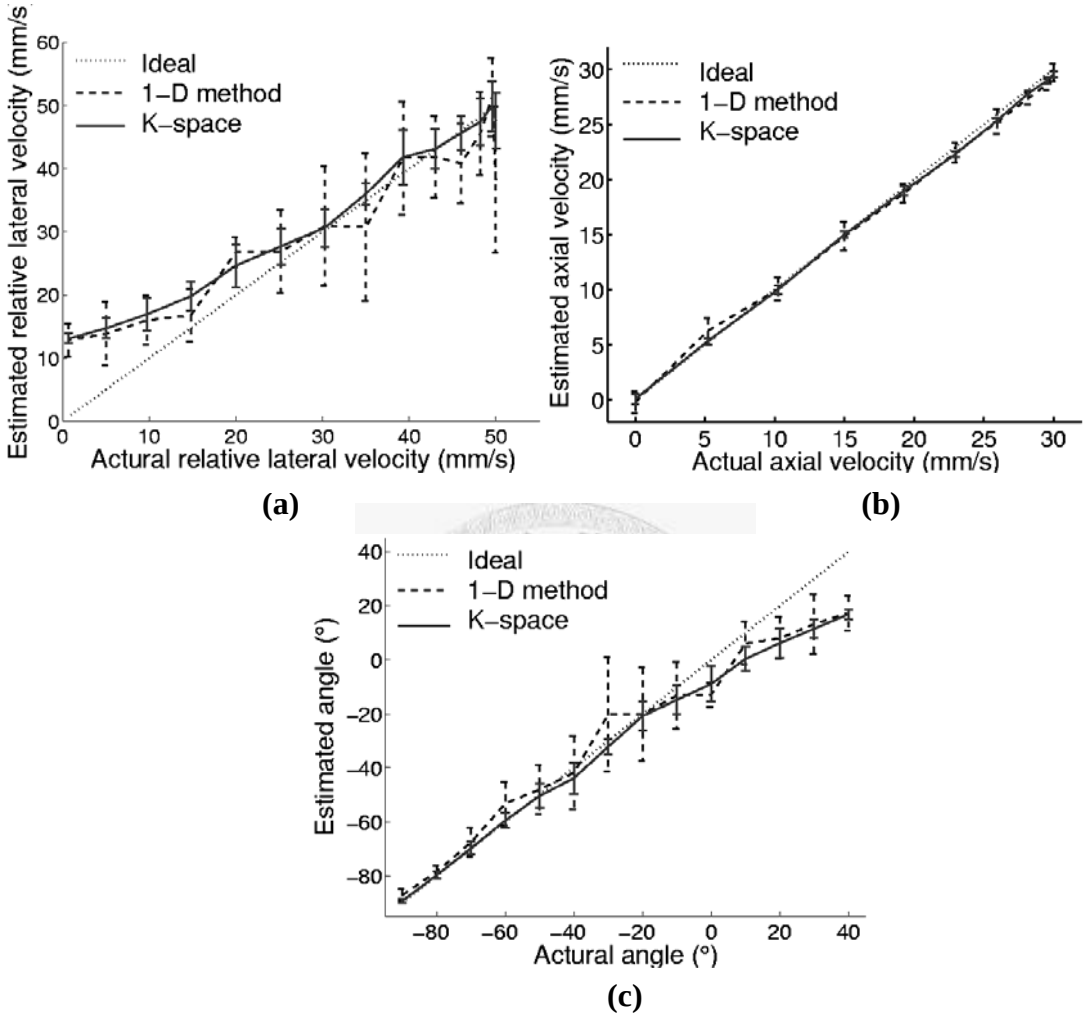

Fig. 3.2. Constant-flow simulation results. The *k*-space (solid lines) and 1-D (dashed lines) vector velocity estimators are compared. (a) Estimated u_{rel}. (b) Estimated axial velocity components. (c) Estimated Doppler angles. The dotted lines are the actual values. The error bars represent ± one standard deviation relative to the mean.

Compared Fig. 3.2(a) to Fig. 3.2(b), the axial velocity estimates are more accurate and robust than the lateral velocity estimates. The estimated lateral velocities in the direction opposite to the scanning direction (i.e., $u_{\text{rel}} > 20\,\text{mm/s}$) are in close agreement with the actual ones. The lateral velocities in the scanning direction, however, are overestimated due to the finite kernel size (as explained in Section 3.2.1). However, a smaller u_{rel} narrows the lateral spatial spectrum and consequently reduces the estimation variance, as evident in Fig. 3.2(a). Generally speaking, the

estimates of lateral velocities in the direction opposite to the scanning direction and the corresponding Doppler angles (i.e., $\theta = -90 \sim 0°$) are in good agreement with the actual values. Overall, the *k*-space estimator outperforms the 1-D estimator in terms of both the estimation bias and the standard deviation, demonstrating that averaging across axial spatial frequencies is effective in reducing the estimation error.

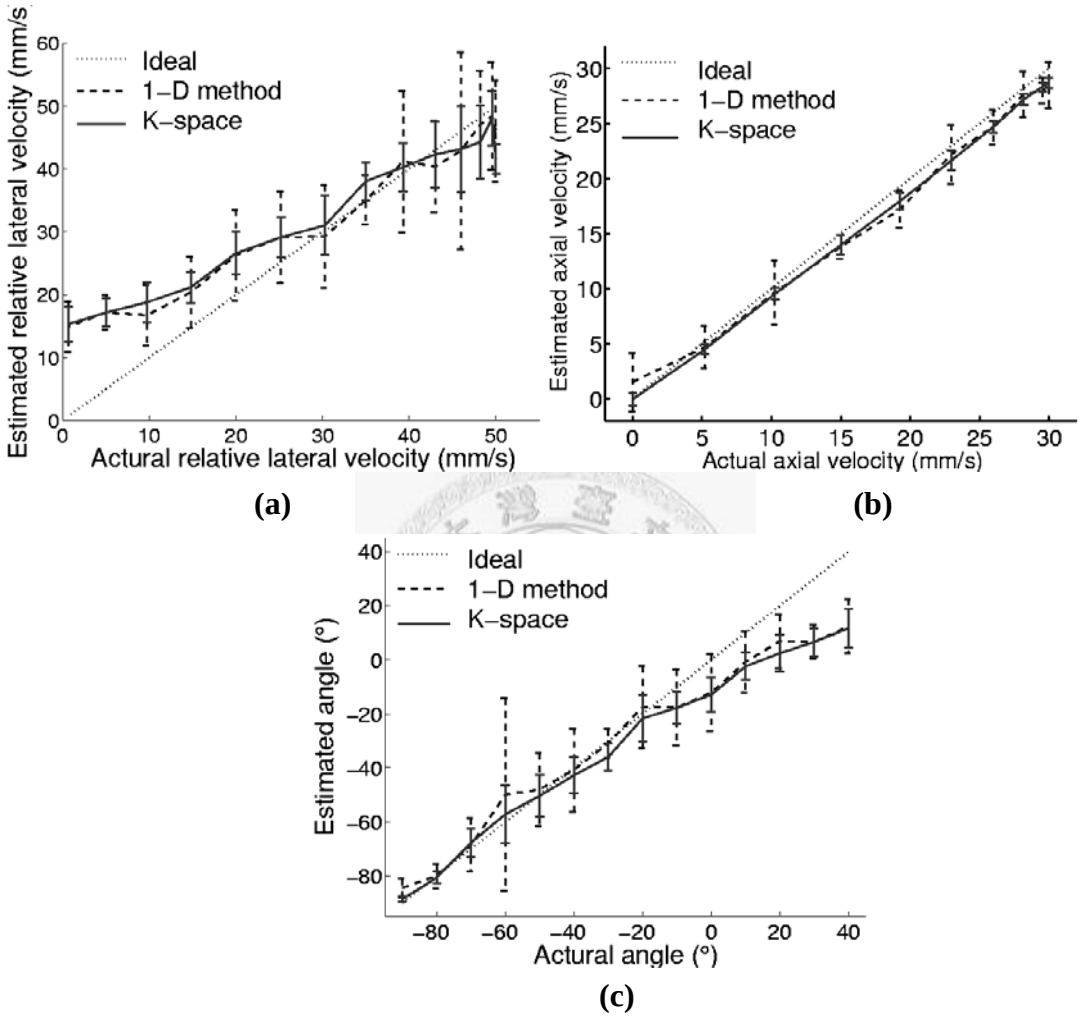

Fig. 3.3. Laminar-flow simulation results, shown in the same format as Fig. 3.2.

3.2.3 Spatial Velocity Gradients

The preceding simulations assumed constant flows within the selected kernel and did not include spatial velocity gradients. In practice, the presence of velocity gradients degrades the accuracy of the bandwidth estimation [40], [41]. To evaluate such effects on the proposed *k*-space estimator, a laminar flow $u(r)$ with a parabolic profile was simulated using

$$u(r) = (1 - \frac{r^2}{R^2})u_{\max}, \tag{3.8}$$

where R is the vessel radius, r is the radial distance relative to the vessel center, and $u_{\max}$ is the maximum flow velocity. The vessel was surrounded by stationary clutter, and the intensity ratio between the flow and clutter signals was set to unity. Parameter values of $R = 0.31\,\text{mm}$, $u_{\max} = 30\,\text{mm/s}$, and θ from –90° to 40° were used. The kernel size was 8λ×10λ, making its lateral size roughly equal to the vessel radius when $\theta = 0°$. Other simulation conditions were identical to those for the constant flows. To minimize the effects of velocity gradients, the peak frequency was estimated instead of the mean frequency [54]. The estimation results are shown in Fig. 3.3 using the same display format as in Fig. 3.2. The estimation errors are slightly higher for laminar flows than for constant flows. Note that in Fig. 3.3(b), since the kernel includes a large portion of the vessel, the axial velocities are underestimated relative to their corresponding maximum axial velocities. The *k*-space estimator is still better than the 1-D estimator, with the simulation results showing that applying the *k*-space estimator is feasible in the presence of velocity gradients.

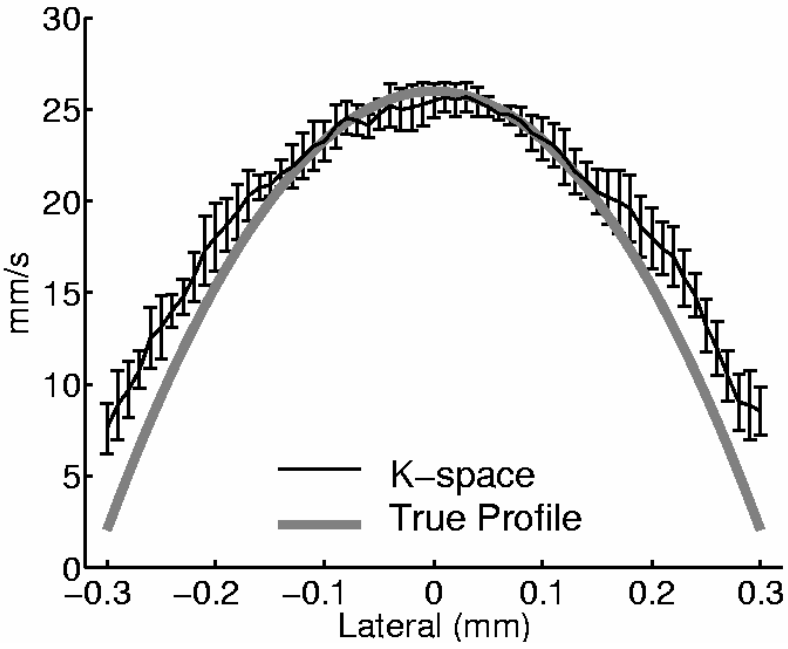

Fig. 3.4. Estimation of flow velocity profile using the *k*-space (thin solid line) estimator. The thick solid line is the actual profile. The Doppler angle is –30° and the kernel size is 2λ×5λ. The error bars represent ± one standard deviation relative to the mean.

The use of a large kernel improves the lateral velocity estimation because it is more susceptible to the observation window than the axial velocity estimation. If a vessel is smaller than the required kernel, the precise flow profile cannot be obtained. To account for this problem, a larger kernel is used firstly to determine the Doppler angle, from which a smaller kernel can be used to estimate the axial velocity

component and in turn, the velocity vector. This is demonstrated in Fig. 3.4, where a laminar flow with $\theta = -30°$ was investigated using the *k*-space estimator (thin solid line). A 2λ×5λ kernel was used to estimate the axial velocity component. Ten realizations were generated. Since the kernel contains larger velocity gradients for smaller velocities than those for larger velocities, so the estimated profile is slightly broadened. Also note that the estimation variance is larger than that shown in Fig. 3.3(b) because a smaller kernel was used in this case. It is evident that this two-step vector velocity estimation method allows accurate estimation of the velocity profile.

3.3 Experimental Results–Constant Flows

The principle of the *k*-space vector velocity estimator is derived assuming a constant velocity. Thus, a constant-flow experiment was designed to meet this requirement. To emulate a 2-D constant flow, a speckle phantom was placed in a water tank and interrogated by a tilted, scanned transducer. Fig. 3.5 explains how scanning a tilted transducer laterally is equivalent to moving a phantom in two dimensions. When the transducer is moved from right to left with a tilt angle of ψ, the equivalent axial velocity component is $u_{\text{scan}} \cos\psi$ toward the transducer, and the equivalent relative lateral velocity between the transducer and the phantom is $u_{\text{scan}} \sin\psi$. In this way, 2-D constant flows were emulated by varying the scan speed and the tilt angle. Note that the tilt angle of the transducer rather than the Doppler angle was estimated.

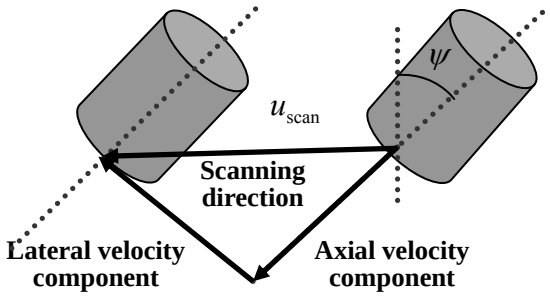

Fig. 3.5. The effect of scanning a tilted transducer.

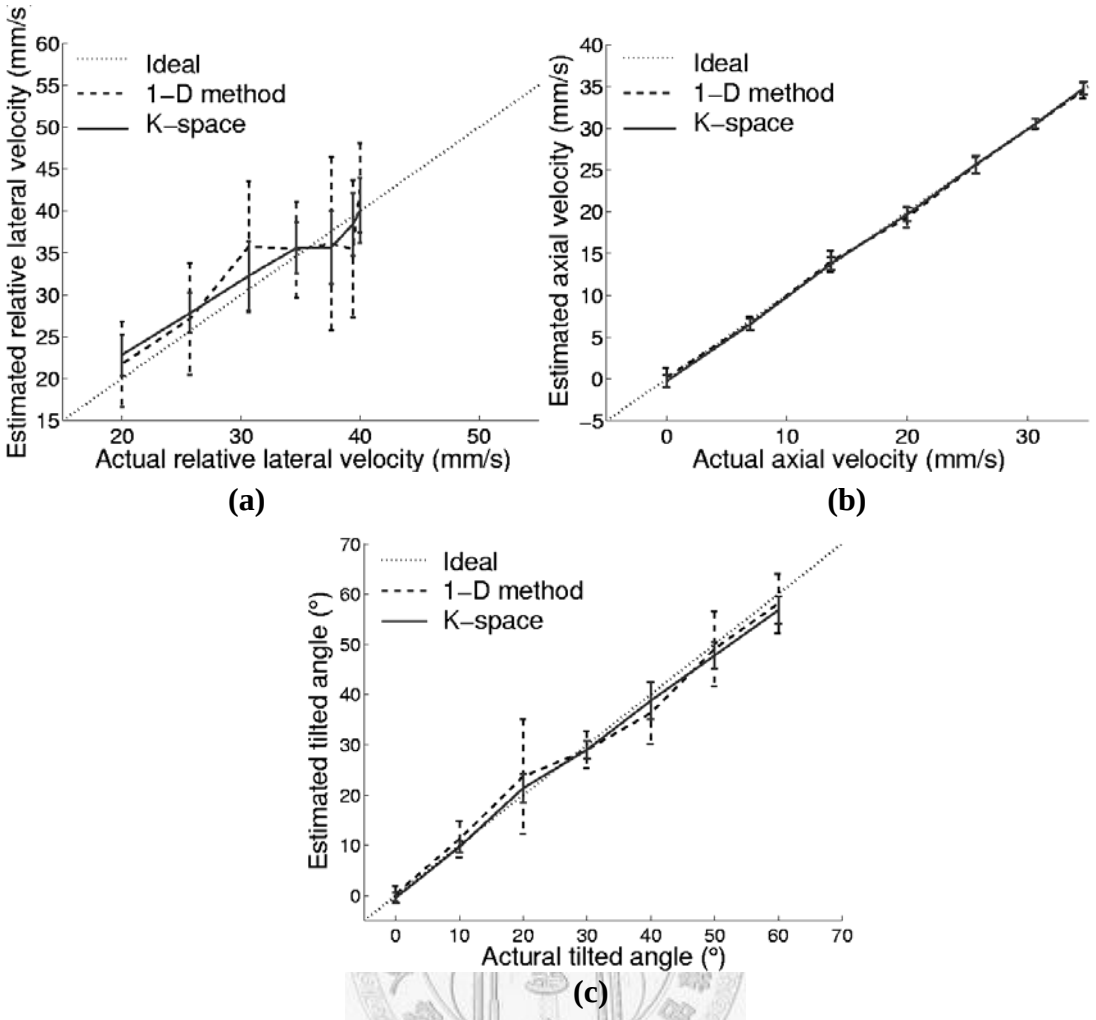

Fig. 3.6. Constant-flow experimental results obtained by scanning a tilted transducer at 40 mm/s. (a) Estimated u_{rel}. (b) Estimated axial velocities. (c) Estimated tilt angles. The solid and dashed lines correspond to the *k*-space and 1-D vector velocity estimators, respectively. The dotted lines are the actual values. The error bars represent ± one standard deviation relative to the mean.

Scan speeds of 40 and 50 mm/s were investigated. For each scan speed, the phantom data were collected at tilt angles from 0° to 60° in increments of 10°. An 8λ×10λ kernel was selected around the focus. A –12-dB bandwidth threshold was used, γ was set to 0.33, and 11 axial spatial frequencies were employed in the *k*-space estimator. Figs. 3.6 and 3.7 show the estimation results when the transducer was scanned at 40 and 50 mm/s, respectively. Each figure includes estimations of the relative lateral velocities (Figs. 3.6(a) and 3.7(a)), the axial velocities (Figs. 3.6(b) and 3.7(b)), and the corresponding tilt angles (Figs. 3.6(c) and 3.7(c)). The solid and dashed lines are the results for the *k*-space and 1-D estimators, respectively, and the dotted lines are the actual values. Ten independent experiments were performed to produce mean and standard deviation values. Consistent with the simulation results, the axial velocity estimation is more accurate than the relative lateral velocity

estimation. Furthermore, smaller relative lateral velocities are overestimated. The estimation errors in the experimental results are, however, larger than those in the simulations, especially for the 1-D estimator. This is because the presence of large spectral fluctuations in the experimental data makes it difficult to estimate the bandwidth correctly. This is partly attributable to the depth of field of the transducer being too small and lacking uniformity. As a result, when only the axial velocity component is present, the echoes of two adjacent scan lines are no longer the delayed and scaled versions of each other, leading to additional spectral variation. Another reason is that during data acquisition, the motor speed is not constant, which also results in spectral fluctuation. Although the two above factors affect the accuracy of the velocity estimation, the *k*-space estimator is still more robust and is more consistent with the actual values than the 1-D estimator. Note that unlike the Doppler angle estimation in the simulations, underestimation occurs at larger tilt angles where the relative lateral velocities are overestimated.

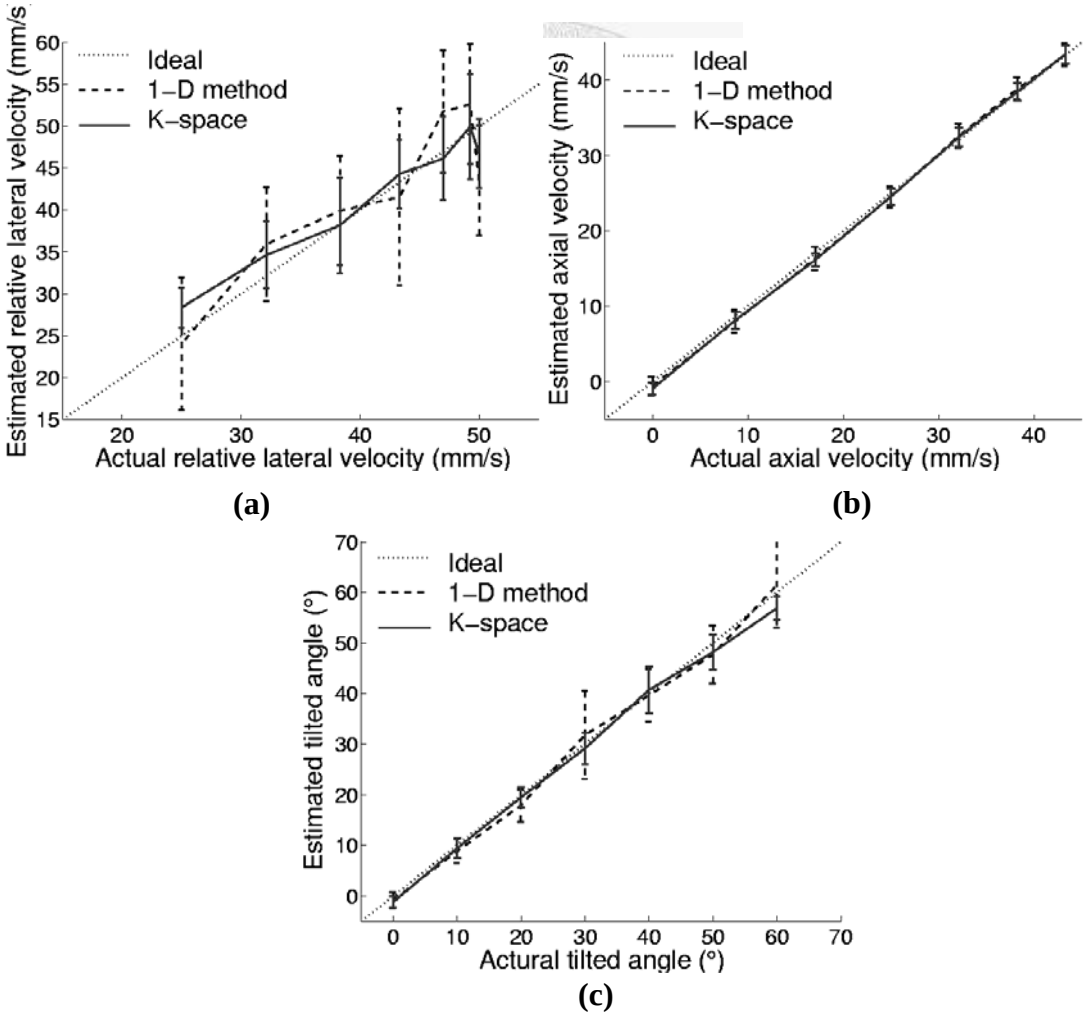

Fig. 3.7. Constant-flow experimental results obtained by scanning a tilted transducer at 50 mm/s, shown in the same format as Fig. 3.6.

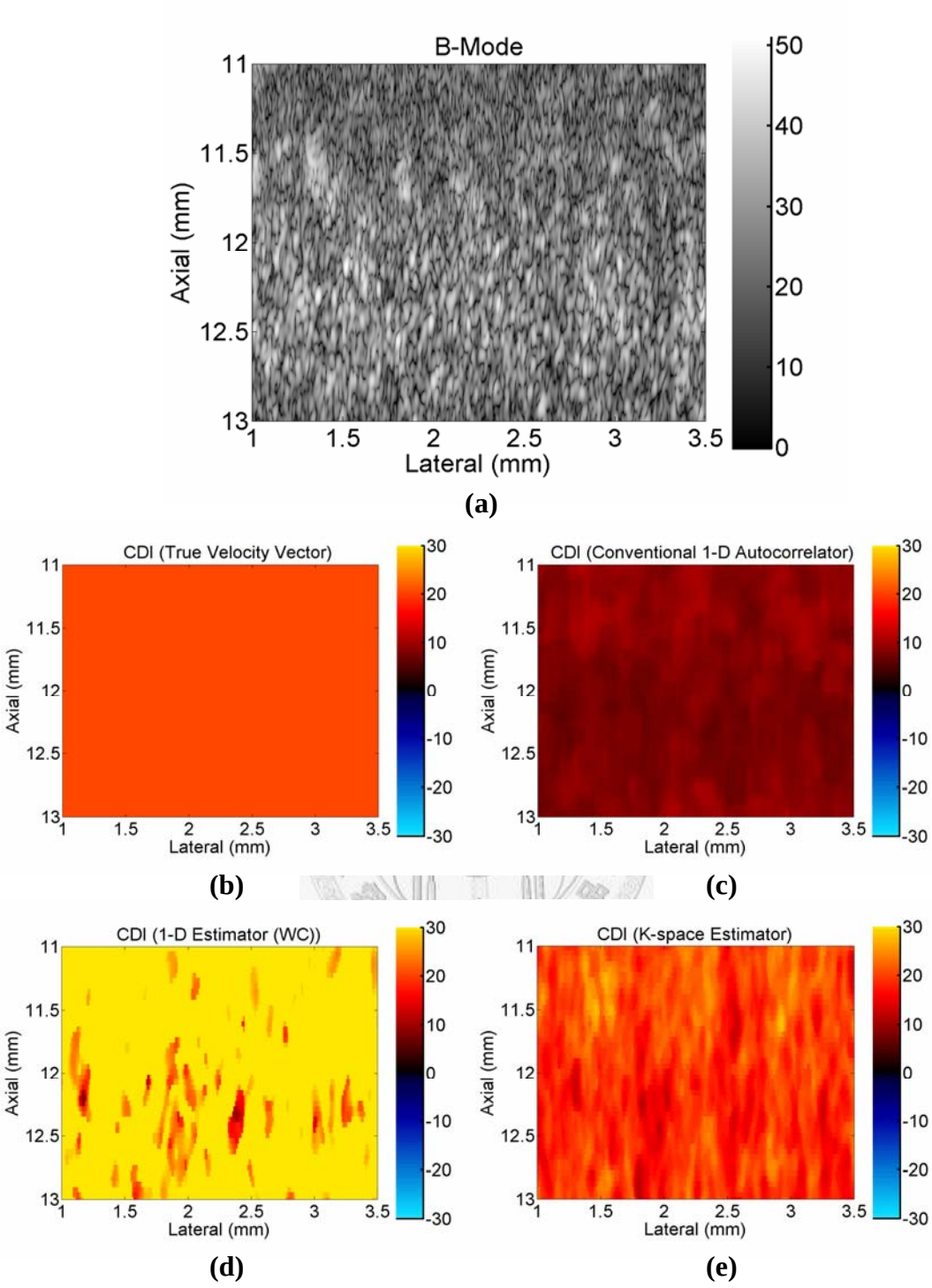

Fig. 3.8. B-mode (panel (a)) and color Doppler images (panels (b)–(e)) of the constant flow phantom. The actual axial and lateral velocities are 6.9 (toward the transducer) and 19.4 mm/s (in the opposite of the scanning direction), respectively. Panel (b) shows the true velocity vector (20.6 mm/s). Panel (c) corresponds to the conventional 1-D autocorrelator. Panel (d) corresponds to the 1-D estimator without considering the swept-scan effect; panel (e) corresponds to the *k*-space estimator.

The advantage of the *k*-space estimator is further demonstrated in Fig. 3.8, in which color Doppler images (panels (b)–(e)) with different velocity estimation methods were compared at a scan speed of 40 mm/s and a tilt angle of 10°. In this case, the axial velocity was 6.9 mm/s toward the transducer, whereas the emulated lateral velocity of the phantom was 19.4 mm/s assuming the transducer speed was 20 mm/s. This yields a velocity vector of 20.6 mm/s. Panel (a) shows the B-mode image. Panel (b) shows the true velocity vector result. Panel (c) shows the result of the conventional 1-D autocorrelation-based axial velocity estimation method [3]. Panel (d) corresponds to the 1-D estimator without considering the swept-scan effect; panel (e) corresponds to the *k*-space estimator. All color Doppler images were post-processed by employing proper thresholding and the median filter. As shown in Fig. 3.8, the conventional 1-D autocorrelation method could only detect the axial velocity component, and the 1-D estimator ignoring the swept-scan effect produced a large bias. Note that the velocity shown in this figure was limited within ±30 mm/s, and the actual estimation results for the 1-D estimator were larger than those displayed. The *k*-space estimator provided the accurate velocity vector information though the estimation variance was slightly larger than that in panel (c).

3.4 Discussion and Concluding Remarks

In this chapter, based on the *k*-space modeling technique introduced in Chapter 2, we proposed an efficient vector velocity estimator that combines the velocity estimates within several axial spatial frequencies. The experimental results demonstrated that the *k*-space velocity estimator can correct angle estimation bias caused by the swept scanning, and provide more accurate vector velocity estimation than conventional narrowband velocity estimation methods.

As shown in Section 3.2.1, the lateral and axial kernel sizes are chosen according to the maximum detectable lateral (in the scanning direction) and axial velocity components, respectively. Although the determination of the kernel size in a swept scan is based on the PSF, it is conceptually identical to the number of firings and the range gate in a step scan. In the later case, the number of firings has to be large enough so that the observation time is longer than the lateral transit time [40], whereas the range gate length is determined to assure that the Doppler bandwidth is governed by the lateral transit time rather than the gate length [40]. Note that for the conventional spectral-broadening-based methods in a step scan, due to its narrowband

characteristics, the pulse length that determines the axial length of the sample volume is required to be sufficiently long to provide accurate velocity estimation at the center frequency. In comparison, since the k-space velocity estimator is a wideband technique, the pulse length has less effects on the velocity estimation.

Simulation and experimental results for the proposed *k*-space velocity estimator showed that axial velocity estimation is more robust than lateral velocity estimation. One of the main reasons is that the lateral velocity resolution is lower than the axial velocity resolution by a factor of $f_{\text{num}}/\gamma = 6$ (see Section 2.2.1). Other reasons include the mean frequency estimation being less sensitive to spectral variation and, most importantly, less influenced by the observation window. As indicated in Figs. 3.2(a) and 3.3(a), an $8\lambda \times 10\lambda$ kernel is sufficient for accurate lateral velocity estimation in the direction opposite to the scanning direction. However, such a kernel is too small for lateral velocities in the scanning direction even though the estimation variance in this case is greatly reduced. Note that the aforementioned situation is unrelated to the scan speed. Slowing down the transducer simply improves the lateral velocity resolution (Eq. (2.13)) and is irrelevant to the overestimation of the lateral velocity in the scanning direction. This problem can be solved by increasing the kernel size or detecting the lateral velocity in the next frame. However, these two methods cannot be applied to flows exhibiting spatial or temporal variations. An alternative method is to predict the truncated region outside the selected kernel using autoregressive modeling [41]. In this case, since the estimation variance is not large, 1-D rather than 2-D autoregressive prediction is sufficient to obtain reliable estimates.

In the experiment, the transducer was tilted and scanned laterally to emulate 2-D motion of the speckle phantom. The results indicated that the use of a tilted transducer for flow measurements using the swept-scan technique might result in poor estimation of the velocity vector even if the tilt angle is small. For example, for a scan speed of 20 mm/s and a tilt angle of 10°, there is a difference of 3.5 mm/s between the actual and estimated axial velocities, which is larger than the axial velocity resolution of 1.25 mm/s. Hence, especially for slow flows, accurate velocity measurement has to take this effect into account. Other experimental factors affecting the accuracy of the vector velocity estimation include the limited depth of field and the instability of the scanning motor, as discussed in Section 3.3. Both factors lead to spectral variation and degrade the velocity estimation especially when the spectral bandwidth is small.

Finally, although the analyses and the estimation results presented in this chapter were performed at the focal range of the transducer, they are also valid in the non-focal region. In this case, an additional quadratic phase curvature – equal to the

difference between the phase curvature at the focal range and the range of interest – has to be imposed on the aperture function in (2.6). Thus, if the scan speed is much smaller than the sound velocity, the lateral spatial spectrum at the non-focal range is still an even function and the axial velocity estimation is not affected. For lateral velocity estimation, the proportionality between the relative lateral velocity and the lateral spatial spectral bandwidth still holds outside the focus. However, the scaling factor γ should be set dynamically along the range. Therefore, a lookup table for γ is required to perform vector velocity estimation on the entire image.

Chapter 4 Experimental Results

In this chapter, the efficacy of the proposed *k*-space vector velocity estimator in a swept-scan system presented in Chapter 3 was further evaluated with both *in vitro* and *in vivo* experiments. In both experiments, the kernel size used for velocity estimation was 8λ×10λ. The bandwidth threshold was –12 dB and γ was 0.33. For all velocity results shown here, a negative lateral velocity represents movement away from the scanning direction whereas a negative axial velocity represents movement toward the transducer.

4.1 *In Vitro* Results

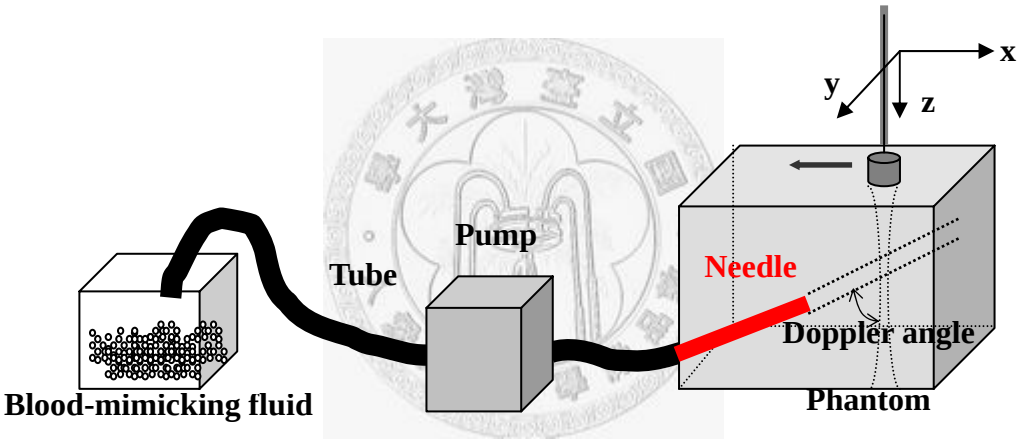

Fig. 4.1. The *in vitro* flow experimental setup.

In vitro experiments with blood-mimicking fluid were conducted using the setup illustrated in Fig. 4.1. A needle with a diameter of 1.5 mm connected to a tube was embedded inside a speckle phantom as a flow pathway. A pump (Cole-Palmer, Vernon Hills, IL) was used to produce flow velocities between 15 and 30 mm/s. As indicated in Fig. 4.1, the transducer was scanned from right to left at 20 mm/s, and the flow direction was toward it. Six Doppler angles of 29°, 45.2°, 59.2°, 70.4°, 82.6°, and 90° were measured. Only the flow data acquired around the focus were used to estimate the Doppler angle. At each angle, five different realizations were generated. As an example, a swept-scanned image containing a flow with a Doppler angle of 59.2° is displayed with a 40-dB dynamic range in Fig. 4.2(a). Fig. 4.2(b) shows the *k*-space representation of the kernel indicated by a white box in Fig. 4.2(a). Eleven estimates of the axial velocity component (dashed line) and the lateral velocity component

(solid line) corresponding to 11 different axial spatial frequencies are shown in Fig. 4.2(c), where an axial spatial frequency index of six represents the center axial spatial frequency.

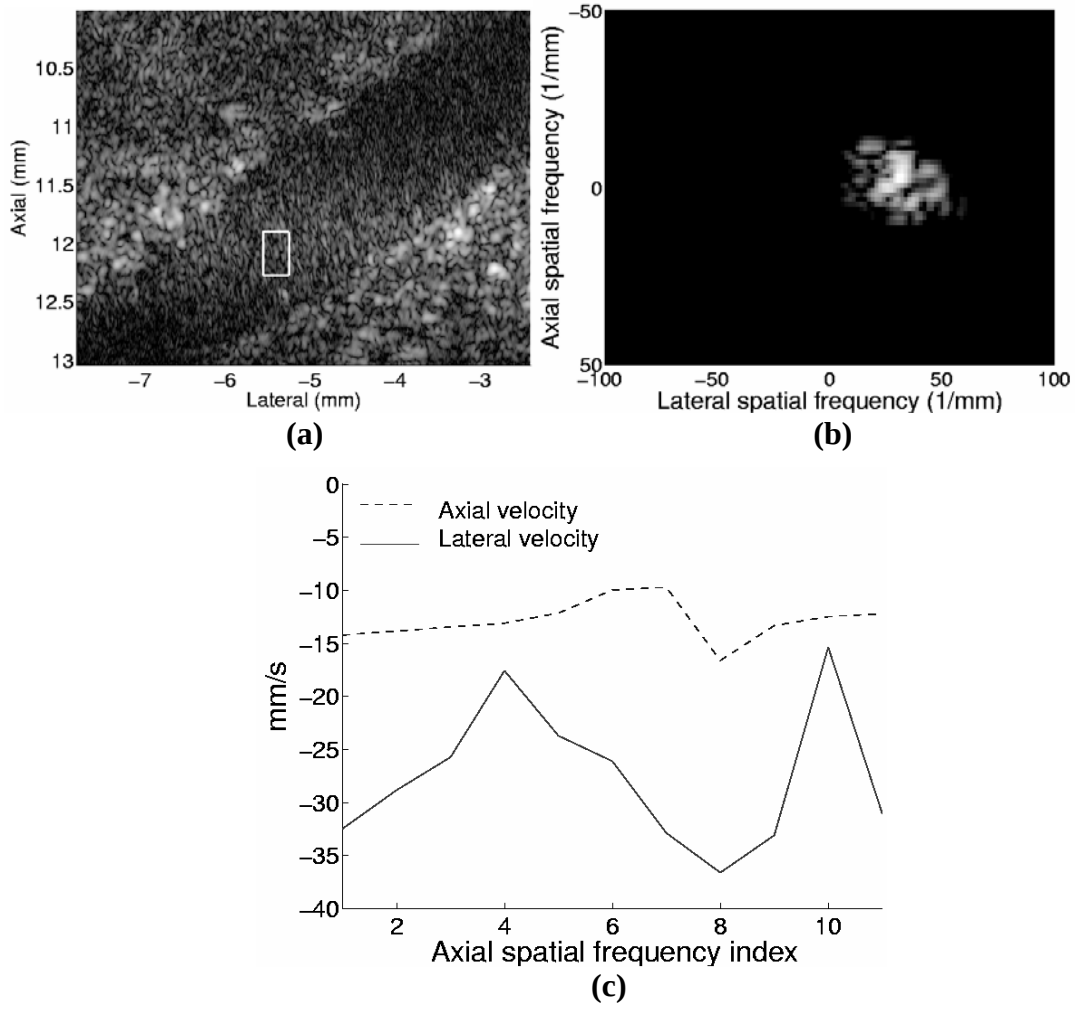

Fig. 4.2. *In vitro* flow experimental results. (a) A 40-dB swept-scanned image containing a flow at an angle of 59.2°. The white box indicates the selected kernel. (b) The *k*-space representation of the selected kernel displayed with a 20-dB dynamic range. (c) The estimates of the axial (dashed line) and lateral (solid line) velocity components as functions of f_z.

Fig. 4.3 shows the estimated Doppler angles using the 1-D estimator (dashed line) and the *k*-space estimator (heavy solid line). As a comparison, the result for the conventional spectral-broadening-based method (i.e., the 1-D estimator without considering the swept-scan effect) is shown as a light solid line. The corresponding mean and standard deviation values are listed in Table 4.1. The *k*-space estimator had an average angle estimation bias of 2.6° and standard deviations from 2.2° to 8.2°,

whereas the 1-D estimator had an average angle estimation bias of 3.4° and standard deviations from 5.8° to 13.3°. When the swept-scan effect was ignored, the average angle estimation bias became 15° and the standard deviations were from 2.7° to 6.6°. These experimental results demonstrate that a wide range of Doppler angles can be correctly estimated using the *k*-space estimator.

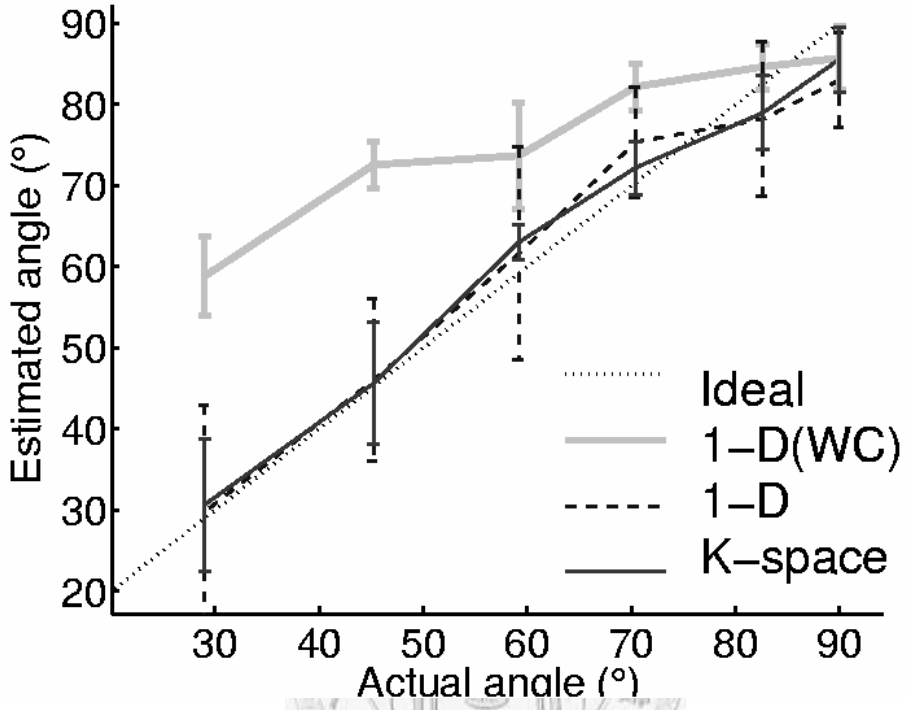

Fig. 4.3. Flow experimental results. Doppler angles are estimated using the 1-D estimator (dashed line) and the *k*-space estimator (heavy solid line). As a comparison, the light solid line represents the 1-D estimator ignoring the swept-scan effect (denoted as 1-D (WC)). The dotted line shows the actual Doppler angles.

Table 4.1. Doppler angle estimations on a flow phantom using the 1-D estimator, the *k*-space estimator, and the 1-D estimator ignoring the swept-scan effect (mean ± one standard deviation)

Doppler angle (°)	**1-D estimator (without correction)**	**1-D estimator**	***k*-space estimator**
29.0	58.7 ± 4.9	29.8 ± 13.3	30.7 ± 8.2
45.2	72.6 ± 2.9	46.0 ± 10.0	45.6 ± 7.5
59.2	73.7 ± 6.6	61.6 ± 13.1	63.0 ± 2.2
70.4	82.2 ± 2.7	75.4 ± 6.7	72.2 ± 3.3
82.6	84.7 ± 2.8	78.2 ± 9.5	79.0 ± 4.6
90.0	85.8 ± 3.9	83.0 ± 5.8	85.6 ± 4.0

4.2 *In Vivo* Results

To test the performance of the *k*-space velocity estimator, *in vivo* flow measurements on mouse tails were performed. The mice were properly anesthetized and a side of the tail containing a vein was scanned. The scan speed in this experiment was 10 mm/s (PRI = 100 μs and Δx = 1 μm). Fig. 4.4(a) shows one of the B-mode images over a 50-dB dynamic range, from which a vessel is clearly visible. As an initial investigation, the color Doppler image using the 1-D autocorrelator (see Section 1.1.1) with proper post processing is displayed in Fig. 4.4(b). Every pixel in this image was formed by using 16 successive scan lines and a 4λ range gate, and no angle correction was done (thus, only the axial velocity components were detected). In addition, a Chebyshev type II, 8th-order IIR high-pass filter was employed as a wall filter. This wall filter was applied to the whole data set before performing the velocity estimation. As indicated in Fig. 4.4(b), the axial velocity components in the vessel were around 10 mm/s. By consecutively scanning the same region, the vessel boundary was detected from the consecutive B-mode images and the measured Doppler angle was around 55°.

The velocities and angles were individually estimated for four different kernels indicated as four color boxes in Fig. 4.4(a). The white, blue and red boxes correspond to the flow regions with the increasing range, whereas the black box corresponds to the tissue. Different from the *in vitro* measurements, the vessel size in this case is smaller than the kernel size. To remove the clutter signals, we used a 2-D, IIR high-pass filter with the same cut-off lateral spatial frequency along the axial spatial frequency. The cut-off frequency was chosen empirically according to spectra of stationary tissues. The ability of this 2-D wall filter in clutter rejection is demonstrated in Fig. 4.5. Fig. 4.5(a) shows the original white color kernel (left) and its *k*-space representation (right). Fig. 4.5(b) shows the results after applying an 8th-order Chebyshev type II, 2-D IIR filter. It can be seen that the signals outside the vessel are almost suppressed. Fig. 4.5(c) shows the results of the rejected clutter signals. The signals with lower frequencies are still present in the vessel.

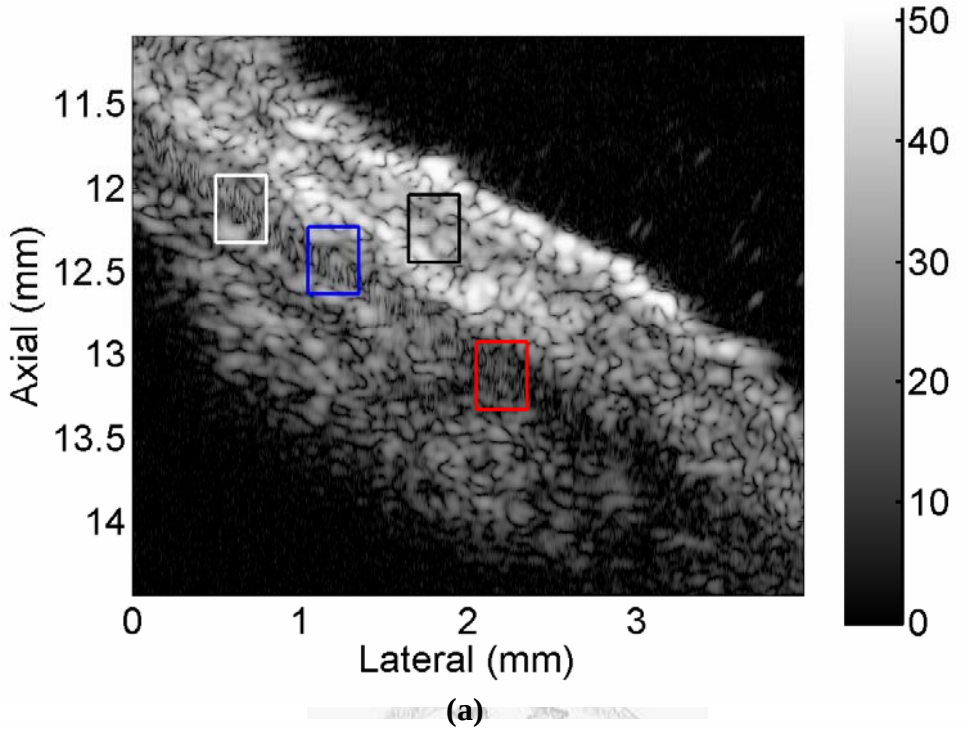

(a)

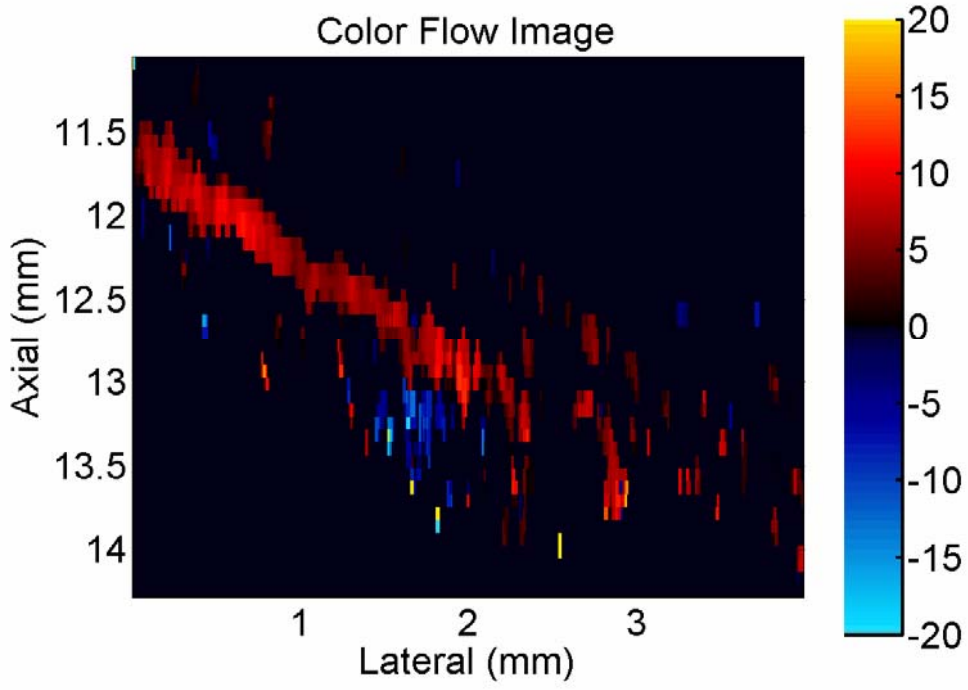

(b)

Fig. 4.4. An *in vivo* flow measurement in a mouse tail (Doppler angle ~ 55°). (a) B-mode image (displayed over a 50-dB dynamic range). (b) Color Doppler image (in units of mm/s) using the 1-D autocorrelator. Note that angle correction was not used in panel (b).

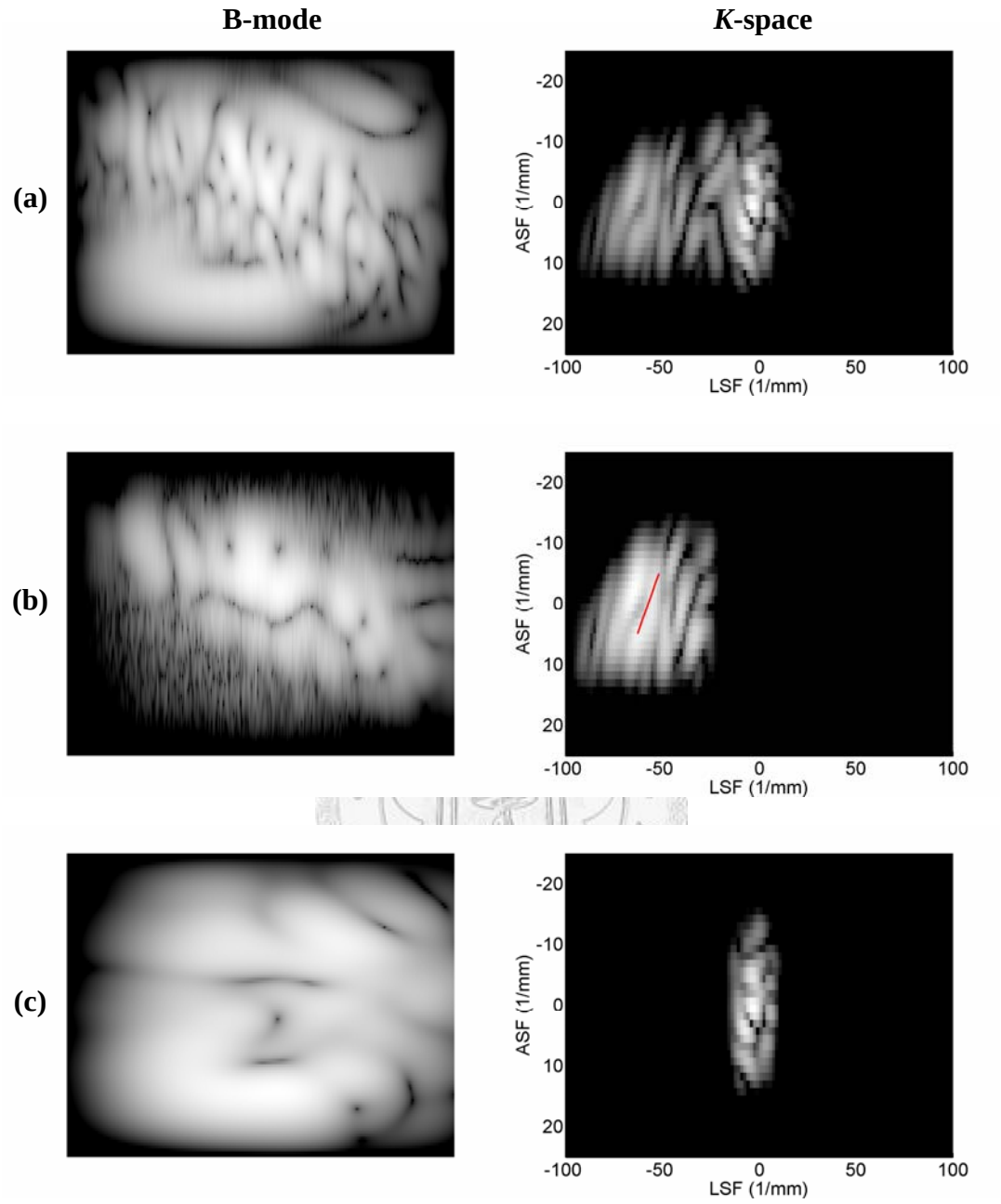

Fig. 4.5. Results of the 2-D wall filter applied to the white box in Fig. 4.4(a). B-mode images (left panels) and the corresponding *k*-space representations (right panels) (a) before and (b) after the wall filtering are shown. The results for the rejected clutter signals are shown in panel (c). All images are displayed over a 30-dB dynamic range. Note that the red line shown in panel (b) represents the estimated mean lateral spatial frequencies corresponding to the axial velocity.

Fig. 4.6 specifically illustrates the lateral spatial spectrum at the center axial spatial frequency before (light solid line) and after the wall filtering (heavy solid line). Note that the horizontal axis represents the equivalent axial velocity. It is observed

that though a slight overlap is present between the flow and clutter signals, the frequencies with larger intensities for the flow signals still can be identified. The estimated axial (dashed line) and lateral (solid line) velocities corresponding to 9 different axial spatial frequencies are shown in Fig. 4.7, where the circles represent the results using the 1-D estimator. By averaging 9 estimates, the estimated axial and lateral velocities for the *k*-space estimator (dotted lines) were −11.1 mm/s and −15.9 mm/s, respectively. This yields a Doppler angle of 55.2°, consistent with the actual Doppler angle.

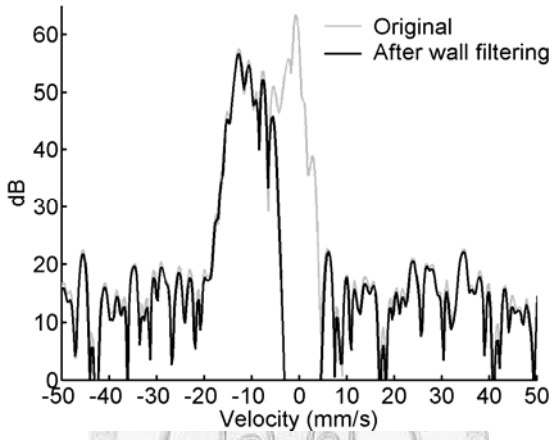

Fig. 4.6. The lateral spatial spectrum at the center axial spatial frequency before (light solid line) and after the wall filtering (heavy solid line) for the white box shown in Fig. 4.4(a). Note that the horizontal axis represents the equivalent axial velocity.

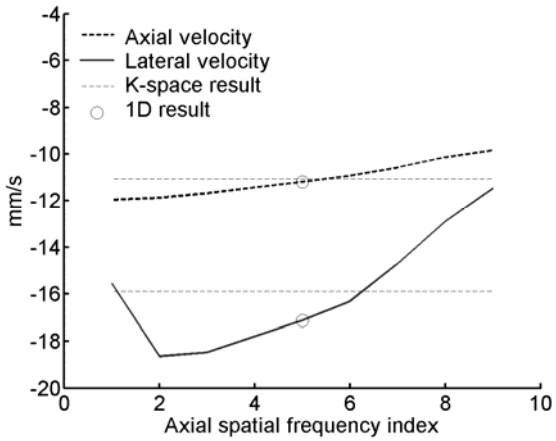

Fig. 4.7. The result of the *k*-space velocity estimator for the white box in Fig. 4.4(a). The estimated axial (dashed line) and lateral velocities (solid line) corresponding to 9 different axial spatial frequencies are shown. The circles represent the results of the 1-D estimator, and the dotted lines are the results of the *k*-space estimator.

For all four color boxes shown in Fig. 4.4(a), the estimation results using the 1-D and *k*-space estimators are compared in Table 4.2. Note that the wall filter was not applied to the black box (i.e., the tissue region). It is shown that the *k*-space estimator can accurately estimate the Doppler angles for the white and blue boxes. For the red box, however, the Doppler angle is overestimated significantly. This is mainly attributed to two facts: (i) the insufficient SNR in this region increases the estimate variance, and (ii) the bandwidth becomes wider at the non-focal range. To demonstrate the robustness of the *k*-space velocity estimator, five successive measurements for the white box were made and the results are listed in Table 4.3. The estimated angle for the *k*-space estimator was 55.4°±8.3° (mean ± standard deviation), better than 48.7°±18.8° for the 1-D estimator.

Table 4.2. Velocity and Doppler angle estimations for the four boxes shown in Fig. 4.4(a) using the 1-D and *k*-space vector velocity estimators

	White box (blood)	**Black box (tissue)**	**Blue box (blood)**	**Red box (blood)**
Axial velocity (mm/s)	−11.1 (−11.2)	0.1 (0.1)	−6.4 (−6.2)	−7 (−7.6)
Lateral velocity (mm/s)	−15.9 (−17.1)	−0.4 (3.6)	−9.1(−2.8)	−34 (−36)
Doppler angle (°)	55.2 (56.8)	N/A	54.6 (23.8)	78.4 (78)

*The actual Doppler angle is around 55°

**The values in the brackets represent the results of the 1-D estimator

Table 4.3. Velocity and Doppler angle estimations for the white box shown in Fig. 4.4(a) with five different realizations using the 1-D and *k*-space vector velocity estimators

	Axial velocity (mm/s)	**Lateral velocity (mm/s)**	**Doppler angle (°)**
	−8.90 (−9.4)	−19.6 (−18.5)	65.5 (63.2)
	−10.2 (−10.3)	−9.4 (−3.1)	42.5 (17.0)
	−11.1 (−11.2)	−15.9 (−17.1)	55.2 (56.8)
	−10.8 (−10.8)	−17.0 (−18.7)	57.9 (60.0)
	−10.5 (−10.1)	−15.5 (−10.6)	55.9 (46.3)
Mean	−10.3 (−10.4)	−15.5 (−13.6)	55.4 (48.7)
Standard deviation	0.9 (0.7)	3.8 (6.7)	8.30 (18.8)

*The actual Doppler angle is around 55°

**The values in the brackets represent the results of the 1-D estimator

The *k*-space estimator was further investigated at a larger Doppler angle where the conventional Doppler-based technique produces a large estimate bias. Fig. 4.8 shows such a case in which the Doppler angle is approximately 75°. Figs. 4.8(a) and (b) show the B-mode and color Doppler images, respectively. It is observed that the estimated velocities in the vessel are generally below 10 mm/s away from the transducer. Using the same display format as in Fig. 4.5, Fig. 4.9 depicts the resulting filtered B-mode images and *k*-space representations for the white box shown in Fig. 4.8(a). The filtered lateral spatial spectrum (heavy solid line) at the center axial spatial frequency is shown in Fig. 4.10, and compared with the one for the stationary tissue (dashed line) indicated as the black box in Fig. 4.8(a). The spectral overlap in this case is much more significant than that in the previous case.

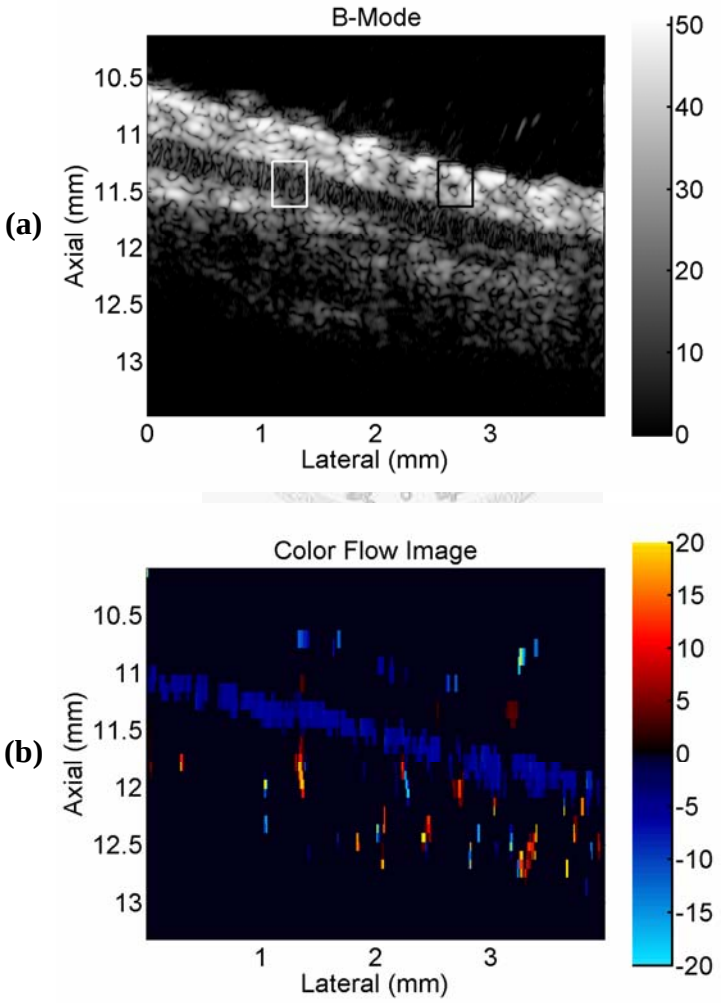

Fig. 4.8. An *in vivo* measurement in a mouse tail (Doppler angle ~ 75°). (a) B-mode image (displayed over 50-dB dynamic range). (b) Color Doppler image (in units of mm/s) using the 1-D autocorrelator. Note that angle correction was not used in panel (b).

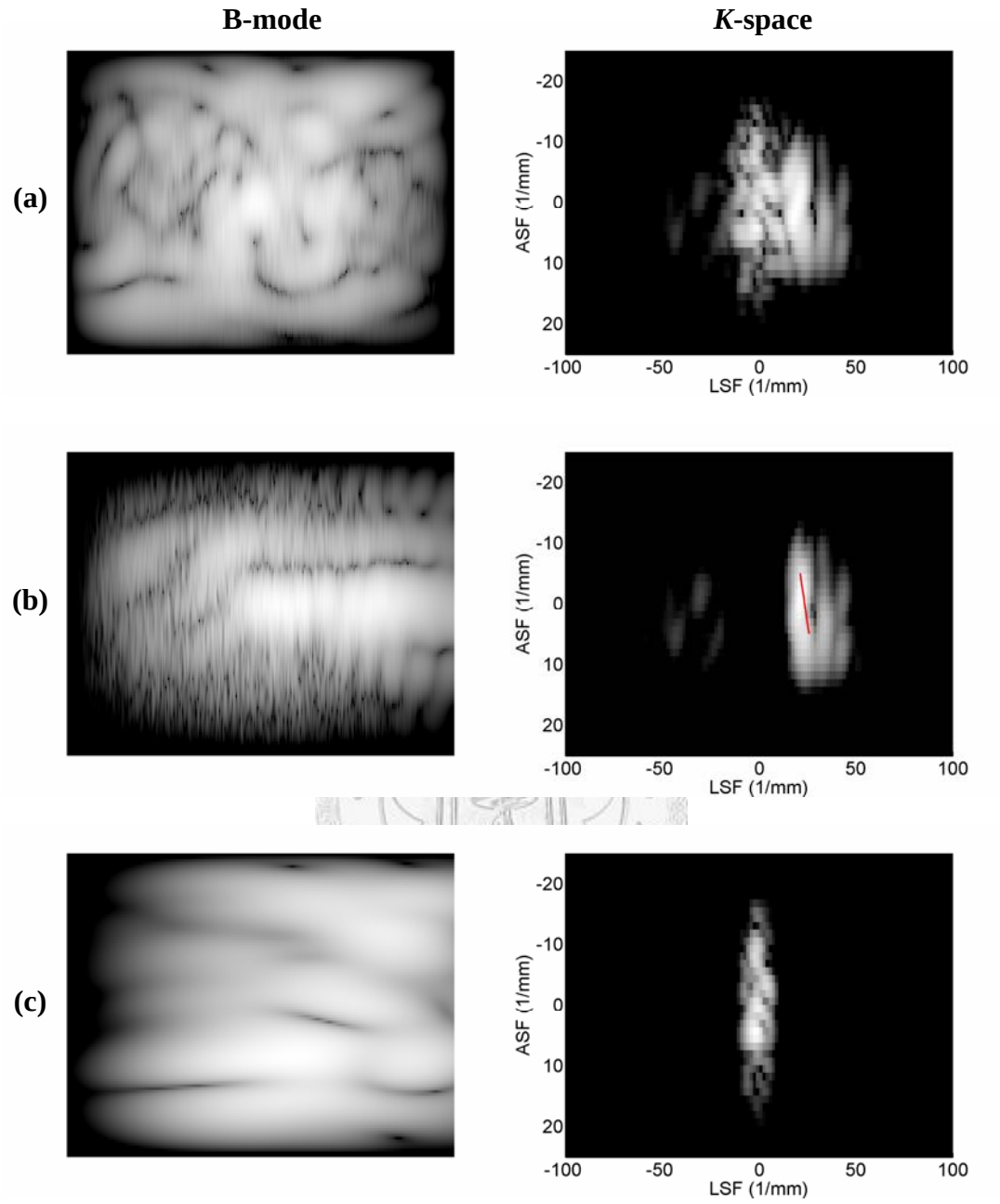

Fig. 4.9. Results of the 2-D wall filter applied to the white box in Fig. 4.8(a). B-mode images (left panels) and the corresponding *k*-space representations (right panels) (a) before and (b) after the wall filtering are shown. The results for the rejected clutter signals are shown in panel (c). All images are displayed over a 30-dB dynamic range. Note that the red line shown in panel (b) represents the estimated mean lateral spatial frequencies corresponding to the axial velocity.

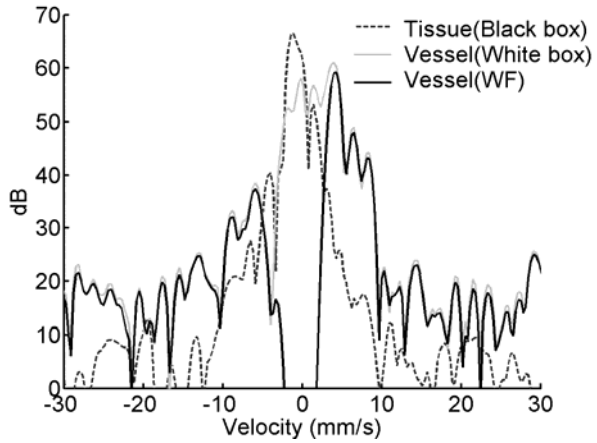

Fig. 4.10. The lateral spatial spectrum at the center axial spatial frequency before (light solid line) and after the wall filtering (heavy solid line) for the white box shown in Fig. 4.8(a). For comparison, the dotted line corresponds to the black box (i.e., the tissue region) shown in Fig. 4.8(a) without wall filtering.

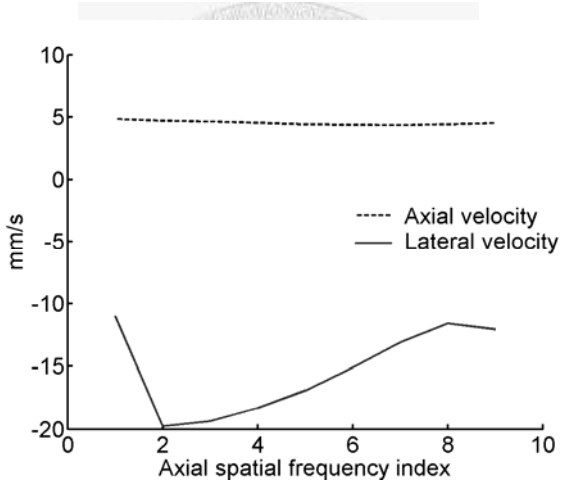

Fig. 4.11. The result of the *k*-space estimator for the white box in Fig. 4.8(a). The estimated axial (dashed line) and lateral velocities (solid line) corresponding to 9 different axial spatial frequencies are shown.

The estimated axial and lateral velocities as a function of the axial spatial frequency for the white box are shown in Fig. 4.11. The estimated axial velocity, lateral velocity, and Doppler angle for the *k*-space estimator were 4.5 mm/s, −15.2 mm/s, and 73.5°, respectively. With five successive measurements at the white box, Table 4.4 summaries the estimation results using the 1-D and *k*-space estimators. The estimated angle for the *k*-space estimator was 69.6°±3.7°, compared to 71.5°±4.7° for the 1-D estimator. Due to presence of the severe spectral overlap, the estimated axial and lateral velocities are over- and under-estimated, respectively, which causes an underestimation in Doppler angle estimation.

Table 4.4. Velocity and Doppler angle estimations for the white box shown in Fig. 4.8(a) with five different realizations using the 1-D and *k*-space vector velocity estimators

	Axial velocity (mm/s)	**Lateral velocity (mm/s)**	**Doppler angle (°)**
	4.5 (4.4)	−15.2 (−16.9)	73.5 (75.4)
	5.4 (5.8)	−12.8 (−13.7)	67.1 (67.3)
	5.4 (5.5)	−11.6 (−12.0)	64.9 (65.5)
	4.9 (5.3)	−16.0 (−19.8)	72.9 (75.0)
	5.6 (5.0)	−14.8 (−17.9)	69.4 (74.4)
Mean	5.2 (5.2)	−14.1 (−16.1)	69.6 (71.5)
Standard deviation	0.5 (0.5)	1.8 (3.2)	3.7 (4.7)

*The actual Doppler angle is around 75°

**The values in the brackets represent the results of the 1-D estimator

4.3 Discussion and Concluding Remarks

In this chapter, both *in vitro* and *in vivo* experiments were conducted to investigate the feasibility of the proposed *k*-space vector velocity estimator. These experimental results demonstrated that the *k*-space velocity estimator can correct for the angle estimation bias caused by the swept scan. Furthermore, compared to the 1-D estimator using only the center axial spatial frequency, the *k*-space estimator can efficiently reduce velocity estimation errors.

In the *in vivo* experiments, the scan speed was set to 10 mm/s according to the analyses in Section 2.2.3. In Fig. 2.8, at the scan speed equal to 10 mm/s, a critical angle of 55° corresponds to a detectable velocity vector of around 8 mm/s, which allows the accurate velocity estimation in the first *in vivo* experiment. However, a critical angle of 75° at this scan speed yields an extremely large minimally detectable velocity and therefore, the spectral overlap is present inevitably and causes an slight angle estimation bias in the second *in vivo* experiment. In this case, decreasing the scan speed can reduce the spectral overlap and improve the angle estimation if the motor control is not a problem. However, our system currently can only provide the stable motor control at the scan speed above 10 mm/s and limits our further investigations below this scan speed.

The *in vivo* results demonstrated the robustness of the *k*-space estimator even in

the presence of the clutter signals. It was shown that employing a 2-D wall filter is capable of removing the clutter signals effectively. The 2-D wall filter applied here had the cut-off lateral spatial frequencies independent of the axial spatial frequency. Nonetheless, if the spectral overlap between the flow and clutter signals becomes non-negligible, a 2-D wall filter with the variable cut-off lateral spatial frequencies increasing with the axial spatial frequency will be desirable. In this case, since the filter is non-separable in rectangular coordinates, the required number of computations is more than that in the case of a filter with a fixed cut-off frequency.

The color Doppler images shown in Figs. 4.4(b) and 4.8(b) were the results with the wall filter being applied to the whole scanned data set. This is different from the conventional step-scan method in which the filter is simply applied to the data obtained with a few number of firings. As mentioned in Section 1.2.2, the transient response of IIR filters affects the first few data and therefore degrades the performance of velocity estimation in a step scan. In contrast, the transient response is absent in a swept scan except at the edges of the scanned image. To investigate the effects of the transient response on velocity estimation in a step scan, the wall filter with zero initialization was individually applied to the data set spanning 16 scan lines. Note that this is not identical to the step scan but helps the understanding of such a transient effect. The results are shown in Fig. 4.12(b) and compared to the case of the swept scan shown in Fig. 4.12(a) (note that Fig. 4.12(a) is identical to Fig. 4.4(b)). It is shown the transient response results in several false flows that are not present in the B-mode image (see Fig. 4.4(a)) and also increases the estimation variance. The results demonstrate the advantage of the wall filter applied in a swept scan.

Finally, the *in vivo* results also indicated that the performance of the *k*-space estimator degrades as the SNR decreases. The main reason is that the maximum frequency determined by the threshold method is susceptible to the noise. A more robust maximum frequency estimation method, such as integrated power spectrum methods, can be used to solve this problem [55]. However, it is not clear whether this method is more affected by the presence of the clutter signals than the threshold method. Another method is to increase the SNR of the system using coded excitation [56]. We will examine the possibility of velocity estimation with this technique in Chapter 5.

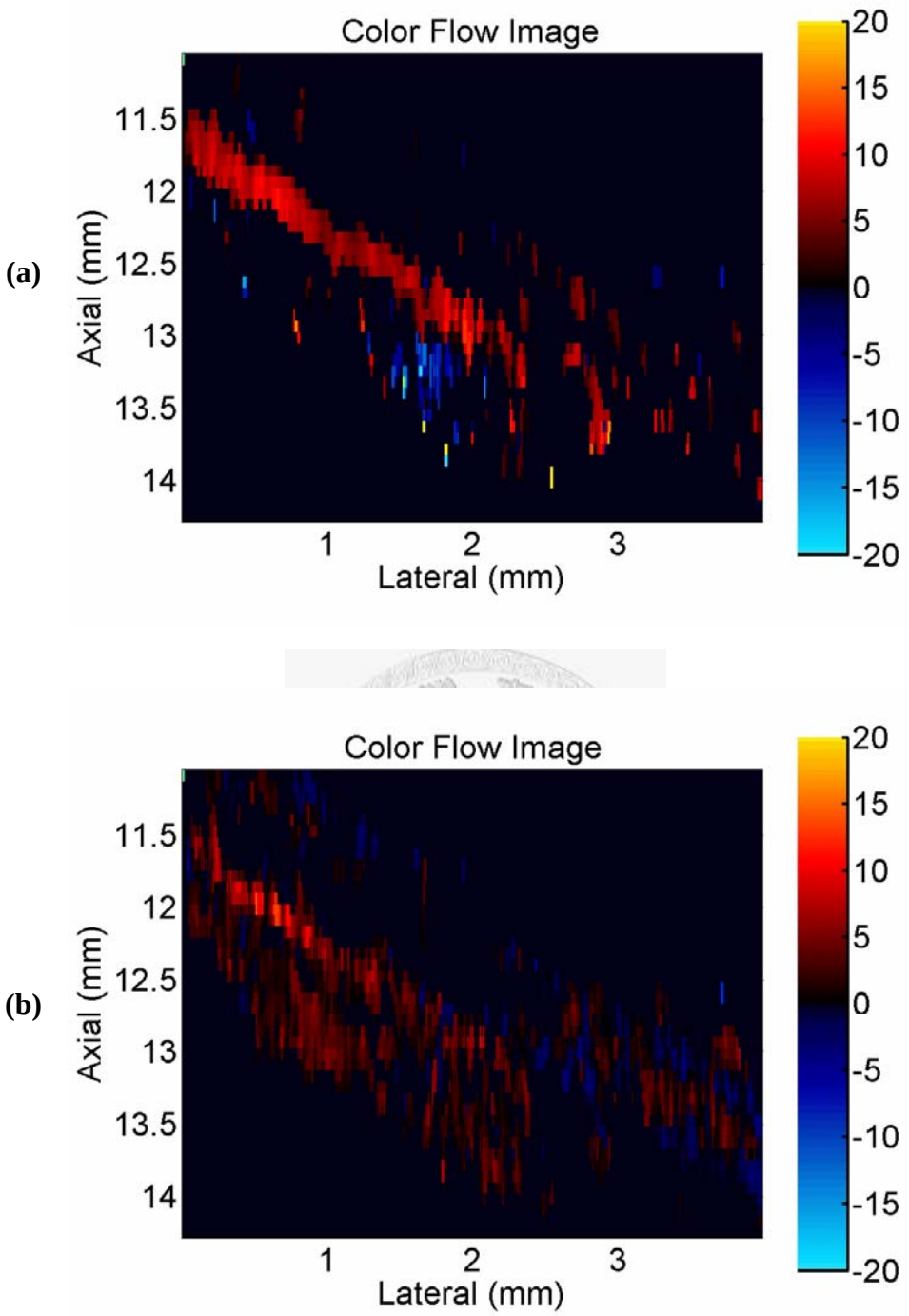

Fig. 4.12. Comparison of the color Doppler images by applying the wall filter to (a) the whole data set (spanning 4000 scan lines) and (b) the partial data set (16 scan lines). Note that panel (a) is identical to Fig. 4.4(b).

Chapter 5 Discussion

5.1 *K*-space Estimation in Swept-scan vs. Spectral-broadening-based Estimation in Step-scan

In this section, the *k*-space vector velocity estimator in a swept scan is compared to the conventional spectral-broadening-based techniques in a step scan. To obtain the accurate lateral velocity estimation, both methods require a sufficiently long observation window. Given the same PRI and axial window length (i.e., the range gate), both methods have the same observation time if the number of repeated firings (in step scanning) is equal to the number of scan lines (in swept scanning). In Chapter 3, it was shown that the required kernel size for the *k*-space estimator is 8λ×10λ. Hence, regardless of its improvement in the frame rate, the spatial resolution for the *k*-space estimator is worse than that for the spectral-broadening-based technique in a step scan (the lateral spatial resolution is 2λ according to Table 2.1). Nonetheless, the *k*-space estimator is capable of detecting the direction of the lateral velocity, which is not possible for the conventional technique in a step scan.

Before further comparing the performances of both techniques, the required number of repeated firings for the conventional spectral-broadening-based technique is evaluated. Instead of using the transit time [40], a spatial-domain method that is similar to the analysis on the kernel size in a swept scan is introduced. This is depicted in Fig. 5.1, where a moving object in a step scan (panel (a)) can be equivalently represented in a swept scan. A 2-D moving object in a step scan can be viewed as an axially moving object in a swept scan with a scan speed equal to the lateral velocity component of the object (panel (b)). This produces a tilted PSF as shown in panel (c). To preserve the −6-dB lateral width of the resulting PSF, the required number of firings N_{R} must satisfy

$$(N_{\mathrm{R}} - 1)\mathrm{PRI}\left|u_{\mathrm{obj}} \sin\theta\right| \geq \lambda f_{\mathrm{num}} . \tag{5.1}$$

Rearrange (5.1) as

$$(N_{\mathrm{R}}-1)\mathrm{PRI} \geq \frac{\lambda f_{\mathrm{num}}}{\left|u_{\mathrm{obj}} \sin\theta\right|}, \tag{5.2}$$

i.e., the observation time has to be longer than the transit time [35]. N_{R} increases as the lateral object velocity decreases. Once N_{R} is determined, the required axial window size is $(N_{\mathrm{R}}-1)\mathrm{PRI}\left|u_{\mathrm{obj}} \cos\theta\right|$. For instance, according to Table 2.1, in order to detect a velocity of 30 mm/s with a Doppler angle larger than 10°, 144 firings with an 11λ range gate are required.

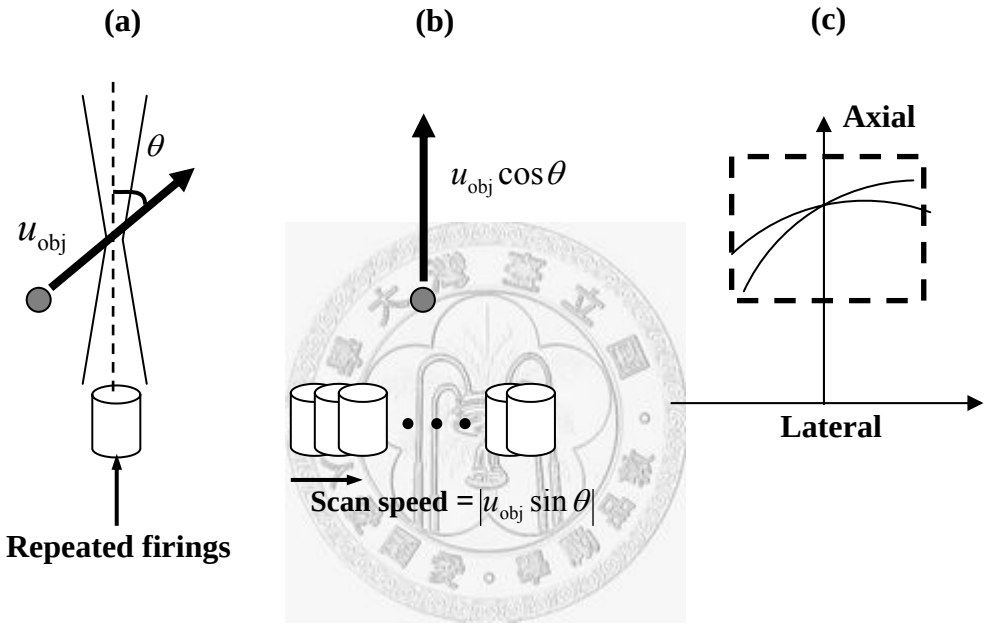

Fig. 5.1. Illustration of a moving object in a step scan (panel (a)) being represented equivalently in a swept scan (panel (b)). The resulting PSF is shown in panel (c). The dashed box indicates the required observation window for vector velocity estimation.

The influence of number of firings on the accuracy of the bandwidth estimation was further investigated by single-object simulations. The simulations are identical to those used in a swept scan (see Section 3.2.1). Figs. 5.2(a) and (b) show the estimated −12-dB Doppler bandwidth as a function of the lateral velocity for different combinations of N_{R} and the range gate length when the velocity vector was fixed at 30 and 50 mm/s, respectively. The proportionality between the bandwidth and the lateral velocity component in a step scan roughly holds for $N_{\mathrm{R}} = 303$ with a 20λ range gate, but such large firings are not feasible for a real-time system. $N_{\mathrm{R}} < 65$ is insufficient to obtain such a proportional relationship. Different from the results obtained using (5.1), $N_{\mathrm{R}} = 151$ is simply adequate to detect lateral velocities higher

than 30 mm/s.

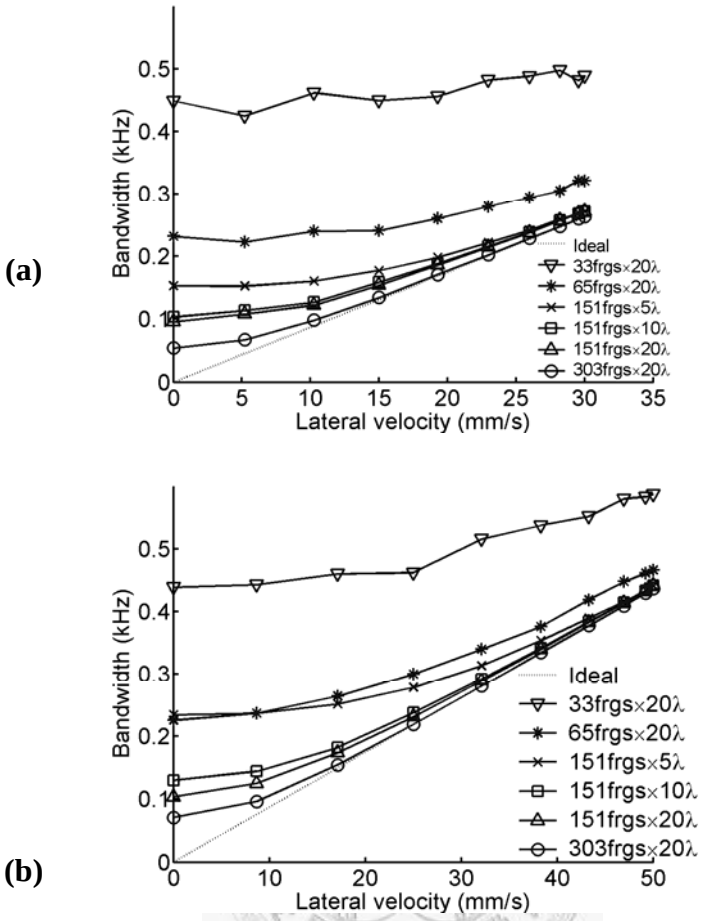

Fig. 5.2. Effects of the number of repeated firings in a step scan on the –12-dB Doppler bandwidth. The velocity vector was fixed at (a) 30 mm/s and (b) 50 mm/s. '33frgs×20λ' represents 33 firings with a 20λ range gate.

Simulation results of the velocity estimation for the *k*-space estimator (right column) and the conventional technique in a step scan (left column) are compared in Fig. 5.3, which is on the basis that both estimators have the same range gate length (10λ) and the observation time (151 firings vs. 8λ lateral kernel spanning 151 scan lines). In these simulations, the flow velocity vector was 30 mm/s with a Doppler angle ranging from –90° to 0°. Other parameters are the same as those in Section 3.2.2. Figs. 5.3(a)–(c) show the estimated lateral velocities, axial velocities, and Doppler angles, respectively. For the conventional technique in a step scan, two different estimation methods using the center frequency (called the narrowband estimator) and 15 RF frequencies (called the wideband estimator) are shown. The *k*-space estimator averaged the estimates from 15 axial spatial frequencies. Overall, due to the insufficient observation window, the lateral velocities in a step scan are overestimated

and angle estimation errors are significant at smaller angles. Fig. 5.3 demonstrates that, under the same observation window with an adequate size, the *k*-space estimator

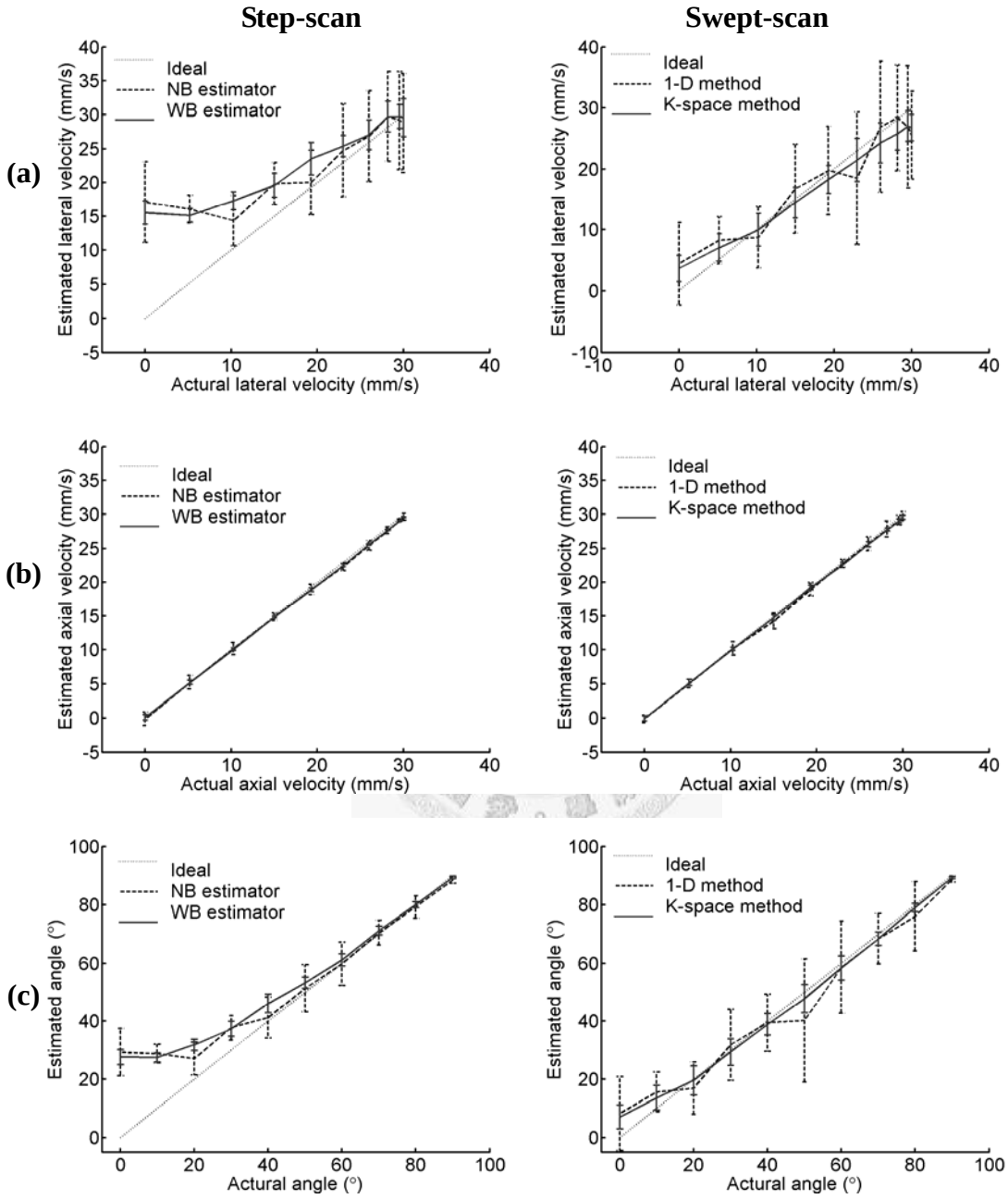

Fig. 5.3. Comparison of constant–flow simulation results between the step- (left panels) and swept-scan (right panels) methods. Panels (a)–(c) correspond to the estimates of lateral velocities, axial velocities, and Doppler angles, respectively. For the step-scan method, 151 firings with a 10λ range gate were used. For the swept-scan method, the kernel size was 8λ×10λ. For both scanning methods, the dashed lines represent the estimates using only the center (axial spatial) frequency, whereas the solid lines are those using 15 RF (axial spatial) frequencies.

provides a wider range of angles than the conventional technique in a step scan. The superiority of the *k*-space estimator is due to the fact that at a given Doppler angle, swept scanning increases the bandwidth and thus decreases the required observation window. Employing spatial averaging can effectively increase the observation time required for the conventional technique in a step scan [40], but the advantage of spatial resolution in a step scan over swept scan is limited.

5.2 *K*-space Vector Velocity Estimator Using Coded Excitation

Transmitting a coded signal and compressing received echoes properly can improve the SNR and the penetration depth [56]. Compared to conventional pulsed excitation with a few cycles, coded signals with large time-bandwidth products have longer durations without sacrificing the bandwidths. Therefore, given the same peak transmission power, the SNR in a coded excitation system is theoretically improved by a factor equal to the time-bandwidth product of the coded signal. The practical SNR improvement depends on both the spectral shapes of the code and the compression filter [56]. Since the attenuation increases with the operating frequency, coded excitation is of particular interest in high-frequency ultrasound. In this section, effects of the coded signal on the *k*-space velocity estimator are examined by simulations.

A linear frequency modulated waveform (also known as a chirp) was used. It has the property that the instantaneous frequency varies linearly with time. The PSFs and the corresponding *k*-space representations in a swept-scanned chirp excitation system are illustrated in Fig. 5.4. In this figure, the chirp had a duration of 2.5μs within which the frequency increased from 20 to 60 MHz. A Chebyshev-shaped matched filter capable of suppressing sidelobes to a –55dB level was used as a compression filter. Other simulation parameters were the same as those listed in Table 2.1. Figs. 5.4(a) and (b) show the results of the stationary object without and with compression, respectively, whereas (c) and (d) show those of the object moving with a velocity of 30 mm/s and a Doppler angle of –30°. It is found that the results with compression are similar to those with pulsed excitation shown in Fig. 2.4. Moreover, the compression filter does not affect the *k*-space representation, except that the axial spatial bandwidth is slightly reduced due to the shaping window applied in the matched filter.

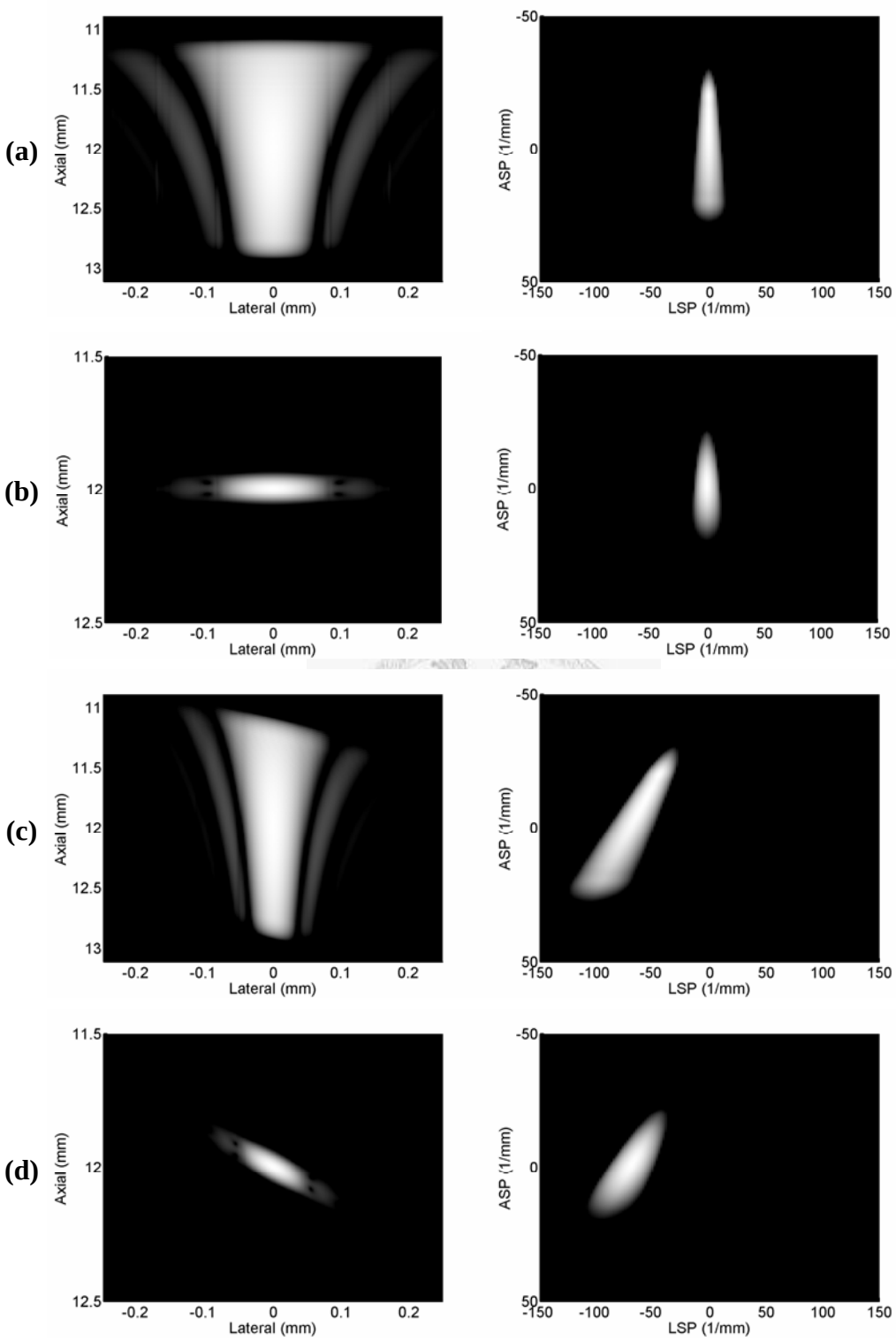

Fig. 5.4. PSFs (left panels) and their *k*-space representations (right panels) using chirped excitation. Panels (a) and (b) correspond to the stationary object without and with compression, respectively. Panels (c) and (d) correspond to the object moving with a velocity of 30 mm/s and a Doppler angle of –30° without and with compression, respectively.

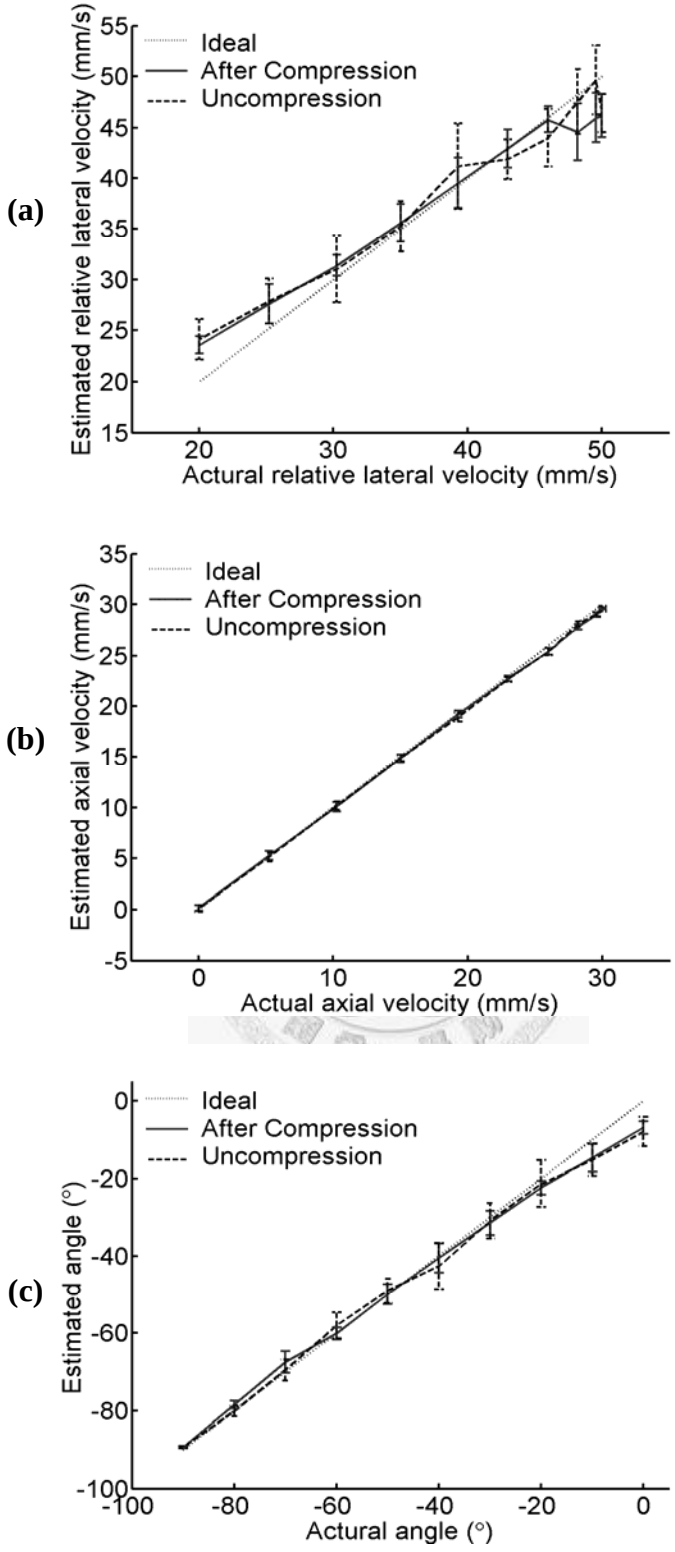

Fig. 5.5. Constant-flow simulation results of the *k*-space velocity estimator using chirp excitation. The velocity estimation with (solid lines) and without (dashed lines) pulse compression are compared. The flow velocity was fixed at 30 mm/s and the Doppler angle varied from –90° to 0°. Panels (a)–(c) correspond to the estimates of u_{rel}, axial velocities, and Doppler angles, respectively.

To further investigate the feasibility of the *k*-space vector velocity estimator using coded excitation, constant flows with a velocity of 30 mm/s and Doppler angles ranging from –90° to 0° were simulated. Except for the transmitted signal, the simulation conditions were identical to those in Section 3.2.2. The parameters for the *k*-space estimator used here (including the kernel size, the bandwidth threshold, the scaling factor, and the number of axial spatial frequencies) were also identical to those in Section 3.2.2. The velocity estimation results using the *k*-space estimator are shown in Fig. 5.5. Figs. 5.5(a)–(c) show the estimated lateral velocities, axial velocities, and Doppler angles, respectively. The estimation results before (dashed lines) and after (solid lines) compression are compared to each other. The dotted lines represent the actual values. Ten realizations were generated to produce the mean and standard deviation values. Compared to the case with pulsed excitation (see Fig. 3.2), it is shown that the *k*-space velocity estimator also performs well using coded excitation with compression. Furthermore, although the axial kernel size (10λ) is less than the chirp length (50λ), the performance of velocity estimation without compression does not degrade significantly. This is because the kernel mainly truncates the upper and lower axial spatial frequencies, and has less effects around the center axial spatial frequencies used for averaging. Therefore, if the kernel is large enough to maintain the center axial spatial frequency, the *k*-space velocity estimator can also be performed on the uncompressed flow data.

5.3 Applying *K*-space Estimator to Electronic-scanning Array Systems

Although the proposed *k*-space velocity estimator is mainly developed in a mechanical swept-scan system, applying it to a transducer array with electronic scanning is straightforward. In this case, since the elements accounting for transmission and reception have no relative displacement during the pulse-echo round trip time (i.e., $d = 0$), the term $e^{j\pi f_x d} = 1$ in (2.6) and the *k*-space representations described in Section 2.1 are unchanged, except that the scan speed u_{scan} is replaced by $\Delta x / \text{PRI}$. A potential advantage of electronic scanning over mechanical scanning is that the velocity estimation is free from the errors caused by the variations in the motor speed.

The type of the array has a great impact on the performance of the *k*-space

estimator. In a phased-array system, the beam steering capability allows the scan line increment (i.e., Δx) to be much less than a wavelength. In a linear-array system, on the other hand, Δx is typically on the order of the wavelength. Hence, for a given PRI, flow signals in a linear-array system are more decorrelated. Moreover, the number of scan lines within the kernel is much less than that in a phased-array system. Large Δx may also cause the spectral aliasing and limit the maximum detectable velocity (see Section 2.2.2). These factors lead to the conclusion that the *k*-space estimator should perform better in a phased-array system than in a linear-array system.

5.4 Power Doppler in Swept-scan

To provide accurate velocity vector estimation in a swept scan, the kernel size required for the *k*-space estimator is shown to be as large as 8λ×10λ (~ 0.3 mm×0.4 mm). For measuring microvascular structures (e.g., tumor angiogenesis), however, such a kernel may include a variety of velocity vectors, which makes the *k*-space estimator inadequate for this application. In this case, since the vessels are distributed closely and non-uniformly, techniques capable of providing the high sensitivity rather than flow direction information are demanded. In other words, echoes from flows are usually weak enough so that quantitative velocity estimation is relatively difficult. To increase the sensitivity of flow detection, Power Doppler in which spectral energy of flow signals is displayed is often used to provide qualitative visualization of flow patterns in conventional color Doppler imaging.

Because the lateral spatial spectrum of flow signals in a swept scan broadens linearly with the relative lateral velocity over the scan speed (see (2.9)), the resulting spectral energy increases at the same rate when the spectrum is normalized to its maximum. Therefore, employing Power Doppler in a swept-scan system has to remove the effect of the scanning speed on spectral energy. Note that the 2-D spectrum can be utilized in the calculation of spectral energy. In this case, before combining the spectral energy of the lateral spatial spectra at different axial spatial frequencies, the individual lateral spectral spectra have to be normalized to their individual maxima, and the resulting spectral energy has to remove the dependence on the axial spatial frequency.

In order to provide the sufficient spatial resolution, the kernel used for Power Doppler must be small enough. As a result, spectral energy may be not strictly

proportional to the relative lateral velocity (see Fig. 3.1) and its dependence on the scan speed may be overcompensated. Proper correction of the relationship between spectral energy and the scan speed according to the kernel size is therefore required to provide an appropriate spectral energy map.

Chapter 6 Conclusions and Future Works

In this thesis, effects of the swept-scan technique on vector velocity estimation were investigated using a *k*-space approach. This *k*-space modeling provided an accurate description of 2-D motion in a swept scan. With this technique, it was demonstrated that the swept-scan technique introduced an additional spectral broadening proportional to the scan speed. Experimental results showed that applying the conventional spectral-broadening-based technique to a swept-scan system resulted in an estimation bias as well as an increase in estimation variance.

Based on the *k*-space modeling, a wideband vector velocity estimation technique in a swept scan was proposed. Both simulation and experimental results demonstrated that the proposed velocity estimator can not only correct an estimation bias due to the swept scan, but also outperform conventional narrowband estimation techniques utilizing only the center frequency of the excitation. Furthermore, the proposed velocity estimator also performed better than conventional spectral-broadening-based techniques applied in a step scan in terms of the frame rate and estimation accuracy.

Future works will continue *in vivo* investigations of the performance of the proposed vector velocity estimator to the vessels with more clinical values using mouse animal models, such as carotid, ascending, renal, abdominal, and major arteries. Characteristics of flow pulsation and turbulence within these vessels may have a significant impact on the accuracy of bandwidth estimation. In addition, to assess these flow velocities with a sufficient SNR, the penetration and system sensitivity need to be improved. Therefore, we will also experimentally evaluate the use of coded excitation and/or contrast agents in high-frequency flow velocity vector estimation. It should be noted that combining coded excitation with contrast agents is advantageous for clutter suppression [57]. Another potential technique for clutter reduction with contrast agents is pulse inversion Doppler [58]. Both techniques are particularly applicable to the detection of slow flow velocities in a swept scan and will be investigated.

Appendix A Approximation of (2.2)

The *k*-space representation in a swept scan described in (2.2) can be rewritten as

$$P_{\mathrm{SW}}(f_x, f_z) = G''(f_z) e^{-j2\pi f_z (z_\mathrm{f} - \frac{d^2}{4z_\mathrm{f}})} A_\mathrm{T}(-2z_\mathrm{f} f_x / f_z) * A_\mathrm{T}(-2z_\mathrm{f} f_x / f_z - d) e^{j2\pi f_x d}$$
$$= G''(f_z) e^{-j2\pi f_z (z_\mathrm{f} - \frac{d^2}{4z_\mathrm{f}})} \int A_\mathrm{T}(-2z_\mathrm{f}(f_x - f_x')/f_z)\, A_\mathrm{T}(-2z_\mathrm{f} f_x'/f_z - d) e^{j2\pi f_x' d} \mathrm{d}f_x'$$

$$G''(f_z) = \frac{G}{f_z^{\,2}} B_\mathrm{PE}(\frac{-cf_z}{2}).$$

(A.1)

Let $f'_x = f''_x - f_z d/4z_\mathrm{f}$; (A.1) then becomes

$$P_{\mathrm{SW}}(f_x, f_z) = G''(f_z) e^{-j2\pi f_z (z_\mathrm{f} - \frac{d^2}{4z_\mathrm{f}})} \int A_\mathrm{T}(-2z_\mathrm{f}(f_x - f_x'')/f_z - d/2)$$
$$A_\mathrm{T}(-2z_\mathrm{f} f_x''/f_z - d/2)\, e^{j2\pi(f_x'' - \frac{f_z d}{4z_\mathrm{f}})d} \mathrm{d}f_x''$$
$$= G''(f_z) e^{-j2\pi f_z z_\mathrm{f}} e^{j\pi f_x d} \int A_\mathrm{T}(-2z_\mathrm{f}(f_x - f_x'')/f_z - d/2) e^{-j\pi(f_x - f_x'')d}$$
$$A_\mathrm{T}(-2z_\mathrm{f} f_x''/f_z - d/2) e^{j\pi f_x'' d} \mathrm{d}f_x''$$
$$= G''(f_z) e^{-j2\pi f_z z_\mathrm{f}} e^{j\pi f_x d} \left[A_\mathrm{T}(-2z_\mathrm{f} f_x/f_z - d/2)\, e^{-j\pi f_x d} * A_\mathrm{T}(-2z_\mathrm{f} f_x/f_z - d/2)\, e^{j\pi f_x d} \right]$$

(A.2)

If $f_x d <\!\!\sim \pi$ for f_x corresponding to the nonzero spectrum values, the phase terms in the bracket can be approximated as $1 \pm j\pi f_x d$. (A.2) can therefore be approximated as

$$P_{\mathrm{SW}}(f_x, f_z) \cong G''(f_z) e^{-j2\pi f_z z_\mathrm{f}} e^{j\pi f_x d} \left[A_\mathrm{T}(-2z_\mathrm{f} f_x/f_z - d/2)(1 - j\pi f_x d) \right.$$
$$\left. * A_\mathrm{T}(-2z_\mathrm{f} f_x/f_z - d/2)(1 + j\pi f_x d) \right]$$
$$= G''(f_z) e^{-j2\pi f_z z_\mathrm{f}} e^{j\pi f_x d} \left[A_\mathrm{T}(-2z_\mathrm{f} f_x/f_z - d/2) * A_\mathrm{T}(-2z_\mathrm{f} f_x/f_z - d/2) \right.$$
$$\left. + \pi^2 d^2 (f_x A_\mathrm{T}(-2z_\mathrm{f} f_x/f_z - d/2)) * (f_x A_\mathrm{T}(-2z_\mathrm{f} f_x/f_z - d/2)) \right]$$

(A.3)

Neglecting the term containing d^2 in the bracket, (A.3) can be approximated as

$$P_{\mathrm{SW}}(f_x, f_z) \cong G''(f_z) e^{-j2\pi f_z z_{\mathrm{f}}} e^{j\pi f_x d} \left[A_{\mathrm{T}}(-2z_{\mathrm{f}} f_x / f_z - d/2) * A_{\mathrm{T}}(-2z_{\mathrm{f}} f_x / f_z - d/2) \right]$$

(A.4)

References

[1] J. A. Jensen, *Estimation of blood velocities using ultrasound: a signal processing approach*. New York: Cambridge Univ. Press, 1996.

[2] K. W. Ferrara and G. DeAngelis, "Color flow mapping," *Ultrasound Med. Biol.*, vol. 23, pp. 321–345, 1997.

[3] C. Kasai, K. Namekawa, A. Koyano, and R. Omoto, "Real-time two-dimensional blood flow imaging using an autocorrelation technique," *IEEE Trans. Son. Ultrason.*, vol. SU–32, pp. 458–464, 1985.

[4] T. Loupas, J. T. Powers, and R. W. Gill, "An axial velocity estimator for ultrasound blood flow imaging, based on a full evaluation of the Doppler equation by means of a two-dimensional autocorrelation approach," *IEEE Trans. Ultrason., Ferroelect., Freq. Contr.*, vol. 42, no. 4, pp. 672–688, 1995.

[5] K. W. Ferrara and V. R. Algazi, "A new wideband spread target maximum likelihood estimator for blood velocity estimation – Part I: Theory," *IEEE Trans. Ultrason., Ferroelect., Freq. Contr.*, vol. 38, no. 1, pp. 1–16, 1991.

[6] S. K. Alam and K. J. Parker, "The butterfly search technique for estimation of blood velocity," *Ultrasound Med. Biol.*, vol. 21, no. 5, pp. 657–670, 1995.

[7] F. S. Foster, C. J. Pavlin, K. A. Harasiewicz, D. A. Christopher, and D. H. Turnbull, "Advances in ultrasound biomicroscopy," *Ultrasound Med. Biol.*, vol. 26, no. 1, pp. 1–27, 2000.

[8] G. R. Lockwood, D. H. Turnbull, D. A. Christopher, and F. S. Foster, "Beyond 30 MHz – applications of high frequency ultrasound imaging," *IEEE Eng. Med. Biol. Mag.* vol. 15, pp. 60–71, 1996.

[9] D. A. Knapik, B. Starkoski, C. J. Pavlin, and F. S. Foster, "A 100–200 MHz ultrasound biomicroscope," *IEEE Trans. Ultrason., Ferroelect., Freq. Contr.*, vol. 47, no. 6, pp. 1540–1549, 2000.

[10] K. W. Ferrara, B. G. Zagar, J. B. Sokil-Melgar, R. H. Silverman, and I. M. Aslanidis, "Estimation of blood velocity with high frequency ultrasound," *IEEE Trans. Ultrason., Ferroelect., Freq. Contr.*, vol. 43, no. 1, pp. 149–157, 1996.

[11] C. J. Pavlin, D. A. Christopher, P. N. Burns, and F. S. Foster, “High frequency Doppler ultrasound examination of blood flow in the anterior segment of the eye,” *Am. J. Ophthalmol.*, vol. 126, no. 4, pp. 597–600, 1998.

[12] D. A. Christopher, P. N. Burns, and F. S. Foster, “High frequency continuous wave Doppler ultrasound system for the detection of blood flow in the microcirculation,” *Ultrasound Med. Biol.*, vol. 22, no. 3, pp. 1196–1203, 1996.

[13] D. A. Christopher, P. N. Burns, B. G. Starkoski, and F. S. Foster, “A high-frequency pulsed wave Doppler ultrasound system for the detection and imaging of blood flow in the microcirculation,” *Ultrasound Med. Biol.*, vol. 23, no. 7, pp. 997–1015, 1997.

[14] D. E. Kruse, R. H. Silverman, R. J. Fornaris, D. J. Coleman, and K. W. Ferrara, “A swept-scanning mode for estimation of blood velocity in the microvasculature,” *IEEE Trans. Ultrason., Ferroelect., Freq. Contr.*, vol. 45, no. 6, pp. 1437–1440, 1998.

[15] D. E. Goertz, D. A. Christopher, J. L. Yu, R. S. Kerbel, P. N. Burns, and F. S. Foster, “High-frequency color flow imaging of the microcirculation,” *Ultrasound Med. Biol.*, vol. 26, no. 1, pp. 63–71, 2000.

[16] D. E. Goertz, J. L. Yu, R. S. Kerbel, P. N. Burns, and F. S. Foster, “High-frequency 3-D color-flow imaging of the microcirculation,” *Ultrasound Med. Biol.*, vol. 29, no. 1, pp. 39–51, 2003.

[17] F. S. Foster, P. N. Burns, D. H. Simpson, S. R. Wilson, D. A. Christopher, and D. E. Goertz, “Ultrasound for the visualization and quantification of tumor microcirculation,” *Cancer Metastasis Rev.*, vol. 19, pp. 131–138, 2000.

[18] C. Kargel, G. Plevnik, B. Trummer, and M. F. Insana, “Doppler ultrasound systems designed for tumor blood flow imaging,” *IEEE Trans. Ins. and Meas.,* vol. 53, no. 2, pp. 524–536, 2004.

[19] M.-L. Li, Y.-F Chen, W.-J. Guan, and P.-C. Li, “A Digital Ultrasonic System for Small Animal Imaging,” *Ultrason. Imag.*, vol. 26, pp. 85–99, 2004.

[20] P.-C. Li, Y.-F Chen, W.-J. Guan, “Ultrasonic high frequency blood flow imaging of small animal tumor models,” in *Proc. IEEE Ultrason. Symp.,* 2003, pp. 1598–1601.

[21] C. K. Phoon, O. Aristizábal, and D. H. Turnbull, “40 MHz Doppler characterization of umbilical and dorsal aortic blood flow in the early mouse embryo,” *Ultrasound Med. Biol.*, vol. 26, no. 8, pp. 1275–1283, 2000.

[22] F. S. Foster *et al.*, “A new ultrasound instrument for *in vivo* microimaging of mice,” *Ultrasound Med. Biol.*, vol. 28, no. 9, pp. 1165–1172, 2002.

[23] S. M. Day, J. L. Reeve, D. D. Myers, and W. P. Fay, “Murine Thrombosis Models,” *Thromb Haemost*, vol. 92, pp. 486–494, 2004.

[24] A. Liu, A.L. Joyner and D.H. Turnbull, “Alteration of limb and brain patterning in early mouse embryos by ultrasound-guided injection of Shh-expressing cells,” *Mech Dev*, vol. 75, pp. 107–115, 1998.

[25] C.-K. Yeh, K. W. Ferrara, and D. E. Kruse, “High-resolution functional vascular assessment with ultrasound,” *IEEE Trans. Med. Imag*., vol. 23, no. 10, pp. 1263–1274, 2004.

[26] R. V. Shohet *et al.*, “Echocardiographic destruction of albumin microbubbles directs gene delivery to the myocardium,” *Circulation*, vol. 101, pp. 2554–2556, 2000.

[27] D. E. Kruse and K. W. Ferrara, “A new high resolution color flow system using an eigendecomposition-based adaptive filter for clutter rejection,” *IEEE Trans. Ultrason., Ferroelect., Freq. Contr.*, vol. 49, no. 12, pp. 1739–1754, 2002.

[28] H. Torp, “Clutter rejection filters in color flow imaging: a theoretical approach,” *IEEE Trans. Ultrason., Ferroelect., Freq. Contr.*, vol. 44, no. 2, pp. 417–424, 1997.

[29] A. Bjaerum, H. Torp, and K. Kristofferson, “Clutter filters design for ultrasound color flow imaging,” *IEEE Trans. Ultrason., Ferroelect., Freq. Contr.*, vol. 49, no. 2, pp. 204–216, 2002.

[30] P.-C. Li, C.-J. Cheng, and C.-K. Yeh, “On velocity estimation using speckle decorrelation,” *IEEE Trans. Ultrason., Ferroelect., Freq. Contr.*, vol. 48, no. 4, pp. 1084–1091, 2001.

[31] J. R. Overbeck, K. W. Beach, and D. E. Strandness, Jr., “Vector Doppler: Accurate measurement of blood velocity in two dimensions,” *Ultrasound Med. Biol.*, vol. 18, pp. 19–31, 1992.

[32] M. D. Fox and W. D. Gardiner, “Three-dimensional Doppler velocimetry of flow jets,” *IEEE Trans. Biomed. Eng.,* vol. 35, no. 10, pp. 834–841, 1988.

[33] M. E. Anderson, “Multi-dimensional velocity estimation with ultrasound using spatial quadrature,” *IEEE Trans. Ultrason., Ferroelect., Freq. Contr.*, vol. 45, no. 3, pp. 852–861, 1998.

[34] J. A. Jensen and P. Munk, “A new method for estimation of velocity vectors,” *IEEE Trans. Ultrason., Ferroelect., Freq. Contr.*, vol. 45, no. 3, pp. 837–851, 1998.

[35] G. E. Trahey, J. W. Allison, and O. T. von Ramm, “Angle independent ultrasonic detection of blood flow, “ *IEEE Trans. Biomed. Eng.,* vol. 34, no. 12, pp. 965–967, 1987.

[36] L. N. Bohs, B. H. Friemel, and G. E. Trahey, “Experimental velocity profiles and volumetric flow via two-dimensional speckle tracking,” *Ultrasound Med. Biol.*, vol. 21, pp. 885–898, 1995.

[37] L. N. Bohs, B. J. Geiman, M. E. Anderson, S. M. Breit,and G. E. Trahey, “Ensemble tracking for 2D vector velocity measurement: experimental and initial clinical results,” *IEEE Trans. Ultrason., Ferroelect., Freq. Contr.*, vol. 45, no. 4, pp. 912–923, 1998.

[38] V. L. Newhouse, E. S. Furgason, G. F. Johnson, and D. A. Wolf, “The dependence of ultrasound bandwidth on beam geometry,” *IEEE Trans. Sonics Ultrason.*, vol.27, no. 2, pp. 50–59, 1980.

[39] V. L. Newhouse, D. Censor, T. Vontz, J. A. Cisneros, and B. B. Goldberg, “Ultrasound Doppler probing of flows transverse with respect to beam axis,” *IEEE Trans. Biomed. Eng.*, vol. 34, no. 10, pp. 779–789, 1987.

[40] P.-C. Li, C.-J. Cheng, and C.-C. Shen, “Doppler angle estimation using correlation,” *IEEE Trans. Ultrason., Ferroelect., Freq. Contr.*, vol. 47, no. 1, pp. 188–196, 2000.

[41] C.-K. Yeh and P.-C. Li, “Doppler angle estimation using AR modeling,” *IEEE Trans. Ultrason., Ferroelect., Freq. Contr.*, vol. 49, no. 6, pp. 683–692, 2002.

[42] B.-R Lee, H. K. Chiang, C.-D. Kuo, W.-L. Lin, and S.-K. Lee, “Doppler angle and flow velocity estimations using the classic and transverse Doppler effects,”

IEEE Trans. Ultrason., Ferroelect., Freq. Contr., vol. 46, no. 1, pp. 252–256, 1999.

[43] M. O'Donnell, A. R. Skovoroda, B. M. Shapo, and S. Y. Elemlianov, "Internal displacement and strain imaging using ultrasonic speckle tracking," *IEEE Trans. Ultrason., Ferroelect., Freq. Contr.*, vol. 41, no. 3, pp. 314–325, 1994.

[44] P.-C. Li, C.-Y. Li, and W.-C. Yeh, "Tissue motion and elevational speckle decorrelation in freehand 3D ultrasound," *Ultrason. Imag.*, vol. 24, pp. 1–12, 2002.

[45] W. F. Walker and G. E. Trahey, "The application of *k*-space in pulse echo ultrasound," *IEEE Trans. Ultrason., Ferroelect., Freq. Contr.*, vol. 45, no. 3, pp. 541–558, 1998.

[46] B. H. Friemel, L. N. Bohs, K. R. Nightingale, and G. E. Trahey, "Speckle decorrelation due to two-dimensional flow gradients," *IEEE Trans. Ultrason., Ferroelect., Freq. Contr.*, vol. 45, no. 2, pp. 317–327, 1998.

[47] M.-L. Li, Wei-Jung Guan, and P.-C. Li, "Improved synthetic aperture focusing with applications in high-frequency ultrasound imaging," *IEEE Trans. Ultrason., Ferroelect., Freq. Contr.*, vol. 51, no. 1, pp. 63–70, 2004.

[48] C. Passmann and H. Ermert, "A 100-MHz ultrasound imaging system for dermatologic and ophthalmologic diagnostics," *IEEE Trans. Ultrason., Ferroelect., Freq. Contr.*, vol. 43, no. 4, pp. 545–552, 1996.

[49] P.-C. Li and M.-L. Li, "Adaptive imaging using the generalized coherence factor," *IEEE Trans. Ultrason., Ferroelect., Freq. Contr.*, vol. 50, no. 2, pp. 128–141, 2003.

[50] J. A. Jensen, " Field: A program for simulating ultrasound systems," *Med. Biol. Eng. Comp.*, 10th Nordic-Baltic Conference on Biomedical Imaging, vol. SU–4, Part 1, pp. 351–353, 1996b.

[51] W. T. Mayo and P. M. Embree, "Two-dimensional processing of pulsed Doppler signals," U.S. Patent 4930513, Jun 5, 1990.

[52] L. S. Wilson, "Description of broad-band pulsed Doppler ultrasound processing using the two-dimensional Fourier transform." *Ultrason. Imag.*, vol. 13, pp. 301–315, 1991.

[53] P. J. Vaitkus and R. S. C. Cobbold, “A new time-domain narrowband velocity estimation technique for Doppler ultrasound flow imaging. I. Theory,” *IEEE Trans. Ultrason., Ferroelect., Freq. Contr.*, vol. 45, no. 3, pp. 939–954, 1998.

[54] P. Tortoli, G. Guidi, and V. L. Newhouse, “Improved blood velocity estimation using the maximum Doppler frequency,” *Ultrasound Med. Biol.*, vol. 21, pp. 527–532, 1995.

[55] A. H. Steinman, J. Tavakkoli, J. G. Myers, R. S. C. Cobbold, and K.W. Johnston, “Sources of error in maximum velocity estimation using linear phased-array Doppler systems with steady flow,” *Ultrasound Med. Biol.*, vol. 27, pp. 655–664, 2001.

[56] M. O’Donnell, “Coded excitation system for improving the penetration of real-time phased-array imaging systems,” *IEEE Trans. Ultrason., Ferroelect., Freq. Contr.*, vol. 39, no. 3, pp. 341–351, 1992.

[57] J. M. Borsboom, C. T. Chin, A. Bouakaz, M. Versluis, and N. de Jong, “Harmonic chirp imaging method for ultrasound contrast agent,” *IEEE Trans. Ultrason., Ferroelect., Freq. Contr.*, vol. 52, no. 2, pp. 241–249, 2005.

[58] D. H. Simpson, T. C. Chien, and P. N. Burn, “Pulse inversion Doppler: a new method for detecting nonlinear echoes from microbubble contrast agents,” *IEEE Trans. Ultrason., Ferroelect., Freq. Contr.*, vol. 46, no. 2, pp. 372–382, 1999.